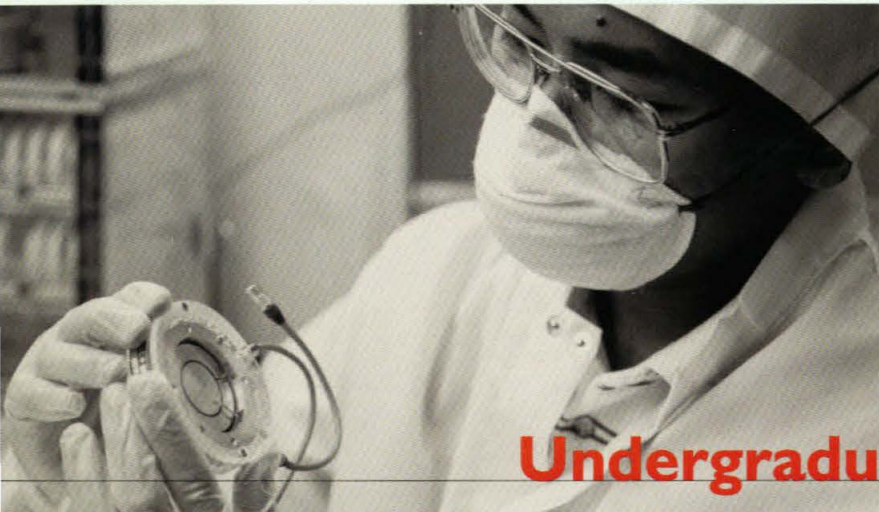


CALTECH



Undergraduate Research Journal

1997

© 1997

Caltech Undergraduate Research Journal

A collection of technical papers by SURF students who completed research in the summers of 1996 and 1997.

Caltech's Summer Undergraduate Research Fellowships (SURF) program gives participants an opportunity to conduct research under the guidance of leading scientists and technical researchers. The SURF program introduces students to the process of scientific investigation as a creative intellectual activity and provides them with a realistic view of the demands and rewards of a professional research career.

SURF's mission supports Caltech's educational purpose: to train the creative type of scientist or engineer urgently needed in our educational, governmental, and industrial development. SURF provides a new dimension to the process of undergraduate education; program participants apply knowledge gained in the laboratories and classrooms toward finding solutions to problems at the frontiers of science and technology. SURF graduates, with their sophisticated and practical knowledge of how to conduct research, have a marked advantage as they begin their careers, apply to graduate schools, or look for jobs in industry.

SURF draws upon the world-renowned research resources and expertise available at Caltech. Indeed, it is the seasoned faculty and technical advisors working with outstanding students who have helped to make SURF the excellent program that it has become since its beginnings in 1979.

Caltech students have rich opportunities to delve into the research environment, to explore the secrets of nature, and to develop new devices or new processes. They bring their skills and talents, background course work, and drive and enthusiasm to the process of science. The stimulating environment at Caltech encourages inquiry and leads students to deepen their scientific and engineering roots.

An important component of undergraduate research is the chance for students to communicate their work. In 1995 the SURF Student Advisory Council (SURFSAC) initiated the first *Caltech Undergraduate Research Journal (CURJ)* to publish the best papers submitted that summer. We applaud the enthusiasm and determination of SURFSAC of students to continue this venture as we present the 1996 and 1997 *CURJ*.

Each paper initially was reviewed by the SURFSAC editorial board and finally reviewed by a faculty editorial board. Student editors had the experience of going through the editorial and publication process, interacting with authors and their mentors. Student authors derived the benefit of the review process to produce excellent papers. We thank the authors and editors whose efforts are reflected in the second *Caltech Undergraduate Research Journal*.

Carolyn Merkel
Director
Student-Faculty Programs

1996 *CURJ*

Student Reviewers:

Sudipta Bardhan, Editor
Priya Rai, SURFSAC Chair
Nasim Afsarmanesh
Jonathan Burrows
Lin Jia
Carlos Maldonado
Jeffrey Miller
James Quallen
Kanna Shimizu
Elwyn Uy
Amy Zheng

Faculty Editors:

John Allman
Charles J. Brokaw
Paolo Ghiradato
Jerrold E. Marsden
Ray D. Owen
John H. Richards
John D. Roberts
Paul W. Sternberg
Harold Zirin
Zhen-Gang Wang

1997 *CURJ*

Student Reviewers:

Minoree Kohwi, Editor
Sudipta Bardhan, SURFSAC Chair
Christopher Bisbee
Brian Collins
Juna Kollmeier
Andrew Strauss
Koen Verbrugghe
Carol Wu
Amalia Zacher

Faculty Editors:

William B. Bridges
Charles J. Brokaw
Sunney I. Chan
Terry Cole
Andrew P. Ingersoll
David B. Rutledge
William M. Whitney

Published by the Caltech Student-Faculty Programs Office
October 18, 1998

Table of Contents

CURJ II

Analysis of the Sea Urchin <i>TEF-1</i> Transcription Enhancer Factor Gene Benjamin H. Mok, Leonard D. Bogarad, and Eric H. Davidson	3
Optimization of a Technique for Visualizing an Activated Protein Kinase in Neural Tissue Kathryn A. Stofer and Mary B. Kennedy	8
Effect of Electrostatic Attraction on the Conformational Distribution of β-Alanine ($+\text{NH}_3\text{CH}_2\text{CH}_2\text{CO}$) Erik W. Streed and John D. Roberts	11
Mutagenesis of the Binuclear Site of the Cu_A Protein Sudipta Bardhan and John H. Richards	18
Engineered Protein-Membrane Interactions Mat E. Barnett and Frances H. Arnold	21
Directed Evolution of a Thermostable Sutilisin Noah Malmstadt and Frances H. Arnold	27
Batch Processes in Combinatorial Auctions: An Experimental Project Pinar Karaca and David P. Porter	34
A Search for High Redshift Quasars Vandana Desai and S. George Djorgovski	41

CURJ III

3D Painting Louis K. Thomas and Peter Schröder	45
Research on Short Frame Turbo Code Alwin Y. Chi and Robert J. McEliece	50
High Efficiency Class-E Power Amplifiers Teo Der-Stepanians and David B. Rutledge	56
Methanol Fuel Cell System Design John F. Christensen and S.R. Narayanan	62
Analysis of Jovian 5-μM Hot Spot Reflectivities Using Hubble Space Telescope Data Andreas C. Tziolas and Glenn S. Orton	69
Analysis of Two Aspects of the Ethylene Signal Transduction Pathway in <i>Arabidopsis thaliana</i> Alfred Wang, Jian Hua, and Elliot M. Meyerowitz	74

Analysis of the Sea Urchin *TEF-1* Transcription Enhancer Factor Gene

Benjamin H. Mok, Leonard D. Bogarad, and Eric H. Davidson

The *TEF-1* gene encodes an enhancer factor that up-regulates the expression of the *CyIIIa* gene. The *CyIIIa* gene is crucial to the development of cytoskeletal actin in the aboral ectoderm of the purple sea urchin (*Strongylocentrotus purpuratus*) embryo. To examine the biochemical and developmental properties of the *TEF-1* gene, its genomic structure and coding sequence were analyzed. 7½ hour and 20 hour arrayed cDNA libraries were screened and several *TEF-1* cDNA clones were isolated. Analysis of these cDNA samples showed that they are of only partial length based on comparisons with homologous genes found in other organisms. To isolate a full length cDNA, two approaches were implemented: (1) Polymerase Chain Reaction (PCR) using degenerate oligonucleotides based on the 5' sequences of related species' *TEF-1* genes. (2) A modified *TEF-1* directed cDNA synthesis method to synthesize the 5' coding region of the *TEF-1* cDNA. For the purpose of delineating the *TEF-1* gene structure, a genomic arrayed library was screened with several cDNA probes derived from coding regions of the *TEF-1* gene. This procedure produced several 50 kilobase-pair potential fosmid clones for fine structure mapping. We are now capable of ascertaining the accurate position of the TEA domain, the 5' position of the promoter, exon/intron density and location, and the start of transcription.

Introduction

The sea urchin *TEF-1* gene is part of a class of transcription factors that contain the TEA domain, a DNA-binding motif. TEA domain proteins are remarkable in sharing this conserved DNA binding domain and are also transcription factors that regulate developmental functions in an assortment of animal and plant phyla (Bürglin, 1991). Apart from the sea urchin *TEF-1* gene, TEA domain genes consist of the following: *ABAA* of *Aspergillus nidulans*, a developmental pathway gene required for the differentiation of asexual spores (Mirabito *et al.*, 1989, Aramayo *et al.*, 1993); *scalloped*, which regulates lineage progression in *Drosophila* sensory neural development (Campbell *et al.*, 1992); and yeast *TEC1*, which is involved in transcriptional activation of the transposon Ty1 (Laloux *et al.*, 1990), among various others.

In mammals, the *TEF-1* transcription factor assists in the activation of tissue specific genes at pivotal stages during development; moreover, it may be one of the most important enhancer activation proteins expressed during mammalian development. The analysis of protein binding sites indicates that the *TEF-1* binds to the same DNA fragment consent sequence (5'-AAGTATGC-3'). Previous experiments of sequence comparisons indicate that the original *SpTEF-1* clone encodes only 90% of the *TEF-1* protein with 50% of the TEA domain (Xiao *et al.*, 1991).

One objective of this investigation was to isolate the entire *TEF-1* gene and the TEA domain coding region from the cDNA through screening arrayed cDNA libraries. This objective was also approached through *TEF-1* directed cDNA synthesis. A second, but equally important, objective was to obtain a fine structure map of the entire *TEF-1* gene through screening a genomic arrayed library and digesting various positive clones for the purposes of delineating the gene structure. We will then be able to ascertain the location of restricting sites, and thus provide the information necessary for future researchers in this field to study the organization and regulation of the entire *TEF-1* gene. By screening the cDNA and genomic libraries, the abundance of the *TEF-1* gene in the sea urchin embryo will also be determined. Through obtaining the genomic DNA, all promoter and regulatory elements will be present to give us definitive properties of the gene.

Materials and Methods

Animals. Embryos of the purple sea urchin, *Strongylocentrotus purpuratus*, were obtained from members of the Davidson group at the Kerckhoff Marine Laboratories and used to prepare the items in the following. *Gallus gallus XJ-RTEF-1A* DNA was provided by C. Ordahl, (University of California, San Francisco, School of Medicine).

Arrayed cDNA Library Screening. An arrayed 7½ hour cDNA library and an arrayed 20 hour cDNA library, each containing 38,000 individual cDNA clones, were screened with cDNA probes approximately 100-600 bp in length derived from partial sequences of the *TEF-1* gene obtained from J. Xian, a member of the Davidson group at Caltech. The time specifications of the libraries show the estimated age of the partially developed animal. The screening was performed following a protocol obtained

through personal communication with H. Lerach, a member of the Davidson group at Caltech.

PCR. The procedure to performing the polymerase chain reaction was modeled after Kirchhamer *et al.*, 1996.

TEF-1 Directed cDNA Synthesis. The directed synthesis of *TEF-1* cDNAs was performed using the Superscript II cDNA library kit of Gibco/BRL with the important modification of using a 30 base oligonucleotide sequence specific to the *TEF-1* gene instead of their oligo-dT primer. This primer contained a unique restriction site, which allowed for the directed cloning of all cDNA products. In our original cDNA screens of arrayed libraries we found *TEF-1* cDNAs at a ratio of 1:10,000 and by this method we found them at a frequency of 1:100. The six longest clones were then sequenced using an ABI Prism kit and an ABI 373A automated sequencer as described by the manufacturers. All cloning, restriction analysis, and colony hybridization were carried out essentially as described by Maniatis *et al.* 1989.

Arrayed Genomic Library Screening. An arrayed fosmid genomic library from the sea urchin was constructed in the pSPORT 1 fosmid vector (Stratagene). The library was screened with probes approximately 100-600 bp in length derived from the previously isolated partial *TEF-1* cDNA strand, provided by J. Xian. Also used was a 600 bp probe derived from the *XJ-RTEF-1A* cDNA from the *Gallus gallus*, which was provided by C. Ordahl. The positive clones were rescreened twice and purified fosmid DNA was prepared by a modified standard lysis protocol for PAC clones.

DNA Sequence Analysis. Clones obtained from the *TEF-1* directed cDNA synthesis approach were sequenced by the transposon method (Strathmann *et al.* 1991), the ExoIII/S1 kit from Pharmacia, and/or using an ABI 373A machine and the manufacturer's recommended protocol, and compiled using IBI software. Multiple sequence alignments were performed using the Clustal V program.

Results

Results from screening the arrayed cDNA libraries. By screening arrayed cDNA libraries, several distinct *TEF-1* sequences of partial length were obtained. These samples were cloned in the pSPORT 1 fosmid vector (by Stratagene), within DH-10b cells (a strain of *E. coli*). By hybridization and digestion, we determined the prevalence of the *TEF-1* cDNA to be 8 positive clones in approximately 80,000 clones total, the entire population of clones screened, which amounts to a ratio of 1:10,000 or 0.01% prevalence. In a cDNA arrayed library, the scarcity of a gene is described as a common transcript with a 1% prevalence, normal with a 0.1% prevalence, and a rare transcript as a 0.01% prevalence. Analysis of these clones led us to conclude that we had acquired no coding regions outside of the 5' end of the *TEF-1* gene that was previously obtained. Thus, we turned to the directed cDNA synthesis approach to produce sublibraries using specific *TEF-1* oligonucleotides as primers.

Results from the *TEF-1* directed cDNA synthesis. A total of eleven sublibraries in the form of bacteria colony lift filters were assembled, each with a positive *TEF-1* clone to negative *TEF-1* clone ratio of approximately 1:100. A total of 40 positive clones were extracted, transformed, amplified, purified, and digested with Pst I and Stu I restriction endonucleases to provide us with information as to the reliability of the synthesized clone's identity and preliminary information as to the amount of novel nucleotides synthesized. These positive clones were then subjected to sequencing. The informative sequence generated by our protocol is 1113 bp in length and encompasses 371 amino acids. The sequencing analysis also provided us with data pertaining to the certification that the clones were in fact *TEF-1*, that an extension in sequence with respect to previous experiments was generated, and that all clones did in fact extend past previously obtained clones. Each of these new clones terminated very near one another, suggesting a secondary structure such as a "hairpin," which caused premature termination of the reverse transcriptase.

Results from screening the arrayed genomic libraries. To obtain the complete genomic region of the *TEF-1* gene, an arrayed sea urchin genomic library was screened using isolated *TEF-1* probes. Several *TEF-1* fragments of approximately 50 kb in length were sequentially isolated. These clones were subjected to extensive restriction endonuclease digestion. The digestion gels were subjected to Southern

blot transfer following Maniatis *et al.* 1989, and the transferred filters were screened with probes approximately 100-600 bp in length derived from the previously isolated partial *TEF-1* cDNA strand, provided by J. Xian. This experiment confirmed that the TEA domain was located in each of the fosmids.

Conclusions

Analysis of clones acquired from screening the arrayed cDNA libraries. We determined that the *TEF-1* gene is very rare, due to the fact that by screening a total of three cDNA libraries, we had only obtained partial length sequences in a scarcity of a 1:10,000 ratio of positive clones to negative clones. This makes *TEF-1* a very rare transcript, which is not necessarily unusual for a transcription regulator.

Analysis of clones acquired from the *TEF-1* directed cDNA synthesis. Applying a directed cDNA synthesis protocol, we determined that the *TEF-1* population was markedly enriched, i.e., the ratio of positive clones versus negative clones was enriched 100 fold, from 1:10,000 to 1:100. In addition, we were able to obtain notably extended sequences as compared to previous experiments in attempting to sequence the entire *TEF-1* cDNA, although the sequencing analysis determined that the clones obtained were still of partial length.

It is possible that the isolation of complete *TEF-1* cDNAs was unattainable because they were subjected to termination during one of the various synthesis steps. cDNAs are known to terminate under various conditions. These abrupt terminations are commonly caused by "hairpins" where the RNA folds onto itself. It is highly probable that the polymerase stopped at a "hairpin." Consequently, we were only able to obtain incomplete, partially synthesized cDNA sequences.

Furthermore, the Mulone reverse transcriptase was used in this experiment. This reverse transcriptase has the characteristic optimal temperature during synthesis of 37° C. We now propose to use the AMV reverse transcriptase in future experiments of the *TEF-1* directed cDNA synthesis. The advantage of using the latter reverse transcriptase is that it functions sufficiently at a higher temperature: 50° C as opposed to 37° C. This higher reaction temperature will aid in destabilizing the hairpin formed by the RNA during the synthesis of the cDNA by the reverse transcriptase. This, along with other modifications should allow the isolation of the full sequence of the *TEF-1* cDNA.

Analysis of clones acquired from screening the arrayed genomic libraries. Several full-length *TEF-1* fragments of approximately 50 kb in length were isolated for fine structure mapping of the gene structure. Important information has been generated that will allow future investigators of the development of the sea urchin to study the organization and regulation of the entire *TEF-1* gene. Specifically, we are now capable of ascertaining the accurate position of the TEA domain, the 5' position of the promoter, exon/intron density and location, and the start of transcription, etc.

Discussion

This investigation resulted in the isolate sea urchin *TEF-1* cDNAs via two separate techniques: one through screening several arrayed cDNA libraries and another through synthesizing *TEF-1* using a directed cDNA synthesis protocol. Our research provided a large genomic clone that contains the *TEF-1* gene which in itself is crucial not only during sea urchin development but is part of a family of genes that are important to the development of all multi-cellular organisms. Current prospects are to continue this investigation of the full-length *TEF-1* cDNA coding region. The *TEF-1* gene's functional properties in regulating developmentally expressed genes will be identified and explored. Homology in the gene (especially in the TEA domain) with respect to functionally similar genes found in various organisms such as the chicken (*Gallus gallus*), mouse (*Mus musculus*), and fruit fly (*Drosophila melanogaster*), will be examined.

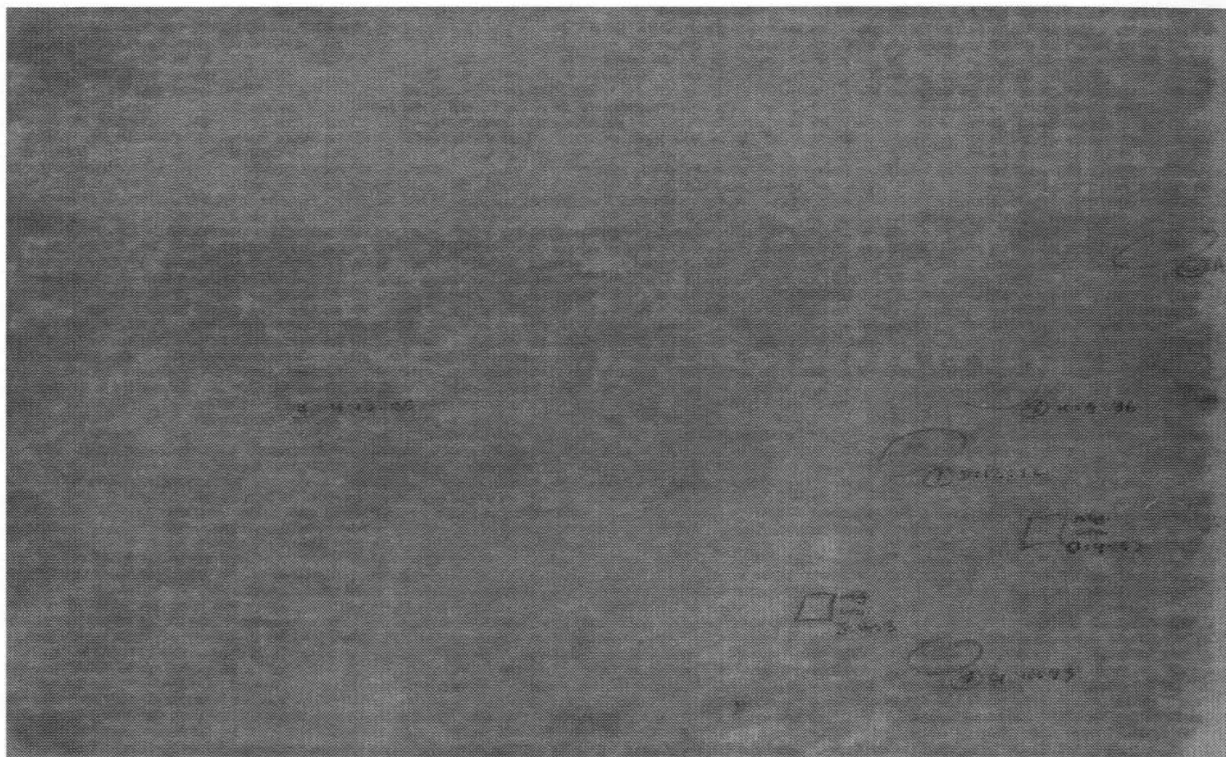


Figure 1. An x-ray film of an arrayed genomic library screened with a *TEF-1* probe derived from the sequenced 3' end of the gene. In this example five positive clones (D:12:12, A:2:2, H:9:36, G:11:33, H:13:25) were selected for the purpose of delineating the *TEF-1* gene structure and two negative clones (O:9:33, J:16:3) were selected as controls.

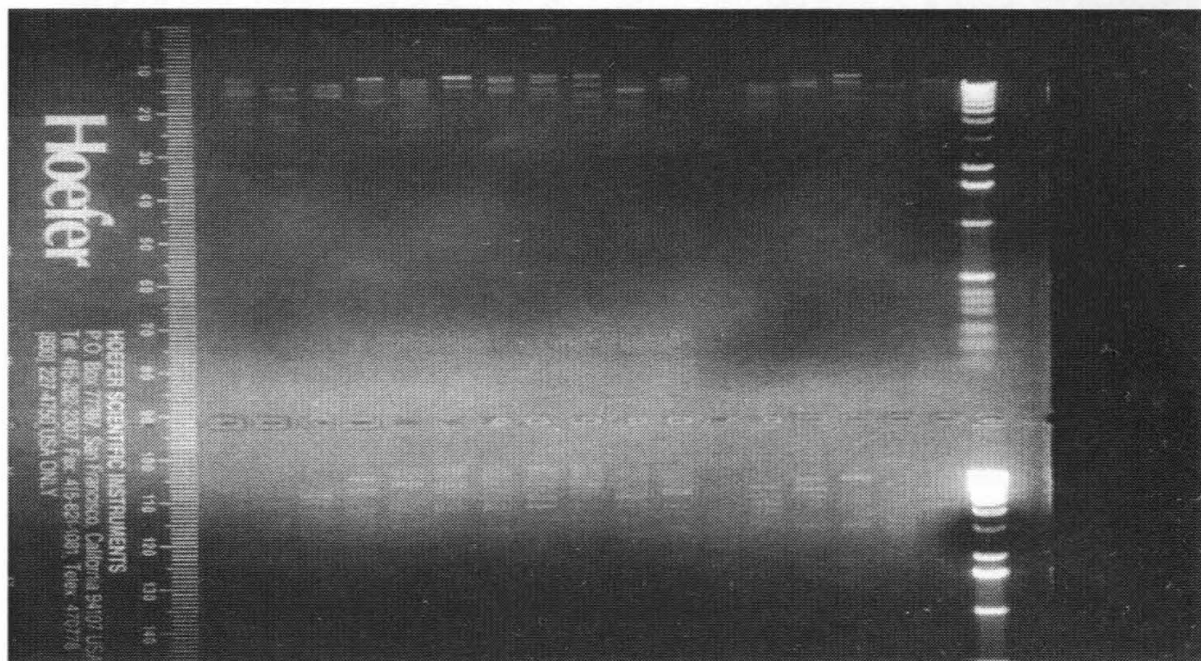


Figure 2. An electrophoresis gel showing a restriction endonuclease analysis of a positive clone selected from screening an arrayed genomic library. The top row shows 17 samples digested with various restriction endonucleases ranging from *Acc I* to *Hind III* to *Xho I*. The bottom row shows 16 samples double-digested with the same previously mentioned enzymes plus *Hind III*. After screening the Southern blot filters transferred from gels such as these, the bands that include the TEA domain were singled out and subjected to fine structure mapping.

Acknowledgements

The author is indebted to Leonard D. Bogarad for his mentorship and discussion, and Eric H. Davidson, Pedro Martinez, Youn-Ho Lee, and Ted Biondi for technical assistance and valuable critical review of the manuscript. This work was supported by the Samuel P. and Frances Krown SURF Endowment Fund and the 1996 Summer Undergraduate Research Fellowships Program at the California Institute of Technology.

References

- Aramayo, R., and Timberlake, W. E., "The *Aspergillus nidulans* YA gene is regulated by ABAA," *EMBO*, Vol. 12, 2039-2048, 1993.
- Bürglin, T. R., "The TEA Domain: a Novel, Highly Conserved DNA-binding Motif," *Cell*, Vol. 66, 11-12, 1991.
- Calzone, F. J., Höög, C., Teplow, D. B., Cutting, A. E., Zeller, R. W., Britten, R. J., and Davidson, E. H., "Gene regulatory factors of the sea urchin embryo. I. Purification by affinity chromatography and cloning of P3A2, a novel DNA binding protein," *Development*, Vol. 112, 335-350, 1991.
- Campbell, S., Inamdar, M., Rodriguez, V., Raghavan, K. V., Palazzolo, M., and Chovnick, A., "The scalloped gene encodes a novel, evolutionarily conserved transcription factor required for sensory organ differentiation in *Drosophila*," *Genes & Dev.*, Vol. 6, 367-379, 1992.
- Casaz, P., Sundseth, R., and Hansen, U., "Transactivation of the simian virus-40 late promoter by large T-antigen requires binding-sites for the cellular transcription factor *TEF-1*," *J. Virol.*, Vol. 65, 6535-6543, 1991.
- Coffman, J. A., Moore, J. G., Calzone, F. J., Hood, L. E., Britten, R. J. and Davidson, E. H., "Automated sequential affinity chromatography of sea urchin embryo DNA binding proteins," *Mol. Marine Biol. & Biotech.*, Vol. 1, 136-146, 1992.
- Coulombe, J., Berger, L., Smith, D. B., Hehl, R. K., and Wildeman, A. G., "Activation of simian virus-40 transcription *in vitro* by T-antigen," *J. Virol.*, Vol. 66, 4591-4596, 1992.
- Gruda, M. C., Zabolotny, J. M., Xiao, J. H., Davidson, I., and Alwine, J. C., "Transcriptional activation by simian virus-40 large T-antigen interactions with multiple components of the transcription complex," *Mol. Cell Biol.*, Vol. 13, 961-969, 1993.
- Hwang, J., Chambon, P., and Davidson I., "Characterization of the transcription activation function and the DNA binding domain of transcription enhancer factor-1," *EMBO*, Vol. 12, 2337-2348, 1993.
- Ishiji, T., Lacey, M. J., Parkkinen, S., Anderson, R. D., Haugen, T. H., Cripe, T. P., Xiao, J. H., Davidson, I., Chambon, P., and Turek, L. P., "Transcriptional enhancer factor *TEF-1* and its cell-specific co-activator activate human papillomavirus-16 E6 and E7 oncogene transcription in keratinocytes and cervical-carcinoma cells," *EMBO*, Vol. 11, 2271-2281, 1992.
- Kania, A., Bonner, A. S., Duffy, J. B., and Gergen, J. P., "The *Drosophila* segmentation gene runt encodes a novel nuclear regulatory protein that is also expressed in the developing nervous system," *Genes & Dev.*, Vol. 4, 1701-1713, 1990.
- Kirchhamer, C. V. and Davidson, E. H., "Spatial information processing in the sea urchin embryo: Modular and intramodular organization of the *CyIIIa* gene cis-regulatory system," *Development*, Vol. 122, 333-348, 1996.
- Laloux, I., Dubois, E., Dewerchin, M., and Jacobs, E., "A gene involved in the activation of Tyl and Tyl-mediated gene-expression in *Saccharomyces cerevisiae*-cloning and molecular analysis," *Mol. Cell Biol.*, Vol. 10, 3541-3550, 1990.
- Leahy, P. S., "Laboratory culture of *Strongylocentrotus purpuratus* adults, embryos, and larvae," *Meth. Cell Biol.*, Vol. 27, 1-13, 1986.
- Levanon, D., Negreanu, V., Bernstein, Y., Bar-Am, I., Avivi, L. and Groner, Y., "AML1, AML2, AML3, the human members of the runt domain gene-family: cDNA structure, expression, and chromosomal localization," *Genomics*, Vol. 23, 425-432, 1994.
- Makabe, K. W., Kirchhamer, C. V., Britten, R. J. and Davidson, E. H., "Cis-regulatory control of the *SM50* gene, an early marker of skeletogenic lineage specification in the sea urchin embryo," *Development*, Vol. 121, 1957-1970, 1995.
- Maniatis, T., Sambrook, J., Fritsch, E. F., *Molecular Cloning: A Laboratory Manual* New York: Cold Spring Harbor Laboratory Press, 1989.
- Mirabito, P. M., Adams, T. H. and Timberlake, W. E., "Interactions of three sequentially expressed genes control temporal and spatial specificity in *Aspergillus* Development," *Cell*, Vol. 57, 859-868, 1989.
- Miyoshi, H., Kozu, T., Shimizu, K., Enomoto, K., Maseki, N., Kaneko, Y., Kamada, N., and Ohki, M., "The t(8;21) translocation in acute myeloid leukemia results in production of an AML1-MTG8 fusion transcript," *EMBO*, Vol. 12, 2715-2721, 1993.
- Ogawa, E., Maruyama, M., Kagoshima, H., Inuzuka, M., Lu, J., Satake, M., Shigesada, K., and Ito, Y., "PEBP2/PEA2 represents a family of transcription factors homologous to the products of the *Drosophila* runt gene and the human *AML1* gene," *Proc. Natl. Acad. Sci. USA*, Vol. 90, 6859-6863, 1993.
- Ransick, A., Ernst, S., Britten, R. J., and Davidson, E. H., "Whole mount *in situ* hybridization shows *Endo 16* to be a marker for the vegetal plate territory in sea urchin embryos," *Mech. Dev.*, Vol. 42, 117-124, 1993.
- Sakakura, C., Yamaguchi-Iwai, Y., Satake, M., Bae, S.-C., Takahashi, A., Ogawa, E., Hagiwara, A., Takahashi, T., Murakami, A., Makino, K., Nakagawa, T., Kamada, N., and Ito, Y., "Growth inhibition and induction of differentiation of t(8;21) acute myeloid leukemia cells by the DNA-binding domain of PEBP2 and the AML1/MTG8(ETO)-specific antisense oligonucleotide," *Proc. Natl. Acad. Sci. USA*, Vol. 91, 11723-11727, 1994.
- Seed, B. and Sheen, J.-V., "A simple phase-extraction assay for chloramphenicol acetyltransferase activity," *Gene*, Vol. 67, 271-277, 1989.
- Stewart, A. F. R., Larkin, S. B., Farrance, I. K. G., Mar, J. H., Hall, D. E., Ordahl, C. P., "Muscle-enriched TEF-1 isoforms bind M-CAT elements from muscle-specific promoters and differentially activate transcription," *Jour. Bio. Chem.*, Vol. 269, 3147-3150, 1994.
- Strathman, M., Hamilton, B. A., Mayeda, C. A., Simon, M. I., Meyerowitz, E. M., and Pallazzolo, M. J., "Transposon-facilitated DNA sequencing," *Proc. Natl. Acad. Sci. USA*, Vol. 88, 1247-1250, 1991.
- Thézé, N., Calzone, F. J., Thiebaud, P., Hill, R. L., Britten, R. J., and Davidson, E. H., "Sequences of the *CyIIIa* actin gene regulatory domain bound specifically by sea urchin embryo nuclear proteins," *Mol. Reprod. & Dev.*, Vol. 25, 110-122, 1990.
- Wang, D. G.-W., Kirchhamer, C. V., Britten, R. J. and Davidson, E. H., "SpZ12-1, a negative regulator required for spatial control of the territory-specific *CyIIIa* gene in the sea urchin embryo," *Development*, Vol. 121, 1111-1122, 1995.
- Xiao, J. H., Davidson, I., Matthes, H., Garnier, J. M., and Chambon, P., "Cloning, expression, and transcriptional properties of the human enhancer factor *TEF-1*," *Cell*, Vol. 65, 551-568, 1991.
- Yuh, C.-H., Ransick, A., Martinez, P., Britten, R. J., and Davidson, E. H., "Complexity and organization of DNA protein interactions in the 5'-regulatory region of an endoderm-specific marker gene in the sea urchin embryo," *Mech. Dev.*, Vol. 47, 165-186.

Optimization of a Technique for Visualizing an Activated Protein Kinase in Neural Tissue

Kathryn A. Stofer and Mary B. Kennedy

Calcium/Calmodulin-dependent protein kinase II (CaMKII) has been identified as an important molecule in hippocampal long-term potentiation (LTP), a form of synaptic modification thought to be an essential part of the mechanism of encoding memories. Studying the relative amounts and distribution of active, autophosphorylated CaMKII in the hippocampus during LTP gives insight into the molecule's function and the process of LTP. The Kennedy lab has developed a technique of fluorescence immunochemical labeling with fluorescent antibodies specific for either active CaMKII or inactive CaMKII utilizing a laser-scanning confocal microscope (LCSM) to visualize their distribution. The purpose of this research has been to perfect this new technique by elucidating the relationship between antibody concentration and brightness values obtained with the LCSM. We have determined an optimum concentration for the antibodies against both active and inactive CaMKII.

Introduction

A major focus of neurobiological research in recent years has been understanding the mechanism of memory formation and storage. Little is known of an overall picture of how the brain translates images and sounds into memories, much less of the physical and chemical changes in the tissue that underlie the process. One of the most significant discoveries in this field has been long-term potentiation (LTP) in the hippocampus, a form of synaptic modification that may underlie the early encoding of memories. This phenomenon involves an increase in the strength of synaptic transmission produced by a high-frequency stimulus to those synapses. Calcium-Calmodulin dependent protein kinase II (CaMKII) is one molecule known to be activated during this high-frequency stimulus and is thus thought to be an important player in LTP.¹ Knockout mice deficient in the α isoform of CaMKII have been shown to be deficient in LTP and impaired in spatial learning tasks such as the Morris water maze, corroborating the theoretical connection between LTP and spatial memory.²

One of the hallmarks of CaMKII activation is autophosphorylation of the kinase at Threonine-286 (287 in the β isoform) that causes the kinase to remain active in the absence of calcium.¹ The autophosphorylated kinase is then hypothesized to phosphorylate neighboring receptors and channels such as AMPA-type glutamate receptors, inducing their increased activity, perhaps contributing to the "maintenance phase of LTP."

The Kennedy lab is exploring the relative amounts of autophosphorylated CaMKII in hippocampal synapses before and after LTP-inducing stimuli. This measurement is accomplished by fluorescence immunochemical labeling of the autophosphorylated site and laser-scanning confocal microscopy. The lab recently developed a technique for staining hippocampal slices to measure and visualize CaMKII autophosphorylation^{3,4} and was interested in clarifying the importance of a few variables to perfect and normalize their results. The variable examined in this study was the concentration of phospho- and nonphospho- primary antibody used to label the slices. We discovered that the relationship of both the phospho- and nonphospho- primary antibodies to the brightness of the staining was linear, thus proving that comparisons between experiments can be made in a simple manner.

Materials and Methods

Two primary antibodies were studied using single-labeling techniques. These antibodies recognize the site of autophosphorylation in CaMKII, Threonine-286. Mouse monoclonal antibody 22B1 is specific for the phosphorylated form of the kinase, and rabbit polyclonal antibody Sylvia is specific for the nonphosphorylated form (Patton *et al.*, 1993). The distribution of these primary antibodies in the hippocampus was then visualized by means of secondary antibodies coupled to fluorescent dyes: FITC-conjugated goat anti-mouse antibody specific to 22B1, and Cy3-conjugated goat anti-rabbit antibody specific to Sylvia. The GAM-FITC was purchased from Cappel and the GAR-Cy3 from Chemicon.

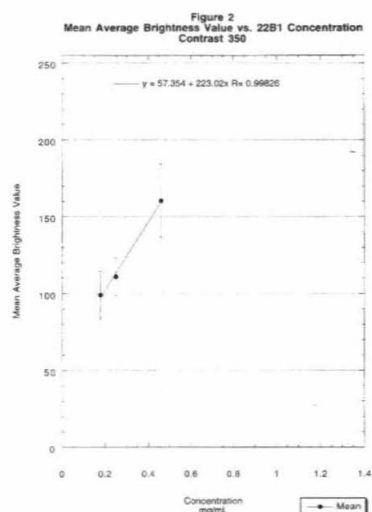
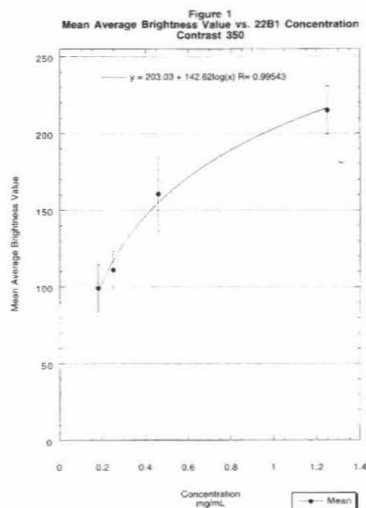
41-54 day old rats were anaesthetized with 1 ml Halothane until there was no hind foot reflex. The rats were decapitated and the brain rapidly removed and placed immediately in ice cold ACSF (Ringer's) solution (119mM NaCl, 2.5mM KCl, 1.3mM MgSO₄·2H₂O, 2.5 mM CaCl₂·2H₂O, 1 mM NaH₂PO₄·H₂O, 26.2 mM NaHCO₃, 11mM Dextrose) that had been bubbled with 95% O₂/5% CO₂ for

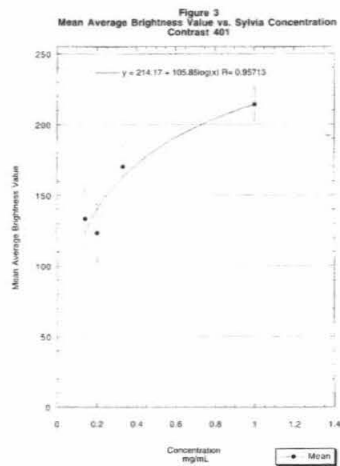
15 minutes beforehand. The hippocampus was removed from both halves of the brain and cut into 500 μm slices using a Stoelting slicer, then slices rested 2 hours on Whatman #5 filter paper over a petri dish of Ringer's in a plastic chamber oxygenated continuously with 95% O_2 /5% CO_2 bubbled through distilled water. Slices were fixed one hour in ice cold 4% paraformaldehyde/0.2% glutaraldehyde in 0.1 M NaPO_4 buffer pH 7.4, then left in PBS (20mM NaPO_4 buffer pH 7.4, 0.9% NaCl) at 4 °C overnight. 4 slices were cut into 4-6 50 μm sections each with a sapphire blade vibratome and placed in a 24-well plate in cold PBS. Sections were then treated as follows (0.5 ml except where indicated): 0.7% triton-x 100 in PBS, 1 hour; PBS, 2X five minutes; 0.1 M glycine in PBS, 1 hour; ddH₂O, 2X five minutes; 0.1% Sodium Borohydride, 20 minutes; ddH₂O, 2X five minutes; blocking buffer (5% normal goat serum, 450 mM NaCl, 0.05% triton-x 100 in 20 mM NaPO_4 buffer), 1.5 hours to reduce background. 230 μl of primary antibody (22B1 for phosphorylated, Sylvia for nonphosphorylated CaMKII) was then added in dilutions of 1:10, 1:30, 1:50, and 1:70 in blocking buffer, one dilution per 500 μm slice. Sections were incubated in primary antibody overnight (≥ 8 hours) at 4 °C, then washed 3X thirty minutes in blocking buffer, and incubated 1 hour in 230 ml secondary antibody - 1:5 GAMF against phosphorylated CaMKII, 1:50 GARCy3 against non-phosphorylated CaMKII dilutions in blocking buffer. Next came thirty minute wash in blocking buffer, 2X thirty minutes wash in PBS, and post-fix in 2% paraformaldehyde in PBS 5 minutes, wash 2X five minutes in PBS. Sections were transferred to 1M NaHCO_3 buffer, pH 9.2, for 1 minute, then mounted in 4% n-propyl gallate, 90% glycerol in carbonate buffer. Edges were sealed with clear nail polish, and slides were frozen after allowing 2 hours for glycerol penetration. Each primary antibody was tested twice, producing a total of 8 slices per antibody (two per each dilution).

Sections were photographed using a Zeiss laser-scanning confocal microscope using a 10X lens (pinhole 20, theoretical optical section ~ 20 μm) at 488 nm for Fluorescein and 543 nm for Cy3 excitation. The brightness was set at 9601 and contrast was 350 for Fluorescein, 401 for Cy3, settings previously used by the Kennedy lab. The CA1 region was photographed at the brightest optical section, images were stored and transferred to a Macintosh computer. Using MacPhase software (Otter Solutions), the dendrites of the CA1 were selected as a "region of interest (ROI)" and their average brightness value calculated. The average brightness value of all 10-12 sections of each dilution (eg. 1:10 22B1) were subsequently averaged and plotted versus concentration of primary antibody in which the tissue was incubated. Curves were fitted using Kaleidagraph software.

Results

The best fit for the phosphokinase data was a logarithmic curve, showing the effect of $\geq 10\%$ saturation in the image at concentration 1.25 mg/ml, contrast 350 (Figure 1), causing deviation from linearity. The lower three concentrations, which did not cause images that were $\geq 10\%$ saturated, showed a simple linear increase in image brightness with an increase in 22B1 concentration (Figure 1). Similar results were gathered from the nonphosphokinase: a logarithmic best fit (Figure 2) due to saturation of the image pulling the curve from linearity demonstrated in the three lower concentrations (Figure 2) at contrast 401.





Discussion

The data for the phosphorylated kinase are best fit with a logarithmic curve, as shown in Figure 1. The fact that this curve has not reached saturation at the concentrations of antibody we have studied indicates that the amount of primary antibody is currently the limiting factor in the amount of signal produced, rather than the amount of secondary antibody or limitations of the microscope. The lack of saturation also reveals that there is no lack of phosphorylated kinase in the tissue. The linearity of the curve in the region of the concentrations of 0.46, 0.25 and 0.18 mg/ml provides reassurance that comparisons between different experiments photographed at different contrasts are indeed valid and the relation is straightforward. The results for the nonphosphorylated kinase are similar: an unsaturated logarithmic curve indicating that the primary antibody is the limiting factor, and a linear region indicating validity of comparisons between experiments.

These results further indicate that in both the phosphorylated and nonphosphorylated cases, a concentration of 0.46 mg/ml may be more useful to use in other experiments than the 0.25 mg/ml that has been used previously by the lab. The higher concentration will allow more kinase to be tagged, producing an image with more information, yet still be cost efficient. As the curve deviates from linearity at concentrations greater than ~0.5 mg/ml, there is less return in signal for the cost of using greater amounts of expensive antibody, so 0.5 mg/ml seems to be the point at which the most information is returned for a reasonable cost.

These are important findings for the study of both the phosphorylated and nonphosphorylated forms of CaMKII. Individual experiments can indeed be optimized in terms of contrast to obtain the best images for any given conditions, including antibody concentration, and the data between experiments have a straightforward relationship to facilitate comparison. Also, primary antibody concentrations are the limiting factors in the studies, i.e. there is no limitation of the equipment causing loss of information, so a concentration of ~0.5 mg/ml seems to be a better choice than the 0.25 mg/ml used previously in terms of the most information without excessive expense.

Acknowledgements

Many thanks to Professor Mary Kennedy, my sponsor, Leslie Schenker, Yannan Ouyang, and David Kantor for instruction and technical assistance, and the members of the Kennedy lab.

Funding provided by: National Institute of Mental Health grant MH49176 to MBK, Mr. and Mrs. William B. Hicks, and the SURF program.

References:

- Hall, Zach W., et al. *An Introduction to Molecular Neurobiology*. Sunderland, Massachusetts: 1992. pp. 463-495.
- Silva, Alcino J., Richard Paylor, Jeanne M. Wehner, and Susumu Tonegawa. "Impaired Spatial Learning in a-Calcium-Calmodulin Kinase II Mutant Mice." *Science*, vol. 257, 206-210, 10 July 92.
- Patton, Bruce S., Sean S. Molloy, and Mary B. Kennedy. "Autophosphorylation of Type II CaM Kinase in Hippocampal Neurons: Localization of Phospho- and Dephosphokinase with Complementary Phosphorylation Site-Specific Antibodies." *Mol. Biol. Cell*, vol. 4, 159-172, February 1993.
- Kindler, Stefan S. and Mary B. Kennedy. "Visualization of Autophosphorylation of Ca²⁺/Calmodulin-Dependent Protein Kinase II in Hippocampal Slices." *J. Neurosci. Meth.*, in press.

Effect of Electrostatic Attraction on the Conformational Distribution of β -Alanine ($^+\text{NH}_3\text{CH}_2\text{CH}_2\text{CO}$)

Erik W. Streed and John D. Roberts

Proton nuclear magnetic resonance (^1H NMR) was employed to study the conformational equilibrium of β -alanine in solvent systems with known dielectric constants. Extensions of the Karplus equation^{3,4,6} were used to determine coupling constants for different conformations. From the observed coupling constants and the calculated couplings for different conformations, the distributions of gauche and trans conformations were determined. The observed coupling constant between the $-\text{CH}_2-\text{CH}_2-$ hydrogens varied from 6.630 Hz to 6.688 Hz over a solvent dielectric constant range from 30 to 80. The results do not indicate a strong change in conformational preference with changes in the dielectric constant of the solvent system.

Introduction

Electrostatic interactions play a fundamental role in many biochemical reactions, such as those involving amino acids, peptides, and proteins. One of the ways that electrostatics affect reactions is by contributing to the stabilities of certain molecular conformations. Peptides and proteins can have hundreds or thousands of differing conformations, with electrostatic attractions contributing to the stability of some, while inhibiting others. To understand larger conformation phenomena fully, we must be able to understand and accurately predict the conformational distributions of the simple amino acids. Accurate prediction of the influence of electrostatic interactions on the conformations of amino acids is important for creating working models of larger phenomena such as protein formation and folding.

Coulomb's Law predicts the force F between two points with charges q_1 and q_2 that are separated by a distance r (figure 1). When the region between the charges is filled with a homogeneous material (gas, solvent, solid, etc.) the electrostatic force is reduced inversely with respect to the dielectric constant ϵ of that material (figure 1). This relationship is the basis of all electrostatic interactions. Unpolarized hydrocarbons have dielectric constants in the range of 2 or 3. Most protein interactions take place in water, which has the high electric constant of 80. Solvation reduces the strength of the electrostatic interactions by a factor of ~ 40 when moved from a polar to a non-polar environment.

One of the simplest amino acids in which electrostatic interactions should be observed is the 1,2-disubstituted ethane, β -alanine. In the zwitterionic state, it has both positively and negatively charged groups which are separated by two carbon-carbon bonds (figure 2). This provides the molecule with a degree of rotational freedom in which the distance between the charged groups varies.

β -Alanine has three different staggered rotational conformations about the carbon-carbon axis. For 1,2-disubstituted ethanes, these conformations are designated based on the relationships of the substituted groups. The gauche conformations of β -alanine are enantiomers and have the two substituted groups adjacent to each other, minimizing the distance between them. In the trans conformation of β -alanine the substituted groups are opposite each other, maximizing the distance between them.

Electrostatic theory suggests that in the gas phase β -alanine would strongly prefer the gauche conformation over the trans conformation with reduced distance between the oppositely charged groups (figure 3). The force between the charged groups is inversely proportional to the dielectric constant (ϵ) between them. As ϵ increases the influence of electrostatic attraction decreases and the expected distribution tends toward the statistical $1/3$ trans and $2/3$ gauche conformer. And as ϵ is lowered the influence of electrostatic interaction is increased, which should favor the gauche conformers. By changing the dielectric constant ϵ of the solvent system surrounding β -alanine, we hoped to observe this effect.

Proton nuclear magnetic resonance spectroscopy (^1H NMR) allows for quantitative determination of the distribution of rotational isomers of 1,2-disubstituted ethanes through the measurement of the $3 J_{\text{HH}}$ coupling constants. The hydrogen-hydrogen couplings $J_{\text{H,H}}$ for the gauche and trans conformations are expected to be quite different. NMR spectrometers have poor time resolution, so ethanes such as β -alanine that have low rotational barriers are subject to rotational time averaging of their

coupling constants. Hence only the mean coupling constants can be measured experimentally. To deduce the conformational equilibrium from the mean coupling constants requires predicted values for the coupling constants of each different conformational state. Several methods are available today to calculate the coupling constants for different conformations of 1,2-disubstituted ethanes such as β -alanine.^{3,4,6}

Molecular quantum mechanics modeling of β -alanine⁵ predicts that, in the gas phase, the gauche conformations are more stable than the trans by 25 kcal/mole and that the gauche conformations are most stable with a dihedral angle of 55°. When β -alanine is placed in an environment where the molecule is surrounded by a bulk dielectric constant of 80 (simulating water solvation), the situation changes drastically. The trans conformation is 3.9 kcal/mole more stable than the gauche conformation. The most stable gauche conformation now has the ideal dihedral angle of 60°. However, when the dielectric constant ϵ is lowered from 80 (water) to 30, the estimated difference between the trans and gauche conformations drops to 0.2 kcal/mole. These calculations indicate that a large change in the rotational equilibrium should occur as the solvent dielectric constant ϵ is lowered. It must be noted that molecular quantum mechanics modeling normally works through energy-minimized structures and hence may or may not fully account for thermal effects.

Materials and Methods

Solvent systems of known dielectric constants were created by mixing either methanol (MeOH) or ethanol (EtOH) with heavy water (D_2O). Samples were prepared by adding sufficient β -alanine in 1.0 ml of solvent system to create ~0.1 M solutions. p-Dioxane was added as an internal reference standard. (3.700 ppm, 1111 Hz for 300 MHz NMR relative to TMS).

The samples were segregated into two different groups: methanol/ D_2O (MD) and ethanol/ D_2O (ED) based solvent systems. The sample having only D_2O and β -alanine was considered to be part of both groups and was treated accordingly. The group of methanol-containing samples were made with both fully deuterated methanol (MeOH- d_4 , a lockable solvent for NMR) and undeuterated methanol (not an NMR lockable solvent). To check that the deuterated solvent was behaving equivalently to the undeuterated solvent, samples were prepared using the same mole fraction of each type of methanol. The observed spectra were in agreement with each other.

Spectra were taken using General Electric QE PLUS 300-MHz Fourier Transform nuclear magnetic resonance (FT-NMR) spectrometers. Nuclear magnetic resonance spectra were acquired at known, constant temperatures. These spectra showed triplets centered at 3.108 ppm and 2.485 ppm derived from β -alanine. Four spectra containing between 4 and 16 usable coupling constants (J) were acquired for each sample. Resolutions ranged from $\sim \pm 0.03$ Hz/point to $\sim \pm 0.09$ Hz/point. Line broadening of up to 1.00 Hz and baseline correction were applied to reduce noise.

Before spectra were taken, samples were placed in the NMR room for at least 30 minutes so that thermal equilibrium could be reached (room temperature $\sim 16.5^\circ C$.) Several spectra of each sample were then taken in series. Concerns over possible temperature drift were alleviated by doing the first ED set of spectra in two sequential series instead of acquiring four spectra at a time. Analysis of the coupling constants showed no indication of temperature drift so all further spectra were taken in one run of four spectra each.

Calculations

To determine the distribution of rotational isomers from the experimentally observed coupling constant, the coupling constants for the individual isomers must be calculated. There are several methods of computing these values. The Karplus equation (figure 4) gives the hydrogen-hydrogen coupling $J_{H,H}$ for ethane in terms of the dihedral angle θ between the hydrogens. This equation does not take into account the effect of substituted groups on the hydrogen-hydrogen coupling. Abraham,⁶ Altona,³ Haasnoot,⁴ and others have improved on the accuracy of the Karplus equation by adding corrections to the coefficients based on the substituted groups.

Wyman² gives an empirical formula for the dielectric constant (ϵ) in terms of temperature (T , in °C) of specific ethanol/water mixtures using a quadratic fit to $\epsilon = a + b(T-20) + c(T-20)^2$. The parameters a , b , and c are given for specified ethanol/water mixtures tested by Wyman.² The mixtures of ethanol and water used by Wyman² need to be corrected for the effects of substituting EtOD/D₂O for EtOH/H₂O. This was done by holding the mole fraction of each solvent constant while calculating new volume percentages. The resulting changes in concentration by volume were less than 5%.

A formula similar to Wyman for the dielectric constants of methanol based mixtures was not found in the literature. The dielectric constant ϵ was calculated by an inverse weighted sum. The inverse dielectric constant $1/\epsilon$ for the pure solvents was weighted by the mole fraction of that particular solvent in the system. Summation of these values gives $1/\epsilon$ for the mixture of solvents. Unfortunately, this method does not allow the temperature correction possible with the EtOD/D₂O solvent systems. Fortunately, the dielectric constants for water and methanol are commonly measured at 20°C which is close to our operating temperature of 16.5°C.

Results

Figures 5 and 6 show the experimentally observed coupling constants J plotted against a measure of the reduction in electrostatic force $1/\epsilon$. Because the NMR spectra that were acquired showed only triplets, it is safe to assume that $J_{13} \sim J_{14}$. Computation of line shapes with line widths corresponding to the ones observed show that J_{13} and J_{14} could differ by about ± 0.9 Hz before the triplet line shapes would visibly distort. This corresponds to about a $\pm 9\%$ change in conformation at equilibrium or about 0.25 kcal/mole change in free energy (ΔG).

Discussion

The observed small changes in coupling constant J with ϵ for β -alanine are consistent with Wei's study of β -alanine conformation distribution in DMSO/D₂O relative to temperature. However, these results do not agree with the previously mentioned quantum mechanical models of Brameld and Goddard which predict the trans conformer will be more stable in water by about 4 kcal/mole.

These discrepancies may be explained in terms of assumptions made about the environment in which a β -alanine molecule is solvated. For example, the effects of the solvent hydroxyl (-OH) groups interacting directly with the β -alanine were not taken into account in quantum calculations. Because of the low ($\sim 0.1M$) concentration, intermolecular interaction between β -alanine molecules was not considered to be relevant to this study.

A fundamental difficulty in this research centers on the solubility of β -alanine in various solutions. A zwitterionic molecule, it dissolves well in highly polar solvents. Unfortunately, the most interesting data on electrostatic effects are expected to come from solvent systems with the lowest possible ϵ (non-polar solvents). Common experimental "tricks" such as using crown ethers to draw ions into solutions are not viable because the solvated zwitterionic state of β -alanine is needed to study the desired effects.

As the dielectric constant increases towards infinity, one would expect to find that the electrostatic influence on the conformation distribution would approach zero. The coupling constant at this point should be that for the statistical distribution of $1/3$ trans and $2/3$ gauche. From the linear fits, this would place β -alanine's coupling constant (J) in the neighborhood of 6.87 ± 0.03 Hz. This is a reasonable value considering how little change in the observed coupling constant has occurred over the fairly wide range of dielectric constants tested.

Extrapolating from the linear fit's for solvent systems of lower dielectric constant does not produce a similarly satisfactory result. As the dielectric constant decreases so should β -alanine's coupling constants. When ϵ is in the range of 2 or 3 (benzene, carbon tetrachloride, pentane) the observed linear fit (figures 5 and 6) suggests the physically unrealistic result that the coupling constant J would drop to nothing and the peaks would coalesce into a singlet.

Conclusions

Minimal changes in the distribution of rotational conformations for β -alanine with solvent systems of varying dielectric strength suggest that electrostatics may play a different role than is reflected in current models. A linear relationship is observed (for ϵ from 30 to 80) between the dielectric constant ϵ of the solvent system and the observed coupling constant (J) of β -alanine. However, the change in J with respect to ϵ is not nearly as large as might be expected. Moreover, the linear fit suggests that as ϵ decreases to around 2 or 3 the coupling would approach zero. This is not physically realistic and it is more likely that the change in J reflects a small change in the conformational equilibrium constant. Consequently, if J changes much more we expect to observe a more complex spectrum. In conclusion, these interesting results provide a basis for further studies of the effect of electrostatic interactions in β -alanine..

$$F = \frac{1}{\epsilon} \frac{q_1 q_2}{r^2}$$

Figure 1. Coulomb's Law
(CGS units)

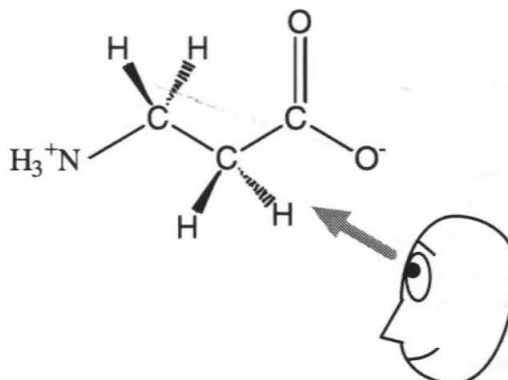


Figure 2. Trans conformation of β -alanine zwitterion

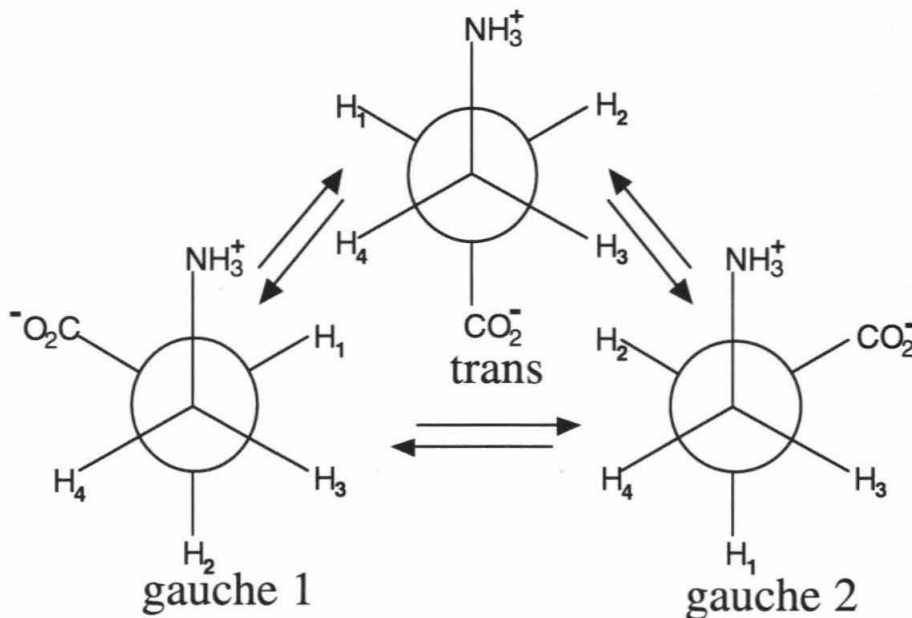
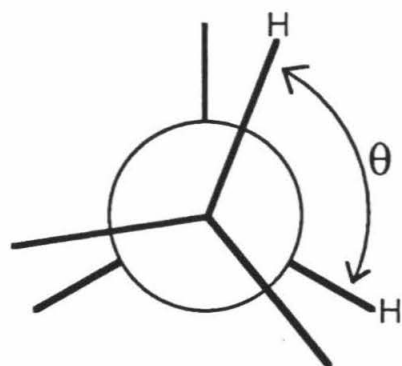


Figure 3. Rotational conformations of β -alanine zwitterion



$$J(\text{H,H}) = 7.0 - 1.0 \cos(\theta) + 5.0 \cos(2\theta)$$

Figure 4. The Karplus Equation

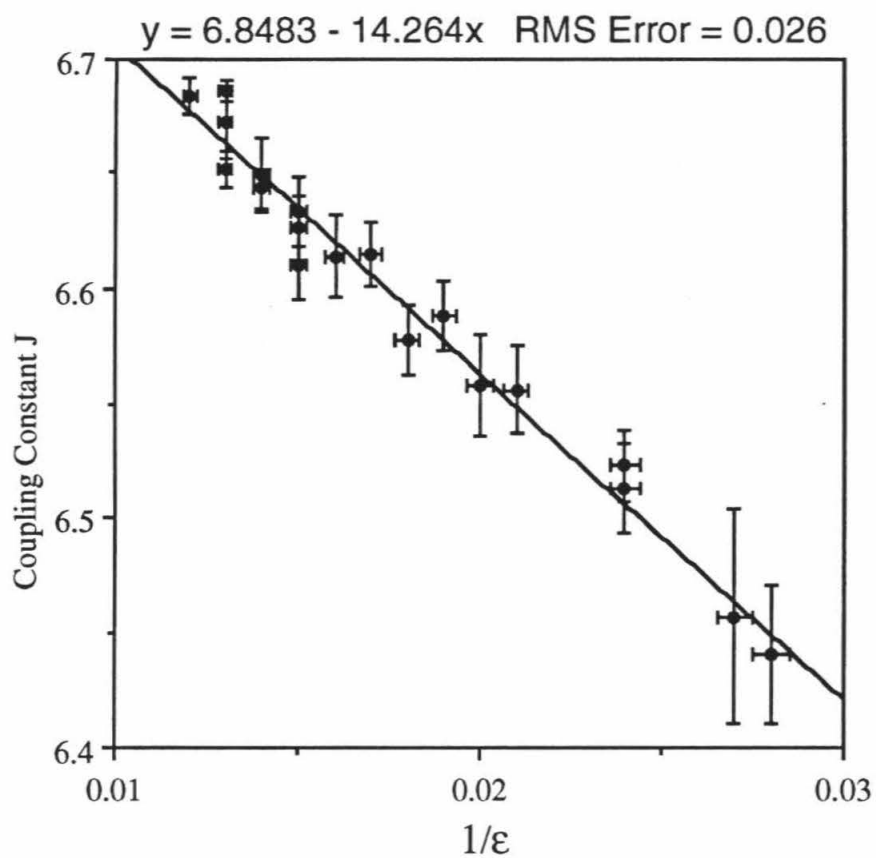


Figure 5. β -alanine dissolved in EtOH/D₂O solvent systems

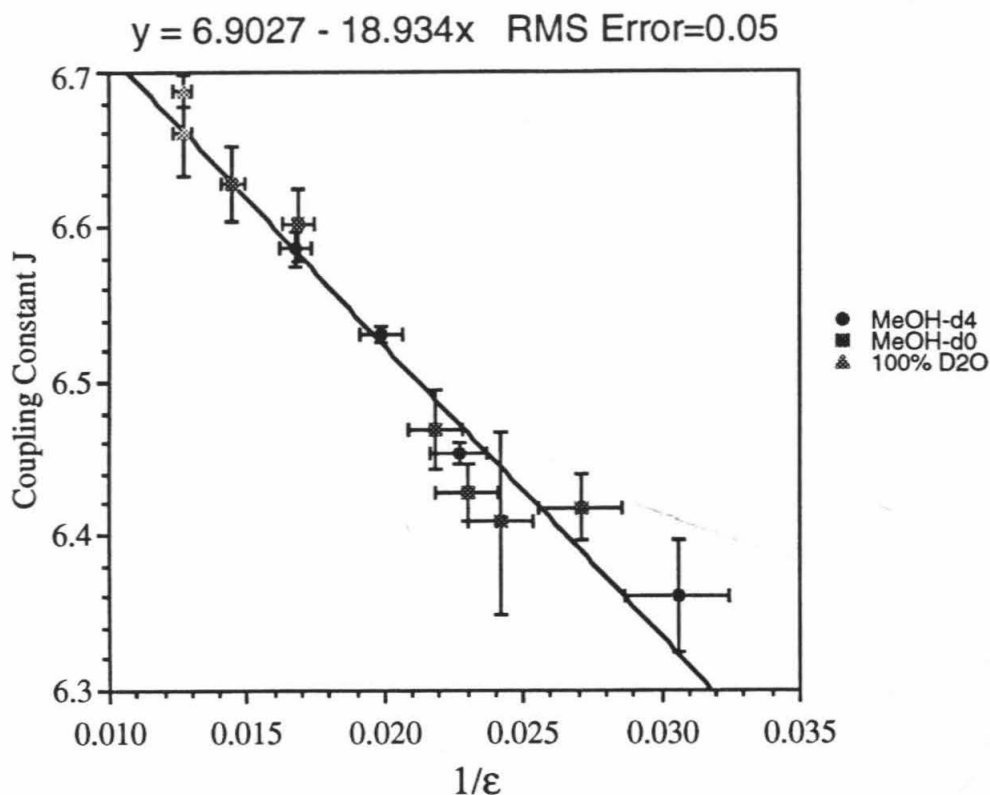


Figure 6. β -alanine dissolved in MeOH/D₂O solvent systems

Table 1. Calculated Coupling Constants for Rotational Conformations of β -Alanine.

All values are in Hertz. J_{xy} denotes the coupling constant between the hydrogens labeled x and y. (Chemically equivalent hydrogens do not split each others' resonances).

Karplus Model

Coupling	trans	gauche 1	gauche 2
J_{13}	13.00	4.00	4.00
J_{23}	4.00	4.00	13.00
J_{14}	4.00	13.00	4.00
J_{24}	13.00	4.00	4.00

Haasnoot⁴ Model

Coupling	trans	gauche 1	gauche 2
J_{13}	14.23	2.23	2.90
J_{23}	3.30	3.74	14.23
J_{14}	3.30	14.23	3.74
J_{24}	14.23	2.90	2.23

Altona³ Model

Coupling	trans	gauche 1	gauche 2
J_{13}	13.21	3.41	2.50
J_{23}	3.38	2.53	12.21
J_{14}	3.38	12.21	2.53
J_{24}	13.21	2.50	3.41

Table 2, Data for Figure 5

EtOD [†]	D ₂ O [†]	ε	mean (J)	sd (J)
0.0%	100.0%	79.1±1.1	6.686	0.005
0.0%	100.0%	80.2±1.1	6.684	0.008
3.3%	96.7%	74.4±1.1	6.672	0.016
3.3%	96.7%	75.5±1.1	6.652	0.008
7.2%	92.8%	71.0±1.1	6.649	0.016
7.2%	92.8%	69.9±1.1	6.643	0.009
11.7%	88.3%	65.1±1.0	6.610	0.015
11.7%	88.3%	66.2±1.1	6.633	0.015
11.7%	88.3%	66.2±1.1	6.626	0.014
16.5%	83.5%	60.8±1.0	6.614	0.018
16.5%	83.5%	59.7±1.0	6.615	0.014
22.2%	77.8%	53.8±0.9	6.588	0.015
22.2%	77.8%	54.8±1.0	6.578	0.015
29.9%	70.1%	48.8±0.9	6.558	0.022
29.9%	70.1%	47.9±0.8	6.556	0.019
39.6%	60.4%	41.7±0.7	6.513	0.020
39.6%	60.4%	42.5±0.8	6.523	0.016
52.2%	47.8%	36.2±0.7	6.440	0.030
52.2%	47.8%	36.9±0.7	6.457	0.047

Table 3, Data for Figure 6

MeOD [†]	D ₂ O [†]	ε	mean (J)	sd (J)
0.0%	100.0%	79±2	6.688	0.010
0.0%	100.0%	79±2	6.660	0.028
10.1%	89.9%	69±2	6.628	0.024
23.1%	76.9%	60±2	6.601	0.023
23.0%*	77.0%	59±2	6.586	0.011
40.2%*	59.8%	50±2	6.531	0.006
51.3%	48.8%	46±2	6.469	0.026
56.0%*	44.0%	44±2	6.454	0.007
57.5%	42.5%	44±2	6.428	0.019
64.3%	35.7%	41±2	6.408	0.060
80.2%	19.8%	37±2	6.418	0.021
100.0%*	0.0%	33±2	6.360	0.036

* MeOH-d₄ was used instead of MeOH-d₀.

† Concentration percentages are in molar fraction form.

Acknowledgments

We would like to thank the following for their assistance with this project: Caltech's SURF Program, Steve Goldberg, Linda Hanely, Sindy Wei, Travis Williams, and Ken Brameld. The Dreyfus Foundation generously provided the Caltech SURF program financial support for this project.

Bibliography

- Abraham, R. J.; Hudson, B. D.; Thomas, W. A. *J. Chem. Soc. Perkin Trans II*, **1986**, p. 1635-1640
 Altona, C.; Francke, R.; de Haan, R.; Ippel, J. H.; Daalmans, G. J.; Hoekzema, A. J. A. W.; van Wijk, J. *Mag. Res. Chem.*, **32**, **1994**, p. 670-678.
 Brameld, K. A. and Goddard, W. A., unpublished work.
 Haasnoot, C. A. G.; de Leeuw, F. A. A. M.; Altona, C. *Tetrahedron*, **26**, **1980**, p. 2783.
 Wei, S. H. SURF Report 1995
 Wyman, J. Jr. *J. Am. Chem. Soc.*, **53**, **1931**, p. 3292

Mutagenesis of the Binuclear Site of the Cu_A Protein

Sudipta Bardhan and John H. Richards

All available structural and electron transfer data suggest that the Cu_A site acts as the initial electron transfer acceptor in the cytochrome *c* oxidases. Thus, the unique delocalization and low reorganization energy of the Cu_A site are likely to be important to this function. Cu_A is known to be a binuclear copper site with the property of a delocalized mixed-valence Cu(1.5)Cu(1.5) structure (1,2,3). The binuclear Cu_A site has a lower reorganization energy than mononuclear copper sites, leaving cytochrome *c* oxidase with more free energy available for proton pumping. Through site-directed mutagenesis, Methionine 227 (M227) has been replaced with an isoleucine (M227I) and a leucine residue (M227L) in the soluble fragment from *Thermus thermophilus*. These mutations were introduced in the hopes of converting the delocalized mixed-valence Cu_A system into a localized Cu(I)Cu(II) site in each mutant.

Key Words: Cu_A—valence trapping—reorganization energy—cytochrome *c* oxidase

Introduction

Many organisms rely on the oxidation of glucose to provide energy for essential biological functions. Glycolysis, fatty acid oxidation, and the citric acid cycle produce NADH and FADH₂ molecules, each of which donates electrons to dioxygen liberating a large amount of free energy that can be used to generate ATP. The process in which electrons are transferred from NADH or FADH₂ to O₂ to form ATP is called oxidative phosphorylation (4). The electrons generated in glucose oxidation flow through a chain of intermediate transmembrane complexes rather than being transferred directly to dioxygen. In the final step of aerobic respiration, cytochrome *c* oxidase catalyzes the four electron reduction of O₂ to H₂O as well as the oxidation of four ferrocytochrome *c* molecules (5).

Electron transfer through the respiratory chain and ATP synthesis are linked by a proton gradient across the inner mitochondrial membrane. The electrons used in dioxygen reduction enter the cytochrome *c* oxidases via four successive bimolecular electron transfers from ferrocytochrome *c*. Reduction of O₂ is coupled to the pumping of two protons from the eukaryotic mitochondrial matrix to the inner mitochondrial space. Two components contribute to the generation of a pH gradient across the inner membrane — the reduction reaction, which takes up two protons from the mitochondrial matrix, and the pumping of two additional protons. The proton gradient is used as an energy source by ATP synthase to produce 36 ATP molecules per glucose molecule (5).

Cytochrome *c* oxidase is known to contain two heme centers, cytochromes *a* and *a*₃, as well as two copper centers, Cu_A, which contains two copper atoms, and Cu_B, which contains one copper atom. The Cu_B site and cytochrome *a*₃ together form an active site in which the dioxygen molecule is bound and reduced; cytochrome *a* and the Cu_A site are involved in electron transfer. In the current model on electron transfer pathways in cytochrome *c* oxidase, the Cu_A site acts as the initial acceptor of electrons donated from cytochrome *c* (5).

The Cu_A site is known to be a binuclear copper site (1,2,3) with the unique property of a delocalized mixed-valence Cu(1.5)Cu(1.5) structure (6). The reorganization energy of the binuclear Cu_A site is thought to be lower than that of the mononuclear blue copper proteins. This feature makes more free energy available to cytochrome *c* oxidase that can be used for proton pumping (7). The Cu_A site has two bridging cysteine ligands (Cys216 and Cys220) and a histidine ligand (His181 and His 224) to each copper. In addition, a methionine sulfur (Met227) is weakly bound to one copper atom and a main chain carbonyl from a glutamic acid residue (Glu218) is weakly bound to the other copper (8). Two site-directed mutants of the soluble fragment from *Thermus thermophilus* were constructed in which Met227 was replaced by isoleucine or leucine.

The isoleucine mutant (M227I) and the leucine mutant (M227L) should increase the reorganization energy of the protein because these mutations should create a valence-trapped site. Normally, one electron is shared equally between the two coppers in the binuclear site, but the introduction of these mutations should convert the delocalized center into a localized Cu(I)Cu(II) system — a Class III complex to a Class I complex according to the classification scheme of Robin and Day (5). This result has been shown in *Paracoccus denitrificans* cytochrome *c* oxidase by Zickermann and coworkers, where valence trapping has been observed in the M227I mutation.

Materials And Methods

Construction of pETCu_AM227I and pETCu_AM227L. Since Met227 lies near the end of the Cu_A gene, a one step PCR method was used in which the sense oligonucleotide primer (CuA.s.NdeI: 5' CTT TAA GAA GGA GAT ATA CAT|ATG GCC TAC A 3') coded for an NdeI restriction site (underlined), whereas the antisense oligonucleotide primer encoded for the M227I (Cu_AL.as.BamHI: 5' TTA GCA GGA TC|C TCA CTC CTT CAC CAC GAT CGT GCC GAA GAT GTT C 3') or M227L (Cu_AL.as.BamHI: 5' TTA GCA GGA TC|C TCA CTC CTT CAC CAC GAT CGT GCC GAA CAG GTT C 3') mutation and a BamHI site (underlined).

The M227I and M227L PCR fragments were extracted once with one volume of chloroform to remove any traces of oil, and then washed twice with 2 mL of 3 M sodium acetate, pH 5.3, in a Centricon 100 to remove *Taq* polymerase, nucleotides, and PCR buffer. Afterwards, the fragments were washed an additional two times with doubly distilled H₂O. The PCR fragments and pETbla vector were digested with NdeI and BamHI restriction enzymes and then purified on a low melting temperature agarose gel. The digested fragments and vector were then cut from the gel, melted at 70°C, equilibrated at 45°C, and the agarose was digested with Gelase. The vectors pETCu_AM227I and pETCu_AM227L were formed by ligating the appropriate PCR fragment into the vector. The constructs were sequenced to confirm that the desired mutations were introduced.

Protein Expression and Purification. A 10 mL culture of LB media (50 mg/mL kanamycin) was inoculated from a freshly streaked plate of BL21 (DE3) cells containing either the pETCu_AM227I or pETCu_AM227L plasmid. This culture was incubated for 12 hours at 37°C, and then was used to inoculate a 1 L flask of LB and kanamycin. This culture was incubated at 37°C, typically for about 2 hours, until the absorbance at 600 nm reached 0.4 to 0.6, and then induced for 12 hours using a final concentration of 0.4 mM IPTG. The cells were pelleted by centrifugation at 5,000 x g for 10 minutes. The pellet from 1 L of culture was resuspended in 25 mL of 50 mM Tris-HCl, pH 8.0, 4 mg/mL lysozyme, 40 U/mL DNase I, 3 U/mL RNaseA, 0.1% Triton X-100, and then was sonicated. The cell debris was separated from the extract by centrifugation at 12,000 x g for 30 minutes at 4°C. The addition of 15 µL/mL volume of 100 mM Cu(His)₂ caused the solution to turn purple by forming the Cu_A site. An additional 30 minute centrifugation step at 12,000 x g further clarified the protein solution. The pH of the protein solution was adjusted to pH 7.0 using 1 M KH₂PO₄ and potassium chloride was added to a final concentration of 300 mM KCl. The protein solution was then loaded on a metal affinity column loaded with copper that had been equilibrated with 100 mM potassium phosphate buffer and 500 mM KCl, pH 7.0, at 4°C, washed with several volumes of equilibration buffer, and eluted with 1 M imidazole.

UV/Vis. Optical spectra of the mutants were recorded on a Hewlett Packard 8453A Diode Array Spectrophotometer.

Results

Protein Expression and Purification. Upon induction with IPTG, the cells produce only the apo form of the protein. After cell lysis, the addition of Cu(II) in the form of Cu(His)₂ causes the solution to turn purple. In the case of the M227L protein, the purple color is very quickly lost, suggesting that the site is losing copper, and the solution returns to an intense blue color, similar to the color of Cu(His)₂. The M227I protein is slightly more stable than the leucine mutant, and can be bound to a metal affinity column and purified before the sample denatures.

Although both the M227I and M227L proteins could be expressed, purification of the holo proteins was nearly impossible because of the proteins' instability. A number of different methods were utilized in an attempt to purify the mutant proteins. At first, we attempted to lower the pH of the cell lysate to pH 4.6 in order to remove more impurities and to load the protein solution on a CM Sepharose column equilibrated with 50 mM sodium acetate, pH 4.6, at 4°C. The protein was washed with several volumes of equilibration buffer and eluted with a 0 - 1 M NaCl gradient in 50 mM sodium acetate. The eluate was in many cases faintly purple in color, but soon turned colorless even when frozen immediately. Next, a metal affinity column was used to purify the proteins, as described earlier. It was possible to elute to M227I mutant holo protein from the metal affinity column, but the protein

quickly denatured afterwards, i.e. lost copper. The M227L mutant is very unstable and purification has been impossible to date. Future attempts to purify the M227I and M227L proteins will involve methods in which the apo protein is purified on a hydrophobic affinity phenyl HR sepharose column.

Protein Analysis. SDS-PAGE analysis shows that the M227I and M227L mutants both have apparent $M_r \sim 15,000$, consistent with wild type Cu_A .

UV/Vis. The absorbance spectrum of M227I, taken directly after elution, is very different from that of wild type Cu_A . The doublet at 480 nm and 530 nm seen in wild type is missing in the M227I spectrum, and the band centered at 790 nm seen in wild type seems to be shifted in M227I.

Discussion And Conclusions

Recent X-ray structure data from *P. denitrificans* cytochrome aa_3 (3), bovine cytochrome aa_3 (2), and the engineered purple center in the CyoA fragment (1) show that Cu_A is a binuclear copper site with two bridging cysteine thiolate ligands and with one strong coordinate bond from each copper to an imidazole ring of histidine. Each copper also has a weaker coordinate bond to either the carbonyl oxygen of a glutamic acid or to the sulfur of a conserved methionine. The Cu_A site behaves as a spin-delocalized, mixed-valence structure in which the single unpaired electron is found with equal probability at either copper (7). It is thought that the introduction of the M227I and M227L mutations into the *T. thermophilus* fragment creates a valence trapped Cu_A site, although without EPR data, it is impossible to verify this belief.

Sequence analysis, mutagenesis, and protein engineering studies indicate a possible evolutionary relationship between soluble blue copper proteins and the Cu_A protein. This leads to the question: why did a binuclear purple site, rather than a mononuclear blue site, evolve into the primary electron acceptor in cytochrome *c* oxidases? Preliminary electrochemical characterization suggests that Cu_A may have a significantly lower reorganization energy than that of mononuclear copper sites. The rate of electron transfer between two redox centers within a protein-protein complex is determined by the driving force of the reaction, ΔG° , the reorganization energy, and the electronic coupling between the donor and the acceptor. The driving force for electron transfer from cytochrome *c* to Cu_A is close to zero, and because of this low ΔG° and the large distance between the two, an appreciable electron transfer rate can only be achieved if the reorganization energy of the Cu_A site is quite small. A low reorganization energy may allow more free energy to be available for cytochrome *c* oxidase to use for proton pumping across the inner mitochondrial membrane (7).

Acknowledgements

I thank John Richards and Claire Slutter for all their help with this project. This work was supported by the SURF program and Mr. and Mrs. Robert L. Noland.

References

1. Wilmanns, M., Lappalainen, P., Kelly, M., Sauer-Eriksson, E. and Saraste, M. (1995) *Proc. Nat'l. Acad. Sci. USA* 92, 11955-11959.
2. Tsukihara, T., Aoyama, H., Yamashita, E., Tomizaki, T., Yamaguchi, H., Shinzawaitoh, K., Nakashima, R., Yaono, R. and Yoshikawa, S. (1995) *Science* 269, 1069-1074.
3. Iwata, S., Ostermeier, C., Ludwig, B. and Michel, H. (1995) *Nature* 376, 660-669.
4. Stryer, L., *Biochemistry*. 1995 W.H. Freeman and Company.
5. Slutter, C., PhD Thesis California Institute of Technology 1996.
6. Antholine, W.E., Kastrau, D.H.W., Steffans, G.C.M., Buse, G., Zumft, W.G. and Kroneck, P.H.M. (1992) *Eur. J. Biochem.* 209, 875-888
7. Slutter, C., Sanders, D., Wittung, P., Malmstrom, B.G., Aasa, R., Richards, J.H. and Fee, J.A. (1996) In Press
8. Zickermann, V., Verkhovsky, M., Morgan, J., Wikstrom, M., Anemuller, S., Bill, E., Steffans, G.C.M. and Ludwig, B. (1995) *Eur. J. Biochem.* 234, 686-693.

Engineered Protein-Membrane Interactions

Mat E. Barnett and Frances H. Arnold

The fabrication of robust, synthetic lipid surfaces to promote specific protein binding and self-assembly presents the possibility to create biological sensing devices, drug delivery systems, nanomaterials, and to understand fundamental biomembrane functions. Functional, metal-chelating, iminodiacetate (IDA) lipid monolayers at the air-water interface were used to promote protein binding via Cu(II)-IDA-histidine complex formation. Metal-bound IDA lipids specifically target protein histidine residues. To facilitate this targeting, hexahistidine tags were attached to a model protein, dihydrofolate reductase (DHFR-his6). Results concerning Cu(II)-IDA lipid monolayer interactions with DHFR-his6, using monolayer film balance techniques, are presented. These results show that a binding interaction between DHFR-his6 and the IDA monolayer depends on the presence of copper. Further results give an estimate for the strength of this interaction. These results are consistent with a proposed protein targeting mechanism, whereby the hexahistidine tags on DHFR's surface specifically interact with Cu(II)-bound IDA lipids. Cu(II)-IDA-histidine ternary complex formation can be used for applications requiring specific protein-lipid interactions.

Introduction

Molecular recognition and binding events between proteins and lipid membrane surfaces underlie many biological signaling pathways [1, 2]. Lipid molecules possessing protein receptors respond to the protein ligands that they specifically bind [3]. Synthetic lipidbased interfaces have been designed in an attempt to mimic nature's ability to target proteins [4], signal ligand assembly [5, 6], and effect two-dimensional protein crystallization [7-9]. Synthetic assemblies of proteins and lipids also form the basis of novel sensing and electronic device fabrication [10].

- Protein targeting to lipid surfaces via non-specific electrostatic interactions [11], or specific protein receptors [12] are two methods of two-dimensional protein immobilization (Figure 1). Problems persist with both approaches. With nonspecific electrostatic interactions, proteins often do not adopt any particular orientation at the lipid surface. This can be undesirable for nanomaterial applications, in which an ordered array of molecules is often crucial for functional properties [13]. Further, electrostatic interactions between proteins and lipid surfaces are typically weak. The specific lipid receptor approach can overcome these two drawbacks; a specific receptor can confer orientational control and strong binding to the lipid-protein interaction. However, this very specificity can be a drawback, in that a given lipid receptor will usually only dock to one type or class of protein. Thus for each new type or class of protein, a new type of receptor lipid must be designed and synthesized. Furthermore, the type of lipid functionality that will act as a receptor for a given type or class of protein can be difficult to know *a priori*. Considering these drawbacks, a general protein-targeting mechanism is desired.
- Metal-chelating iminodiacetate (IDA) lipid molecules that promote protein binding via Cu(II)-IDA-histidine complex formation (Figure 2) have been synthesized for this purpose [14]. IDA lipids chelate Cu(II) ions, which in turn can coordinate one or more protein surface histidine residues ($K_a \sim 10^{3.5} \text{ M}^{-1}$ for one histidine). Histidine residues are naturally present on the surfaces of many proteins, and if not present can be genetically incorporated through the use of hexahistidine (his6) fusion peptides [15, 16] or other histidine motifs (e.g., His-X3-His [17]). Additionally, at pH 7-7.5, histidine is the only amino acid residue that Cu(II) can specifically coordinate. Formation of the ternary complex is fully reversible upon addition of acid (protonation of histidine residues) or EDTA (competitive chelation of Cu(II)).
- We present here dihydrofolate reductase-his6 (DHFR-his6) interactions with Langmuir monolayers [18] of Cu(II)-IDA lipid. A monomolecular lipid film is self-assembled at the air-aqueous interface, and histidine-tagged proteins are introduced into the aqueous phase beneath the monolayer. As the protein diffuses throughout the subphase and comes to the lipid surface, protein interactions with the lipid monolayer that perturb membrane packing are recorded as changes in monolayer surface pressure (at constant surface area) or as changes in surface area (at constant surface pressure). Results show that an interaction between IDA-lipid monolayers and DHFR-his6 depends on the presence of copper. This is consistent with a proposed mechanism of Cu(II)-IDA-histidine binding, in which the IDA lipid chelates a Cu(II) ion, which then coordinates the protein his6-tag.

Materials and Methods

Materials

1-stearyl-2-(9-pyrenylnonyl)-rac-glycero-3-(8-(3,6-dioxy)octyl-1-amino-N,N-diacetic acid) (PSIDA, Figure 3) and 1,2-dioleoyl-rac-glycero-3-(8-(3,6-dioxy)octyl-1-amino-N,N-diacetic acid) (DOIDA, Figure 3), the lipids used to target DHFR-his6, were synthesized as described previously [14]. L-alpha-l-stearoyl-2-oleoyl-sn-glycero-3-phosphocholine (SOPC, Figure 3) was purchased from Avanti Polar Lipids (Alabaster, AL) and used as received. Equimolar binary mixtures of IDA:SOPC were prepared by mixing appropriate volumes of chloroform-dissolved stock IDA and SOPC lipids. IDA lipids were premetallated by adding an aliquot of concentrated methanol-dissolved CuCl_2 to the chloroform-dissolved lipid solutions.

- DHFR modified with a poly(histidine) fusion peptide was expressed and purified by K. Maloney using a *QIAexpression* system (Qiagen, Inc.). The concentration of the protein was determined using a colorimetric assay (Bio-Rad) with BSA as a standard.
- -[N-morpholino]propanesulfonic acid (MOPS) (99.5%), NaCl (99%), chloroform and methanol (HPLC grade) were purchased from Sigma (St. Louis, MO).
- All glassware was cleaned in a concentrated H_2SO_4 / NoChromix™ (CMS) solution. Water used for buffer solutions had a resistivity of 18 megaohms cm^{-1} (Nanopure, Millipore, Inc.). Lipid and protein solutions were stored at -20°C .

Methods

Monolayer experiments were carried out on a computer-controlled, teflon Langmuir film balance (LB-1000, KSV Instruments, Helsinki, Finland) of surface area $75 \times 230 \text{ mm}^2$ (Figure 4). Lipid mixtures were spread at the air-buffer interface, and a waiting period ensued to allow for chloroform evaporation. Protein binding experiments were carried out with 20 mM MOPS, 250 mM NaCl, pH 7.8 buffered subphases at room temperature, and monolayers were compressed at a constant rate of $1.9 \text{ \AA}^2 \text{ molecule}^{-1} \text{ min}^{-1}$. When the desired surface pressure (π) was reached, π was held constant and the monolayer was allowed to equilibrate for 20-30 minutes. Protein was injected into the subphase from behind the trough barrier and allowed to diffuse throughout the subphase. Following protein injections, changes in surface area at constant π were recorded as a function of time.

- In control experiments with non-metallated PSIDA, the monolayer was compressed to 31 mN m^{-1} , allowed to equilibrate, then allowed to expand in 2 mN m^{-1} decrements. This was continued until a surface pressure of 17 mN m^{-1} was attained. This experiment was done to determine the system's "cutoff" pressure: the lowest surface pressure at which nonspecific protein penetration into the monolayer is excluded.
- DOIDA monolayer experiments were performed using an argon atmosphere and a hydrophobized pyrex petri dish (35 mm diameter) instead of a teflon trough. After being spread, the monolayer was allowed to equilibrate for 35-40 minutes, then the desired amount of protein was injected into the subphase through the monolayer, and changes in surface pressure at constant surface area were recorded as a function of time.

Results

We set out to demonstrate that Cu(II)-IDA lipid monolayers can target a model protein, DHFR-his6. In particular, we wanted to show that targeting depends critically on the presence of Cu(II), and that protein binding can be associated with changes in π . Shown in figure 5 is a Cu(II)-free binding control experiment performed on PSIDA. At high surface pressures ($\pi > 25 \text{ mN m}^{-1}$) no change in surface area is observed. This indicates that nonspecific protein insertion into the monolayer is excluded at these pressures. Only when π is less than the cutoff pressure of 25 mN m^{-1} can the protein insert into the monolayer and thus cause a change in surface area at constant π .

- A nonspecific-insertion-preventing surface pressure of 25 mN m^{-1} was chosen for the experiment in which the PSIDA lipid monolayer was loaded with Cu(II) (Figure 6). Shortly after protein injection, a large increase in surface area is observed. This effect is absent without Cu(II), and thus the interaction between the IDA lipid and DHFR-his6 above 25 mN m^{-1} depends specifically on Cu(II).
- The Cu(II)-DOIDA experiments were performed in order to estimate the strength of the Cu(II)-IDA-histidine interaction. In a series of experiments using different DHFR-his6 subphase concentrations, the $\Delta\pi$ effected by the protein at constant surface area is seen to increase linearly with protein concentration, up to a concentration of 25 nM (Figure 7). At subphase concentrations greater than this, essentially the same $\Delta\pi$ is observed, up to a DHFR-his6 concentration of 170 nM. Such saturation behavior is characteristic of specific binding. Additionally, the estimated dissociation constant (K_d) is comparable to that of cytochrome b5-his6 with Cu(II)-IDA monolayers, previously estimated by this group to be $\sim 50 \text{ nM}$ [14].

Discussion

Cytochrome b5-his6 has previously been shown by this lab to induce an area change in Cu(II)-IDA lipid monolayers [14]. Tampe and co-workers have also targeted hexahistidine-tagged proteins to metal-chelating synthetic lipid monolayers [19]. Such monolayer-protein systems combine the specificity and strength of a metal-coordination interaction with the generality of a hexahistidine fusion peptide that can be genetically incorporated into virtually any protein. These systems show promise for nanomaterial applications, in which the specific lipid-protein interaction would confer orientational control while the generality of the system might allow for diverse two-dimensional protein-based structures.

- In the PSIDA-DHFR-his6 system, we observed that changes in monolayer area ($\Delta A/A$) at constant π depend on the presence of Cu(II). This dependence is consistent with our proposed mechanism for Cu(II)-IDA-ligand binding. In this mechanism the IDA lipid chelates Cu(II), which in turn coordinates the his6 tail engineered on DHFR's N-terminus (Figure 2). The $\Delta A/A$ arises as the increasing amount of bound protein forces the lipid monolayer to expand at constant pressure [14]. The $\Delta A/A$ observed without Cu(II) at surface pressures less than 25 mN m^{-1} (Figure 5) is believed to be due to a nonspecific protein-lipid interaction, most likely penetration of the lipid monolayer by the protein. Below a characteristic surface pressure, proteins commonly penetrate and induce area changes in lipid monolayers [20]. This penetration is precluded at higher values of π . A surface pressure of 25 mN m^{-1} was thus chosen for the experiments in which Cu(II) was present (Figure 6), so that the effects of the specific interaction involving Cu(II) could be isolated from those of the nonspecific penetration. In the Cu(II)-free control experiment, 20 mM Ca(II) was included in the buffered subphase so as to retain monolayer charge neutrality while preventing metal-histidine coordination interactions.
- The Cu(II)-DOIDA experiments performed in the hydrophobized petri dish show saturation behavior of the DHFR-his6 (Figure 7). This has been observed previously in the case of cytochrome b5-his6 [14]. In the case of DHFR-his6, all protein subphase concentrations greater than or equal to 25 nM cause essentially the same change in surface pressure at constant area. This implies that all of the protein-accessible Cu(II)-IDA sites in the monolayer become occupied by DHFR-his6, preventing additional protein binding to the DOIDA via Cu(II). At protein concentrations less than 25 nM, some Cu(II)-IDA monolayer binding sites are still unoccupied, and thus the maximal $\Delta\pi$ is not attained at these protein concentrations. From these data, we estimate the dissociation constant (K_d) of the Cu(II)-IDA-DHFR-his6 ternary complex to be $\sim 25 \text{ nM}$. This is comparable to the K_d value previously estimated for the Cu(II)-IDA-cytochrome b5-his6 ternary complex ($\sim 50 \text{ nM}$) [14].

Conclusions

In this study we have shown that DHFR-his6 is targeted to Cu(II)-IDA lipid monolayers spread at the air-aqueous interface. A dissociation constant for this complex was estimated to be 25 nM. These results can be useful for determining conditions of DHFR-his6 two-dimensional crystallization.

Future Work

Another control experiment, to show that the specific lipid-protein interaction depends on the presence of histidine residues, would be desirable. In this experiment wild-type DHFR, without the hexahistidine fusion peptide, would be injected into the subphase beneath a Cu(II)-loaded IDA monolayer. A lack of change in surface area at a surface pressure of 25 mN m^{-1} would show that the lipid-protein interaction is histidine-dependent.

Figure 1

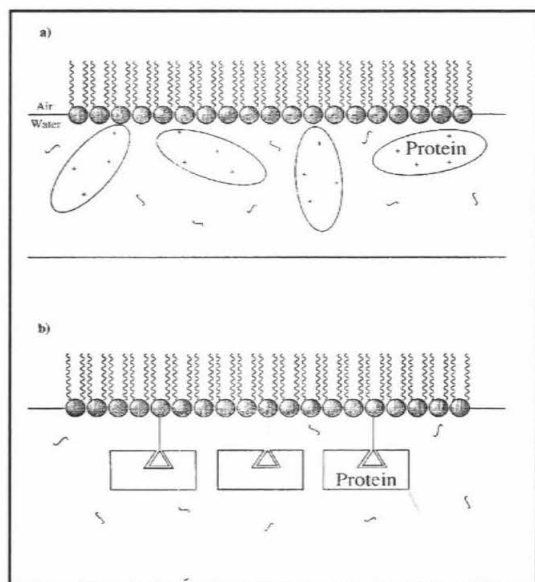


Figure 1. a) Nonspecific electrostatic, and b) specific receptor lipid-protein interactions

Figure 2

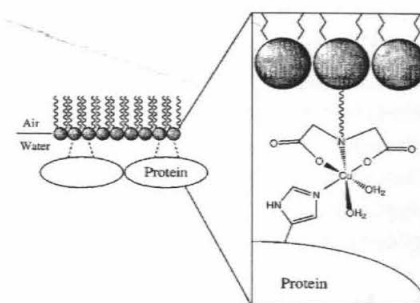


Figure 2. IDA lipid-Cu(II)-histidine ternary complex ($K_a \sim 10^{3.5} \text{ M}^{-1}$)

Figure 3

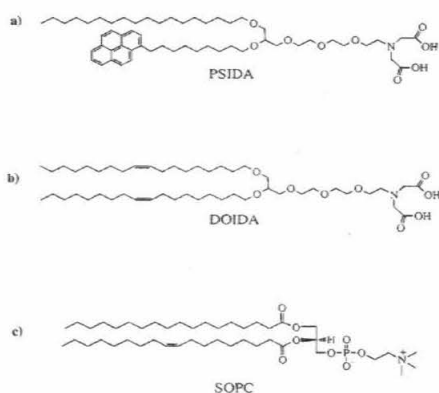


Figure 3. Lipid chemical structures: a) 1-stearyl,2-(9-pyrenyl)rac-glycero-3-(8-3,6-dioxyl)octyl-1-amino-N,N-diacetic acid (PSIDA). b) 1,2-dioleoyl-racglycero-3-(8-3,6-dioxyl)octyl-1-amino-N,N-diacetic acid (DOIDA). c) 1-stearoyl,2-oleoyl-sn-glycero-3-phosphocholine (SOPC)

Figure 4

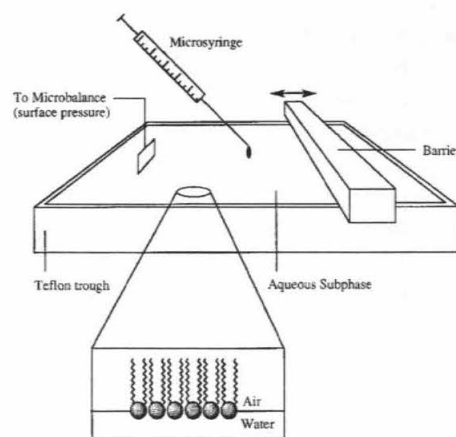


Figure 4. Film balance experimental setup

Figure 5

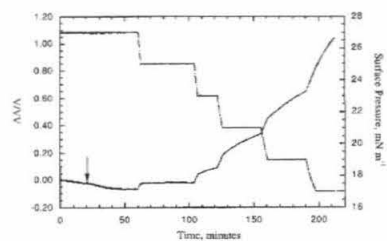


Figure 5. Cu(II)-free control experiment with PSIDA. Subphase is 20 mM CaCl₂, 20 mM MOPS, 250 mM NaCl, pH 7.8, room temperature. DHFR-his6 concentration ~ 60 nM. Compression rate: 1.9 Å² molecule⁻¹ minute⁻¹. Arrow indicates time of protein injection

Figure 6

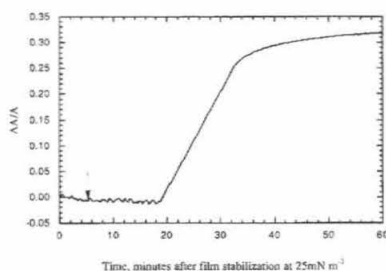


Figure 6. Cu(II)-PSIDA experiment. Same conditions as in Figure 5, except no CaCl₂ in subphase. Arrow indicates time of protein injection

Figure 7

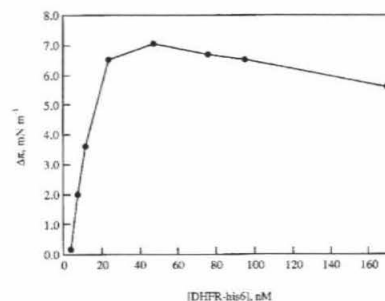


Figure 7. Variable DHFR-his6 concentration DOIDA experiments. Subphase is same as in Figure 6. Initial surface pressure (before protein injection): ~25 mN m⁻¹. DHFR-his6 concentration varied from ~4 nM to 170 nM

Acknowledgements

This research was supported by the Caltech SURF Program. The author thanks professor F. H. Arnold for general advice, and Dr. K. M. Maloney for technical advice and assistance in preparing the manuscript.

References

- DeLisi, C., Siraganian, R. P. (1979). Receptor Cross-Linking and Histamine Release: I. The Quantitative Dependence of Basophil Degranulation on the Number of Receptor Doublets. *J. Immunol.* **122**, 2286-2292.
- Shimohigashi, Y., Costa, T., Chen, H.-C., Rodbard, D. (1982). Dimeric Tetrapeptide Enkephelins Display Extraordinary Selectivity for Delta-Opiate Receptors. *Nature* **297**, 333-335.
- Ullrich, A. S., J. (1990). Signal Transduction by Receptors with Tyrosine Kinase-Activity. *Cell* **61**, 203-212.
- Samuelson, L. A., Miller, P., Galotti, D. M., Marx, K. A., Kumar, J., Tripathy, S. K., Kaplan, D.L. (1992). The Monomolecular Organization of a Photodynamic Protein System through Specific Surface Recognition of Streptavidin by Biotinylated Langmuir-Blodgett-Films. *Langmuir* **8**, 604-608.
- Stelzle, M., Weissmuller, G., Sackman, E. (1993). On the Application of Supported Bilayers as Receptive Layers for Biosensors with Electrical Detection. *J. Phys. Chem.* **97**, 2974-2981.
- Charych, D. H., Nagy, J. O., Spevak, W., Bednarski, M. D. (1993). Direct Colorimetric Detection of a Receptor-Ligand Interaction by a Polymerized Bilayer Assembly. *Science* **261**, 585-588.
- Hemming, S. A., Bochkarev, A., Darst, S. A., Kornberg, R. D., Ala, P., Yang, D. S. C., Edwards, A.M. (1995). The Mechanism of Protein Crystal-Growth from Lipid Layers. *J. Mol. Biol.* **246**, 308-316.
- Edwards, A. M., Darst, S. A., Feaver, W. J., Thompson, N. E., Burgess, R. R., Kornberg, R. D. (1990). Purification and Lipid-Layer Crystallization of Yeast RNA Polymerase-II. *Proc. Natl. Aca. Sci.* **87**, 2122-2126.
- Frey, W., Schief, W. R., Pack, D. W., Chen, C. T., Chilkoti, A., Stayton, P., Vogel, V., Arnold, F. H. (1996). 2-Dimensional Protein Crystallization via Metal-Ion Coordination by Naturally-Occuring Surface Histidines. *Proc. Natl. Aca. Sci.* **93**, 4937-4941.
- Sasabe, H., Furuno, T., Otomo, J., Sato, A., Nagamune, T. (1991). Control of 2-Dimensional Array of Protein Molecules for Bioelectronics. *New Journal of Chemistry* **15**, 149-152.
- Ohnishi, S., Hara, M., Furuno, T., Sasabe, H. (1992). Imaging the Ordered Arrays of Water-Soluble Protein Ferritin with the Atomic Force Microscope. *Biophys. J.* **63**, 1425-1431.
- Ahlers, M., Hoffmann, M., Ringsdorf, H., Rourke, A. M., Rump, E. (1991). Specific Interaction of Desthiobiotin Lipids and Water-Soluble Biotin Compounds with Streptavidin. *Makromolekulare Chemie Macromolecular Symposia* **46**, 307-311.
- Firestone, M. A., Shank, M. L., Sligar, S. G., Bohn, P. W. (1996). Film Architecture in Biomolecular Assemblies. Effect of Linker on the Orientation of Genetically Engineered Surface-Bound Proteins. *J. Am. Chem. Soc.* **118**, 9033-9041.
- Ng, K., Pack, D. W., Sasaki, D. Y., Arnold, F. H. (1995). Engineering Protein-Lipid Interactions: Targeting of Histidine-Tagged Proteins to Metal-Chelating Lipid Monolayers. *Langmuir* **11**, 4048-4055.

15. Fancy, D. A., Melcher, K., Johnston, S. A., Kodadek, T. (1996). New chemistry for the study of multiprotein complexes: the six-histidine tag as a receptor for a protein crosslinking reagent. *Chem. & Biol.* **3**, 551-559.
16. Kubalek, E. W., Legrice, S. F. J., Brown, P. O. (1994). 2-Dimensional Crystallization of Histidine-Tagged HIV-1 Reverse-Transcriptase Promoted by a Novel Nickel-Chelating Lipid. *J. Struct. Biol.* **113**, 117-123.
17. Arnold, F. H. (1991). Metal-Affinity Separations-A New Dimension in Protein Processing. *Bio/Technology* **9**, 151-156.
18. Gaines, G. L. (1966). *Insoluble Monolayers at Liquid-Gas Interfaces*. New York: John Wiley & Sons.
19. Dietrich, C., Schmitt, L., Tarnpe, R. (1995). Molecular-Organization of Histidine-Tagged Biomolecules at Self-Assembled Lipid Interfaces using a Novel Class of Chelator Lipids. *Proc. Natl. Aca. Sci.* **92**, 9014-9018.
20. Peschke, J., Mohwald, H. (1987). Cytochrome-c Interaction with Phospholipid Monolayers and Vesicles. *J. Coll. Surf.* **27**, 305-323.

Directed Evolution of a Thermostable Subtilisin

Noah Malmstadt and Frances H. Arnold

Subtilisin E is produced by the bacteria *Bacillus subtilis*. Like other enzymes produced by organisms in temperate environments, it is a mesophilic enzyme — its activity is greatest at moderate temperatures (e.g. 20-60°C). The goal of this project is to use directed evolution techniques to increase the stability and activity of this enzyme at high temperatures. The subtilisin E gene is mutated randomly through error-prone PCR. The subsequently created mutant library is then screened for residual activity after incubation at an elevated temperature. Highly thermostable mutants are subjected to detailed thermal inactivation analysis and sequenced. The most thermostable variant from each generation is subjected to error-prone PCR again in order to create the next generation of mutants. This process can be repeated for several generations, creating a much more thermostable variant. Research so far has produced a variant that is almost four times more stable than subtilisin E at 65°C.

Introduction

Enzymes, extraordinarily specific and efficient biological catalysts, hold much promise for use in industry. However, since most natural enzymes are very unstable at even moderately high temperatures (> 60°C), they are useless for any application that might require such temperatures. Hence, the thermostabilization of natural enzymes has become a topic of great interest (5). Most attempts to develop thermostable enzymes have utilized rational design methods. Such methods attempt to identify, on the molecular level, the biochemical origin of thermal instability. Once understood, the mechanisms of thermal degradation can be countered, theoretically, by making specific changes in the amino acid sequence of the enzyme.

There are drawbacks to the rational design method. Since neither the mechanisms of protein folding nor those of enzyme action are fully understood, it is impossible at this point to make meaningful changes in protein sequence based on theory alone. In addition, since it takes upwards of a year to produce even a x-ray crystallograph of a protein, the time frame required to identify a new enzyme, study its mechanism of thermal degradation, and develop a rational solution to this thermal degradation is impractically long. There is, however, an alternative to rational design — directed evolution (2).

In a directed evolution experiment, the segment of DNA which codes for the enzyme in question (referred to as the “wild type” enzyme) is subjected to a process which randomly introduces into it mutations. This process produces a large library of genes that all differ slightly from the gene for the wild type. This library is ligated into plasmid vectors, which are inserted into bacteria. These bacteria express the genes, secreting the corresponding enzymes, which are all slightly different from the wild type. These enzymes are then screened in order to determine which are most fit for the desired environment or substrate. The most fit enzymes are then subjected to the process again. This cycle is repeated until an enzyme with significantly greater fitness than the original enzyme is evolved. By altering the screening method, enzymes can be involved for a vast variety of substrates or environments. For instance, to develop an enzyme that acts on a novel substrate, screening would be performed by monitoring the rates at which the various enzymes in the library convert that substrate. In order to screen for an enzyme to be used in an environment with a high concentration of organic solvent, the screening would be performed by monitoring the enzymes' activities in organic solvent.

The goal of the research presented here is to increase the thermostability of subtilisin E, a protease produced by the bacterium *Bacillus subtilis*. Like all proteases, subtilisin E functions in its native environment to degrade unneeded or damaged proteins. Of course, outside of its native environment, subtilisin E can promote the reverse of this reaction — the ligation of amino acids into peptides. Subtilisin E is a mesophilic enzyme, possessing a melting temperature $T_M=58.5^\circ\text{C}$ (3) and an activity half-life of approximately 5.7 minutes at 65°C. Subtilisin E has been studied extensively, and projects to improve its thermostability have produced some stabilizing mutations (4). In addition, subtilisin E thermostability is interesting to study because there exists a natural thermostable subtilisin, thermitase, produced by a thermophilic bacteria (8). A sequence comparison between laboratory-evolved subtilisin E and thermitase should reveal which sequence differences between thermitase and the wild type contribute to increased thermostability and which are neutral to thermostability. This comparison could provide valuable insight into the natural process of evolution by revealing which mutations imparted selective advantage to the thermophilic species and which survived simply because there was

no selective pressure forcing them to be eliminated (neutral mutations). In addition, the mutations introduced in this project will be compared to those introduced in a separate project whose goal is a subtilisin E with increased peptide ligase activity. This comparison will reveal whether thermostability and ligase activity can be introduced simultaneously in the same enzyme.

Experimental Procedures and Materials

A mutant library was created by error-prone polymerase chain reaction (PCR, see reference 6) performed on the subtilisin E gene. The gene was then ligated into a plasmid shuttle vector (figure 1). This plasmid was inserted into *E. coli*. These bacteria were grown in order to amplify the plasmid. The plasmid was then purified from the *E. coli* and inserted into *B. subtilis*. These bacteria were plated on Petri dishes and grown. Colonies growing on the plates were picked into the wells, filled with growth medium, of 96 well plates, which were incubated again. Once the bacteria on these plates had grown, they were centrifuged and small samples of supernate from each well were transferred to the corresponding wells of two clean plates. A kinetic screening assay was performed on each of these plates, one after incubation at elevated temperature and one without incubation. The thermal stability of the enzyme in each well was estimated by comparing the activity before and after incubation. The most stable enzymes were identified, and their genes were purified from the bacteria that produced them. A more detailed thermal inactivation assay was performed on the selected enzymes, and the genes for these enzymes were sequenced. The most stable variant was reserved for further cycles of mutagenesis and screening. The materials and methods used for each step of this procedure are detailed below:

Error-prone PCR: This method is detailed in reference 6.

Bacterial growth: Petri dishes were coated with LB medium with 50 μ g/mL kanamycin and solidified with agar. The dishes were incubated at 37°C for 24-36 hours. Ninety-six well plate wells were filled with SG medium with 50 μ g/mL kanamycin. The plates were incubated at 37°C for 48 hours.

Screening assay: The assay solution was 0.2 mM succinyl alanine-alanine-proline-phenylalanine p-nitroanilide (s-AAPF-na), which is hydrolyzed by proteases to release p-nitroaniline, which absorbs at 410 nm. The solution also contained 0.1M tris-HCl buffer and 10 mM CaCl₂. For the unincubated assay, the empty plate was heated to the incubated assay temperature. Ten μ L enzyme containing supernate was then transferred to each well of this plate from the corresponding well of the centrifuged growth plate. One-hundred μ L assay solution was then added to each well of the assay plate. The activity was measured by monitoring the evolution of p-nitroaniline, using the kinetic assay function of the SoftMax Pro plate reading software on a Molecular Dynamics Thermomax plate reader. For the incubated assay, 10 μ L supernate was transferred from the each well of the growth plate to the corresponding well of an empty plate at room temperature. This plate was then incubated for 30 minutes, 100. μ L assay solution added, and the activity measured; temperature of incubation varied with generation number. For the first generation, incubation was at 60°C. For the second generation, incubation was at 65°C.

Thermal inactivation assay: Bacteria selected from the growth plate were picked into tubes containing 2.5 mL SG medium with kanamycin. These tubes were incubated for 24 hours at 37°C, with constant agitation. After incubation, the solution, containing enzyme, was centrifuged. A cuvette containing 980 μ L assay solution and 20 μ L enzyme solution was then placed in a spectrophotometer, and the absorption at 410 nm was measured. A small tube containing the enzyme solution was then incubated at 65°C. Further spectrophotometric measurements were taken, using the enzyme in this tube, every five minutes for 45 minutes. These measurements were fitted to an exponential curve in order to determine the rate of thermal inactivation. Activity half-life (AHL) was determined from this rate based on the formula:

Results and Discussion

Two generations of mutagenesis have been completed. The results from the first generation have been thoroughly analyzed; analysis is ongoing with the second generation. The first generation produced three promising variants. These variants have been designated 2A12, 4E11, and 1E8. Their respective activity half-lives are 15.7 minutes, 20.0 minutes, and 15.0 minutes (cf 5.7 minutes for the wild type enzyme). A typical example of the data obtained for the kinetics of thermal inactivation (used to calculate these half-lives) is shown in figure 2.

These three genes were sequenced to determine what mutations had been introduced. Locations of mutations from the amino acid sequence of the wild type for each of the three first generation variants are shown in figure 3. The mutations discovered in 2A12 and 1E8 have not been observed previously. Of the two mutations in 4E11, the second (Glu255 -> His) is thought to be neutral to thermostability. This is because the first mutation (Asn218 -> Ser) has been observed previously (3), and has been shown to decrease the thermal inactivation rate of the enzyme, leading to an activity half-life about equal to that of 4E11.

Because of early difficulty in accurately measuring thermal inactivation rates, 2A12 was chosen as the parent of the second generation. Though analysis of the mutants produced in the second generation is not yet completed, it is still possible to glean some information from that generation. As the mutants in both generations were screened, the fractional residual activity of each one was recorded. (The fractional residual activity is the activity after incubation divided by the activity before incubation.) These activities were plotted in descending order to generate a thermostability fitness profile (figures 4 and 5). Such a profile is a useful tool for determining the potential an enzyme has to be evolved for a trait (9). The profile forms a curve, with the residual activity of the parent enzyme located at some point along that curve. Each other point along the curve represents the residual activity of some enzyme that can be formed by subjecting the parent to random mutagenesis. Hence, the curve represents a sample of the possible enzymes that can be evolved from the wild type. It follows that the more of the curve that is at a higher residual activity than the parent, the more mutations there are that will improve the thermostability of the parent. Therefore, the potentials for evolution of various enzymes can be compared simply by comparing those enzymes' fitness profiles. As a directed evolution experiment progresses, each generation will have a different fitness profile. In theory, with each new generation, more possible mutations will be exhausted, and the portion of the curve that is above the wild type will eventually become smaller. As this portion of the curve becomes smaller, it will become more difficult to evolve the enzyme further. Hence, the fitness profile can be a tool to determine at what point in a directed evolution experiment it is no longer worthwhile to progress with further generations. The curves in figures 4 and 5 have similarly sized portions above the parent enzyme. This indicates that the experiment has great potential to proceed with generations after the second generation.

Conclusions

Two novel mutations which increase the thermostability of subtilisin E have been discovered. Thermal inactivation assays indicate that the most stable variant evolved has an activity half-life nearly four times that of the wild type. Thermostability fitness profiles indicate that evolution should be continued beyond the second generation.

As well as continuing the evolution process, future research will seek to determine the melting temperatures (T_M) of the new variants. In addition, thermal inactivation assays and sequencing will be carried out on the best variants of the second, third, etc. generations. Eventually, attempts will be made to explain the molecular origin of thermostabilization due to the mutations discovered.

Acknowledgments

The author would like to thank Dr. Frances Arnold, who sponsored this project, and Huimin Zhao for their help. This project was undertaken as part of the SURF program, which provided funding and support. Support was also provided by the National Science Foundation (REU) and by the Department of Energy.

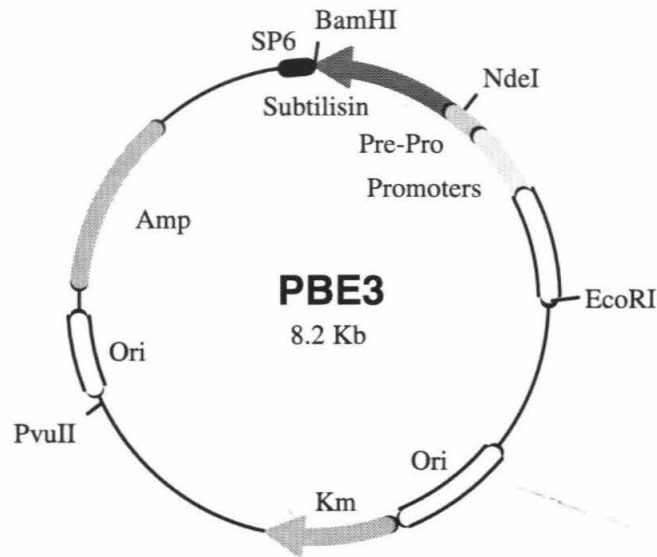


Figure 1. This diagram of the plasmid vector used in this project shows the origins of replication for both *E. coli* and *B. subtilis* (ori). It also shows the genes for subtilisin, ampicillin resistance (Amp) and kanamycin resistance (Km).

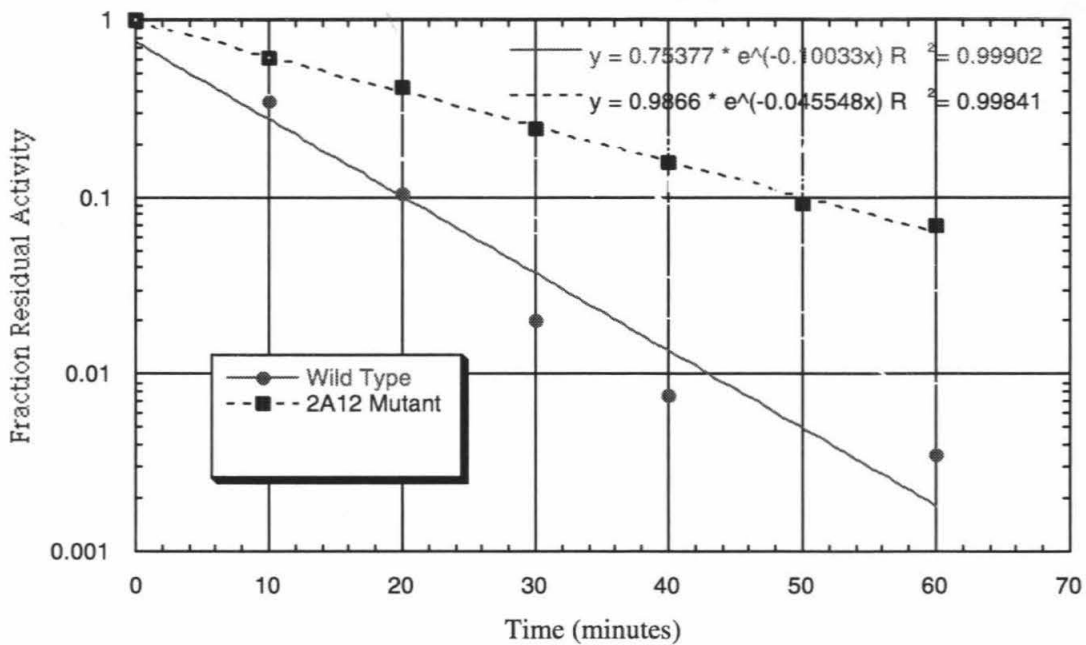


Figure 2: Thermal inactivation of wild type and of the 2A12 mutant

The activities of the enzymes were measured every five minutes during a 60 minute incubation at 65°C. Each point was normalized to the initial activity, giving fraction residual activity. The data were fitted to an exponential curve in order to obtain a rate of inactivation ($y=A*e^{(-rate*x)}$). The quality of the fits is indicated by the correlation coefficients (R^2).

Mutant Name	Base substitution	Amino acid substitution
2A12	CAA → CAG (A->G)	10, synonymous
	ACA → ACT (A->T)	20, synonymous
	AAC → GAC (A->G)	Asn181 → Asp
	TTA → CTA (T->C)	233, synonymous
4E11	GAT → GAC (T->C)	97, synonymous
	ATT → ATA (T->A)	115, synonymous
	CTT → CTC (T->C)	126, synonymous
	AAC → AGC (A->G)	Asn218 → Ser
	GGA → GGT (A->T)	229, synonymous
	CAA → CTA (A->T)	Glu275 → His
1E8	CTT → TTT (C->T)	Leu235 → Phe

Figure 3: Mutations in the first generation

Shown are the mutations in the gene and the amino acid sequence of subtilisin E for the 2A12, 4E11, and 1E8 variants in the first generation. Synonymous mutations are those for which a change in the DNA sequence did not result in a change in the amino acid sequence.

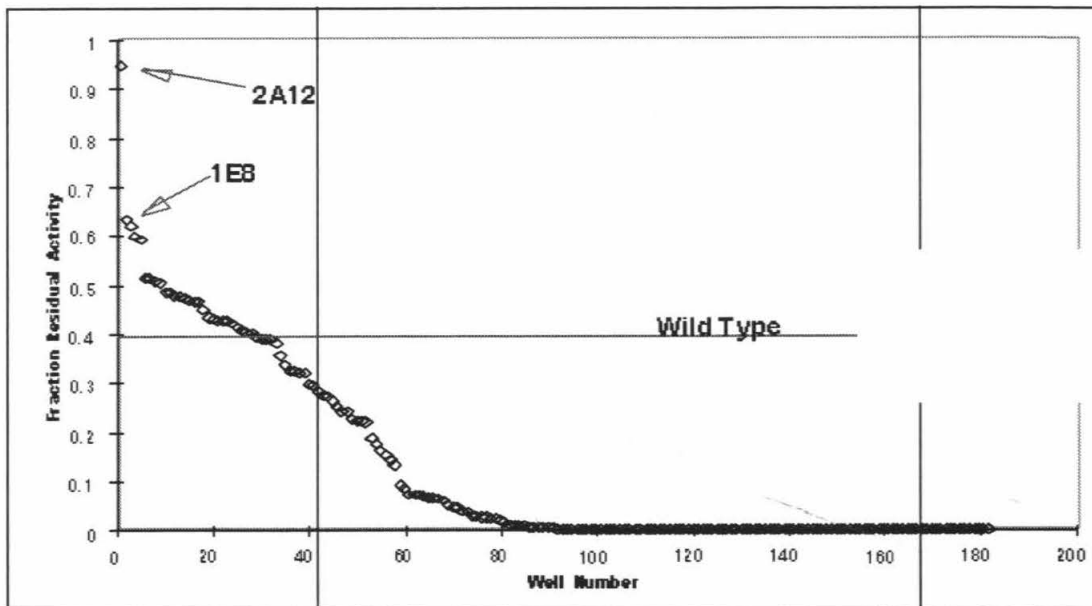


Figure 4: Thermostability fitness profile of the first generation

The fractional residual activity of each mutant in the first generation is plotted. The mutants are arranged in order of descending fractional residual activity. These data were taken during a preliminary screening of the first generation. The positions of both the 1E8 and 2A12 mutants are indicated. 4E11 was detected in a second screening of this generation.

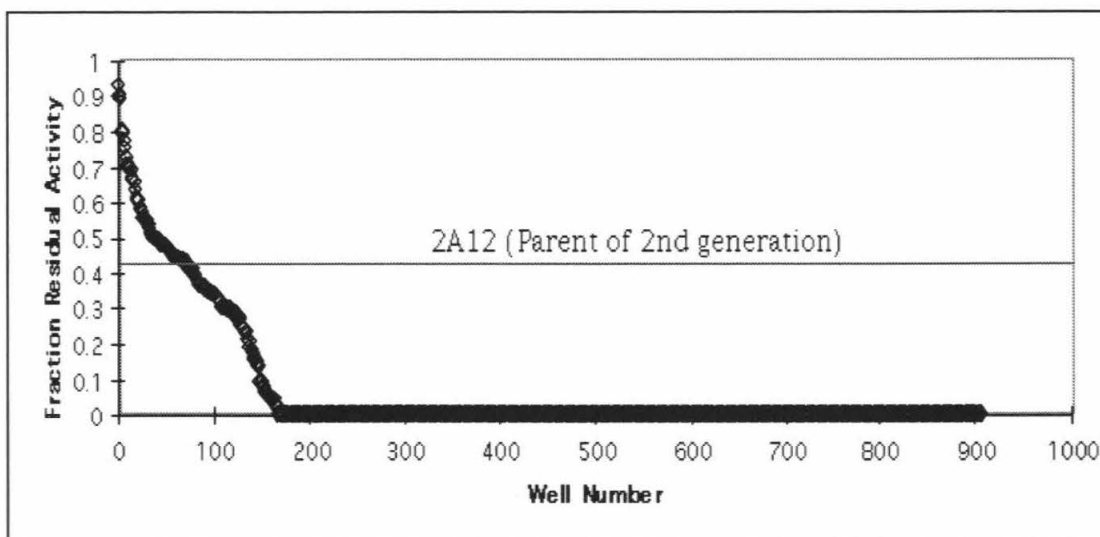


Figure 5: Thermostability fitness profile of second generation

The fractional residual activity of each mutant in the second generation is plotted. The mutants are arranged in order of descending fractional residual activity. Clearly, most mutations are deleterious, resulting in complete inactivation of the enzyme. However, since a large portion of the curve lays above the activity of the parent enzyme (2A12), there are many beneficial mutations as well. This indicates that there is significant potential for further evolution of the enzyme.

References

- Adams, Michael W.W. and Robert M. Kelly. *C&EN*. December 18, 1995.
- Arnold, Frances H. *FASEB*. 7:744-749. 1993.
- Bryan, Philip N. "Engineering Dramatic Increases in the Stability of Subtilisin." from *Stability of Protein Pharmaceuticals*. Plenum Press, New York. 1992.
- Bryan, Philip N., Michele L. Rollence, Michael W. Pantoliano, James Wood, Barry C. Finzel, Gary L. Gilliard, Andrew J. Howard, and Thomas L. Poulos. *Proteins: Structure, Function, and Genetics*. 1:326-334. 1986.
- Gupta, Munishwar N. *Biotechnology and Applied Biochemistry*. 14:1-11. 1991.
- Caldwell, R. Craig and Gerald F. Joyce. *PCR Methods and Applications*. 2:28-30. 1992.
- Flory, Nathalie, Maureen Gorman, Pedro M. Coutinho, Clark Ford, and Peter J. Reilly. *Protein Engineering*. 8:1005-1012. 1994.
- Frömmel, Cornelius and Chris Sandler. *Proteins: Structure, Function, and Genetics*. 5:22-37. 1989.
- Moore, Jeff. Ph.D. Thesis, California Institute of Technology. 1996.

Key Words

Directed Evolution, Enzyme Thermostability, Error-Prone PCR, Enzyme Thermostability, Protease Activity, Protein Engineering, Subtilisin E, Thermostabilization.

Batch Processes in Combinatorial Auctions: An Experimental Project

Pinar Karaca, Swarthmore College, and David P. Porter

This research tackles the mitigation of the “threshold problem” in “combinatorial simultaneous multiple unit auctions.” There exists no theory that would be guiding in approaching the problem. Therefore this project uses experimental methods as a design instrument. “Batch User Selection Mechanism (BUSM)” is designed for the purpose of conducting experiments in order to identify the optimal information structure and the stopping rule in alleviating the “threshold problem.” The uniqueness of the BUSM comes from its integration of both packaging and the batch process into a simultaneous multiple unit auction. BUSM is tested with two different kinds of voluntary information structures called “Queues” and with two different stopping rules. The results of the experiments reveal that the Queues improve the coordination and help lessen the “threshold problem.”

Introduction

Auctions have become an essential component of complex resource allocation in economics. An example of an environment where one needs an advanced auction mechanism is the Federal Communications Commission’s (FCC) Spectrum Auction. There are some important features of the auctioning of the Personal Communication Services (PCS) Licenses :¹

- a) The FCC auction involves the auctioning of non-identical spectrum blocks.
- b) Synergies from owning specific combinations of licenses exist.
- c) The bidder preferences are partially overlapping.
- d) FCC’s goal is to assign more than 2500 heterogeneous PCS licenses to those bidders who value them the most, and hence can be expected to provide new services to the public quickly.

Although participants in FCC auctions have values for the packages of licenses, the FCC has not yet used an auction in which bidders are allowed to submit bids on both individual items and on combinations of items. The conjecture is that allowing packaging in FCC spectrum auctions would be more efficient:

- a) in handling the issue of synergies that exist from owning specific combinations of licenses and,
- b) in determining the optimal (the highest value) outcome of the given overlapping preferences.

An auction mechanism which fits closest to such FCC constraints has been designed by Banks, Ledyard and Porter of the California Institute of Technology. Their “Adaptive User Selection Mechanism (AUSM)” is a computerized ascending bid auction which allows participants to submit bids for single items as well as the combinations of items. In AUSM, all items and packages are auctioned continuously and simultaneously. As Bykowsky, Cull and Ledyard point out, any AUSM-like mechanism can create a “**threshold**” problem. As they state the problem: “Specifically, bidders who wish to obtain single or small subsets of the licenses may have difficulty coordinating their bids with other bidders to displace bidders who have successfully bid for a large subset.”² Experimental evidence suggests that communication improves coordination, and such coordination can overcome the threshold problem.³ Therefore, the stanby queue, which is a voluntary information mechanism, is designed for AUSM

AUSM needs to be modified so that it fits the batch processes. In bidding environments, such as that of FCC, which involve many items, constraints and many participants, any continuous mechanism would result in difficulties. Continuous and quick action may at times hamper coordination between the buyers especially when buyers make group decisions. Therefore, for auctions such as the FCC Spectrum Auction, a batch process appears to be essential. The batch process indicates that the auction proceeds round by round. The challenge of the design of BUSM has been to integrate packaging into the batch process auctions under FCC constraints. BUSM is similar to the AUSM in that it allows bids for single items as well as packages. It is a computerized combinatorial auction and the bidders are linked together through a computer network.⁴

Materials and Methods:

A) BUSM MECHANISM DESIGN:

- 1) One-Sided Market: BUSM operates on one-sided markets which have only buyers. The FCC example was the main inspiration for this choice.
- 2) Both Single Items and Packaging Allowed:

Consider example 1: Suppose there are 3 bidders and 3 items for sale. Further suppose that the bidders have values for packages of items as well as single items. For example, bidder 1 has a value of 95 francs for items A, B and C. Because packaging is allowed, bidder 1 can submit a single bid for items A, B and C.

Example 1 Package Values of Bidders (in franc amounts)

<u>BIDDER 1</u>	<u>BIDDER 2</u>	<u>BIDDER 3</u>
ABC=95	AB= 70	BC= 30
AC = 60	B= 10	C= 30

1st Best	Outcome: AB(bidder 2) + C(bidder 3) = 100	Efficiency:	100%
2nd Best	Outcome: ABC(bidder 1) = 95	Efficiency	95%

This means that the most optimal outcome is for bidder 2 to get items A and B, and bidder 3 to get item C.

- 3) Batch Process: Market is composed of rounds:

The process starts with the first round. Bidders submit bids for their packages or single items. There is no limit to the number of bids one can submit. The market is completely private. Each bidder has information on only his own bids. At the end of the round, the solver runs through the submitted bids and picks those bids which, in total, maximize the revenue generated. Results are then announced publicly, and the winner names, the packages they win, and the winning bids are posted. The second round starts. The same procedure follows. At the end of the second round, depending on the stopping rule, the auction either continues or ends.

Below is a scenario which displays the coordination problem in such a combinatorial auction:

Suppose in round 1, bidders bid as below:

Bidder 1: bids 40 francs for the package ABC
Bidder 2: bids 10 francs for the item B
Bidder 3: bids 10 francs for the item C

The round ends, and results are posted: The winner of the Round is **Bidder 1**. He wins items A, B and C with a bid of 40 francs. Although bidder 2 has value for the package A and B, and that bidder 3 has value for C, they did not have any means of coordination. This is an example of the "threshold problem".

Suppose we start round 2, and the bids submitted are as below:

Bidder 1: bids 40 francs for the package ABC
Bidder 2: bids 40 francs for the package AB
Bidder 3: bids 10 francs for the item C

The round ends, and results are posted. The winners of the Round are: **Bidder 2 and 3**. Bidder 2 wins items A and B. Bidder 3 wins item C. For this case, they were able to coordinate by luck, and they outbid bidder 1. Suppose the stopping rule allows us to continue another round, and that the bids submitted in round 3 are as below:

- Bidder 1: bids 70 francs for the package ABC
- Bidder 2: bids 55 francs for the package AB
- Bidder 3: bids 10 francs for the item C

Round ends, results are posted. The winner of the Round is **Bidder 1**. He wins items A, B and C. Because bidders 2 and 3 have no means of communication, they couldn't guess and coordinate against bidder 1. If the stopping rule ends the auction at this point, Bidder 1 leaves the auction as the winner although this outcome was not the most efficient one. This is a clear illustration of the "threshold" problem in the BUSM.

Therefore, a secondary-mechanism needs to be designed in order to allow the bidders to coordinate and reveal public information if they chose to do so. Two main information structures called the "Queues" were designed for this purpose.

4) The Queues:

a) Continuous Queue: The market (which is completely private) remains functioning on the round by round basis, but within each round, there exists a public bulletin board to which bidders can publicly submit bids. At the end of the round, the solver goes through both the market and the queue to find the winning result. The solver makes no difference between the private market and the queue. The queue is continuously available.

b) Interim Queue: This queue can be considered a round by round queue. The market also operates round by round. In the first half of the round, bidders can submit bids privately both to the Queue and the market. In the middle of the round, the auctioneer announces that the Queue is visible. From that point afterwards, nobody can submit new bids to the queue. Participants can have the Queue opened on their screen, and see what bids were submitted (during the first half of the round) including the bidders who submitted them, and the packages for which they were submitted. At the end of the round, the solver finds the results without discriminating between the bids submitted to the market and to the queue.

5) How to stop the market ?

The experiments tested two different kinds of stopping rules:⁵

a) % Change Stopping Rule:

The market lasts for at least 2 rounds. After the second round, the market closes if the aggregate value of the standing bids (the surplus) does not increase by 5% over the previous round. Otherwise, the market closes in round 6. The items are awarded based on the outcome of the final round.

b) FCC Stopping Rule:

This stopping rule is designed after the stopping rule that the FCC uses. Activity rules are imposed in order to speed up the activity. In simple terms, the auction continues until there are no new bids on any single items or packages.

B) BUSM ENVIRONMENT DESIGN:

The BUSM was tested on three different environments which were all composed of 6 bidders and 6 items (A, B, C, D, E, F) :

<u>Environment 1:</u>		Value Sheets of Bidders					
Bidder id:	<u>1</u>	<u>2</u>	<u>3</u>	<u>4</u>	<u>5</u>	<u>6</u>	
	A = 34	B = 40	ABC=120	D=30	F=30	D =44	
	AC=116	BE=110	CE= 80	BD=40	BC=90	AF=50	
	BD=50	DF= 94	DF=104	ABF=56	CE=100	BDE= 154	
	BE= 90	AD= 78	ACF=120	ABCDEF=314	ACF=146	BDEF=198	

100 % efficiency level 95% efficiency level
AC(1) + BE(2) + DF(3) = 330 ABCDEF(4) = 314

This is an environment in which the threshold problem is the most likely to occur. The optimal outcome (100% efficiency level outcome) is shared between 3 bidders. Specifically, for this outcome, bidder 1 should win items A and C, bidder 2 should win items B and E, and bidder 3 should win items D and F. The outcome which has only 1 person, in the sense that 1 bidder has a high value for all the items A, B,C D, E and F is at 95% efficiency level, which is very close to the first best outcome. There exists a big challenge for the bidders of the 100% efficiency level outcome to coordinate in order to outbid the single buyer of 95% efficiency level outcome. Let us from now on, call this single buyer, the "big guy", and the smaller package bidders of the 100% efficiency level outcome, the "smaller guys."

<u>Environment 2:</u>		Value Sheets of Bidders					
Bidder id:	<u>1</u>	<u>2</u>	<u>3</u>	<u>4</u>	<u>5</u>	<u>6</u>	
	A= 20	B= 25	ABC= 90	ABCDEF=248	F= 30	D= 31	
	AC= 70	BE= 100	DF= 160	BE= 75	BC= 70	DF= 95	
	BD= 70	AD= 51	ACF= 95	CE= 90	CE= 109	BDE= 131	
	ABF= 60	AF= 2	D= 25	BD= 65	ACF= 100	BDEF= 178	

100 % efficiency level 75% efficiency level
AC(1) + BE(2) + DF(3) = 330 ABCDEF(4) = 248

This is a more relaxed environment for the "smaller guys". The big guy sits at an efficiency level of 75%, where as the optimal outcome of 3 "smaller guys" sits at 100% efficiency level. The gap between the "big guy" and the optimal outcome is larger. Therefore, it is expected that there will be less pressure on the "smaller guys" in terms of coordination.

<u>Environment 3:</u>		Value Sheets of Bidders					
Bidder id:	<u>1</u>	<u>2</u>	<u>3</u>	<u>4</u>	<u>5</u>	<u>6</u>	
	A=49	B =49	ABC=90	D=15	F=5	D=21	
	AC=95	BE=110	CE=80	BD=50	BC=70	AF=49	
	BD= 60	DF=90	DF=125	ABF=88	CE=91	BDE=131	
	BE=7	AD=70	ACF=80	ABCDEF=248	ACF=100	BDEF=153	

100 % efficiency level 75% efficiency level
AC(1) + BE(2) + DF(3) = 330 ABCDEF(4) = 248

This is even a more relaxed environment than Environment 2. The big guy still sits at 75% efficiency level, but this time there are more possible outcomes between the 75% and the 100% efficiency levels as compared to Environment 2.

Besides the "big guy" versus "smaller guys" aspect of the environment design, it is important to mention that a non-unique set of competitive equilibrium prices exists for each environment. Competitive equilibrium is the set of single item prices such that if one posts them, the first best outcome occurs. A set of critical equilibrium prices which minimize the revenue that the auction generates for the 3 environments are:

Environment 1: $A=43 + B=37 + C=68 + D=59 + E=68 + F=40 = 315$ francs

Environment 2: $A=16 + B=25 + C=52 + D=50 + E=58 + F=48 = 249$ francs

Environment 3: $A=16 + B=25 + C=52 + D=50 + E=58 + F=48 = 249$ francs

C) EXPERIMENTAL PROCEDURES:

Each experiment consisted of six bidders who were either Caltech undergraduates or, SURF students at Caltech. All the participants were placed in the same room on different computers. One auctioneer was in charge of actively communicating with the participants, while the other auctioneer was in charge of operating the software. Before each experiment, the instructions were read out loud while demonstrating some examples. Participants were allowed and encouraged to ask as many questions as they wished at that period. The instructions were followed by a practice period. Each participant was given a folder with the instructions, their redemption value sheet, accounting sheet, eligibility sheet (for those experiments with the FCC stopping rule), scratch paper, a pencil and a calculator.⁶

During the experiment: During the experiment, participants were allowed to delete any bid from the market before the end of the round. However, they were not allowed to delete any bids from the Queues. One round on average took a minute and a half. Bidders were notified just before the closing of the round. If there was a bidder in the process of submitting her/his bid, she/he was generally allowed to complete his submission.

Experimental Results and Discussion Using the %Change Stopping Rule:

A) Efficiency Tests

1) The distribution of the results among different efficiency levels:

As mentioned earlier, Environment 1 is the hardest environment on smaller guys, while environments 2 and 3 are more relaxed. As expected, threshold problem occurs the most in Environment 1. Among 20 observations in Environment 1, 14 fall in the “big guy” outcome and only 4 observations fall into the 100% efficiency outcome (“smaller guys” being successful). However, the threshold problem is observed (the big guy becomes the winner) mostly in those experiments in which no information structure was used. 50% of the auctions in Environment 1 which resulted in the “big guy” outcome were conducted using no Queue. 36% were conducted with the Continuous Queue, and only 14% were conducted with the Interim Queue. It is also important to note that the 100% efficiency outcome never occurred in those experiments with no Queue. 75% of the auctions which resulted in the 100% efficiency outcome were conducted with the Interim Queue, and 25% with the Continuous Queue.

These results show that the information structure plays an important role in such an environment in which there exists a strong competition between the “smaller guys” and the “big guy” due to the small gap between the efficiency levels of the two outcomes. The Interim Queue performs better than Continuous Queue in dealing with the threshold problem. The results in Environment 2 and 3 indicate that there is no significant difference between the different information structures. This observation reveals that in environments which are more biased towards the smaller guys, the information structure used does not matter since there is less possibility for the threshold problem to occur.

2) The mean efficiency

Another way of comparing the different information structures is to look at the average efficiency each achieved while also taking into consideration the sample standard deviation within each group. As Table 1 shows, in terms of the mean efficiency, the Interim Queue followed by the Continuous Queue performs the best in Environment 1. Environment 2 results indicate that the auctions without the Queue have performed the best, and that the mean efficiencies of the two different

Queues are very close to each other. Environment 3 was tested with a fewer auctions, but the small number of observations obtained for Environment 3 identify the Interim Queue as having generated the most efficient outcome.

Table 1: Mean Efficiency(%) (using % Change Stopping Rule)

	<u>No Queue</u>	<u>Interim Queue</u>	<u>Continuous Queue</u>
ENVIRONMENT 1:	92.25	97.5	95.83
ENVIRONMENT 2:	94.57	92.38	92.5
ENVIRONMENT 3:	97.3	100	80

B) Tackling the Threshold Problem:

In looking at the data for which the “big guy” managed to be the winner, one can identify two main components of the threshold problem:

a) Strategic Component: Bias created by the Stopping Rule

The % Change Stopping Rule closes the auction if the surplus does not go up by 5% or more compared to the previous round. The winners of the auction are determined based on the final round’s results. Therefore, one often encounters a scenario in which the “big guy” holds back information by not bidding for all six items in the earlier rounds. He then bids for all six items by increasing the previous round’s total bids by less than 5%. Therefore the auction stops, and the winner becomes the “big guy”. In the experimental data, those auctions in which the big guy appears in the last round by outbidding a higher efficiency outcome than his own are identified as outcomes due to the strategic component of the “threshold problem”.

b) Coordination Component:

A coordination problem occurs, because it is difficult for two or more bidders to coordinate against the “big guy.” The “big guy” submits bids in earlier rounds, but the “smaller guys” cannot coordinate together to outbid the “big guy”. From the data, those auctions in which the “big guy” appears earlier but the “smaller guys” cannot outbid him are identified as outcomes due to the coordination problem.

Figure 1: The Queues and the two identified Components of the “threshold problem” in Environment 1



As Figure 1 shows, in Environment 1, the coordination problem was observed the most in those auctions conducted with no Queue. Interestingly, no coordination problem was observed in those auctions conducted with the Interim Queue. Some coordination problem was observed with the Continuous Queue. Environment 1 shows that the strategic problem occurs the most for the auctions with the Queues, especially in those with the Continuous Queue. This is because the “big guy” has an opportunity to gain information about the value sheets of the “smaller guys” from their interaction through the Queue. Therefore the “big guy” has more advantage in strategizing his decisions compared to the “smaller guys”. Environment 2 and 3 has no indication about the occurrence of coordination problem. It was expected, from the beginning that these environments would be easier for the smaller guys and that no aggressive competition between the “smaller guys” and the “big guy” was likely to occur. In conclusion, the queues, especially the Interim Queue, help solve the coordination based component of the threshold problem. However, the strategic component of the threshold problem still remains a problem regardless of the information structure we use. At this point, had there been a way to eliminate the strategic problem, the mechanism would have done a great job in

eliminating the threshold problem.

Experimental Results Using the FCC Stopping Rule:

As mentioned earlier, the FCC Stopping Rule was designed so that the auction would continue until there were no new bids on any of the items. The activity rules ensured that the buyers kept active during the auction. Therefore, the conjecture is that the strategic problem which occurs due to the bias in the % Change Stopping Rule would disappear in the auctions conducted with the FCC Stopping rule. A set of experiments were thus conducted using the FCC stopping rule and the Interim Queue. Among all the 14 auctions, only two "big guy" outcomes at 95% efficiency level occurred. They were both mistakes on the subjects' account during the experiment. In environment 1, 97.5 % average efficiency is observed due to this mistake. No strategic problem, and no coordination problem were observed. In Environments 2 and 3, the mean efficiencies were 100%.

Summary and Conclusions:

Environment 1, being the most challenging environment provided some interesting data. In terms of efficiency performance, the Interim Queue performed best in Environment 1. In environments 2 and 3, the information structure did not matter. It is observed that the %Change stopping rule created a bias, and the FCC Stopping rule did a better job in eliminating the threshold problem. In conclusion, this research suggests the use of the Interim Queue with the FCC Stopping Rule as the best batch process\simultaneous multiple unit auction with packaging. The efficiency performance has a great deal of significant evidence for this suggestion.

Acknowledgments:

I thank Minnie Ingersoll of Stanford University, and Wes Boudville of Caltech for their assistance for this project. I thank David P.Porter, my SURF advisor, and John Ledyard of Caltech for their advice and guidance. I also thank the SURF program for this great research opportunity.

References

- Banks, Jeffrey S., Ledyard, John O., Porter, David P., "Allocating Uncertain and Unresponsive Resources: An Experimental Approach," *RAND Journal of Economics*, Vol 20. No.1 .Spring. 1989
- Bykowsky, Mark M., Cull, Robert J., Ledyard, John O., " Mutually Destructive Bidding : The FCC Auction Design Problem," *Division of the Humanities and Social Sciences, Caltech Social Science Working Paper 916*. 1995
- Gibbons, Robert, *Game Theory for Applied Economists*, Princeton University Press, Princeton, NJ. 1992
- Kagel, John H., Roth, Alvin E., *The Handbook of Experimental Economics*, Princeton University Press, Princeton, NJ. 1995
- Ledyard, John O., Noussair Charles, Porter, David, "The Allocation of a Shared Resource Within an Organization," *Division of the Humanities and Social Sciences, Caltech, Social Science Working Paper 917*. 1995.
- Ledyard, John O., Porter, David, Rangel, Antonio, "The Results of Some Tests of Mechanism Designs for the Allocation and Pricing of Collections of Heterogeneous Items." 1996
- McMillan, John, *Games Strategies, and Managers*, Oxford University Press. New York, Oxford. 1992
- Olson, Mark, Porter, David, "Resource Allocation in Complex Systems: Auctions, Priority and Scheduling.", Plott, Charles, "An Updated Review of Industrial Organization: Applications of Experimental Methods," *Handbook of Industrial Organization*, Volume II, Edited by R. Schmalensee and R.D Willig, *Elsevier Science Publishers*, B.V. 1989
- Rassenti, S. J., Smith V.L., Bulfin, R.L, "A Combinatorial Auction Mechanism for Airport Time Slot Allocation," *Discussion Paper, College of Business & Public Administration, University of Arizona*, Discussion Paper 81-27. 1981, FCC Home Page on Internet: (<http://www.fcc.gov/>)

¹ Mark M. Bykowsky, Robert, J.Cull, John O. Ledyard, Mutually Destructive Bidding: The FCC Auction Design Problem, Division of the Humanities and Social Sciences, California Institute of Technology, Social Science Working Paper 916, January 1995, pg: 4,5,6

² ibid., pg: 21

³ ibid., pg:23

⁴ The software for the BUSM is designed by Wes Boudville of Caltech

⁵ Stopping Rules are designed by Minnie Ingersoll . See the SURF report of Pinar Karaca for detailed instructions.

⁶ The software was designed by Wes Boudville of Caltech

A Search for High Redshift Quasars

Vandana Desai and S. George Djorgovski

We are conducting a systematic search for bright quasars with redshift greater than 4, which correspond to those quasars formed when the universe was 5-10% of its current age. Due to Lyman alpha absorption in the green part of these quasars' spectra, and Lyman alpha emission in the red region, quasars appear much brighter in red than green. Also, they appear starlike at optical wavelengths. These characteristics of the quasar spectrum make the data from the Second Palomar Sky Survey, which exist in green, red, and infrared bands, especially useful for searching for high redshift quasars. With the help of sophisticated classification and cataloging software called SKICAT, objects observed in the survey which match the spectral characteristics of quasars have been selected. Spectra of the final candidates were taken at the Palomar 200" telescope. Thirteen new fields, amounting to about 468 square degrees of the Northern Sky, have been covered. Seven new quasars with redshift greater than 4 have been discovered.

Introduction

Quasars (Quasi-Stellar Objects) serve as useful probes into the history of the universe. As the most luminous objects known to astronomers, they can be detected at further distances than any other astronomical object. Their high luminosity allows reliable spectra to be taken, which can then be interpreted to reveal the properties of the intervening intergalactic medium, showing how it has evolved through time. In cosmological terms, observing a high redshift quasar is like looking back into the past. Quasars as probes of earlier epochs in the universe can be powerful tools in the study of the formation of galaxies and other large scale structure in the universe. In order to take advantage of these tools, a determination of the Quasar Luminosity Function (QLF) must be made. The QLF has been found to increase with redshift (Schmidt 1968, Boyle *et al.* 1993). This trend has been confirmed observationally up to a redshift of 2.2. It is reasonable to assume, however, that the QLF reaches a maximum value at some higher redshift, decreasing for redshifts greater than that. This peak in the QLF would represent the epoch in which quasars were formed, and may provide a link to the epoch of the formation of other large scale structure in the universe. In order to take full advantage of these properties of quasars, a systematic survey of quasars at high redshift is necessary.

Data

An ongoing search for high redshift quasars is being conducted at Caltech using data from the Second Palomar Observatory Sky Survey (POSSII). The Survey consists of photographic plates exposed at the Palomar 48 inch Oschin Schmidt telescope. It is being carried out in three colors: blue-green (J), red (F), and infrared (N). Each plate covers 6.6 degrees by 6.6 degrees of the Northern Sky. A digitized version of this survey (DPOSS) is being created at the Space Telescope Science Institute (STScI) in collaboration with Caltech. In order to make efficient use of this digitized survey, the Caltech Astronomy Department and the JPL Artificial Intelligence Group have created the Sky Image Cataloging and Analysis Tool (SKICAT). SKICAT classifies the objects found in the survey and catalogs them for easy manipulation. Once catalogs in J, F, and N are made for a given field they are matched together by right ascension and declination. The result is a matched catalog that can be searched for candidate quasars.

Approach

Once a matched catalog has been created, candidate quasars must be selected out of the tens of millions of objects in the catalog. Since quasars appear starlike in the optical regime, and are brightest in the F band at the redshifts of interest, all objects that have been classified as stars in F are selected. Since plate magnitudes are only reliable between 16.5^m and 19.6^m, only objects within this magnitude range can be considered for quasar candidacy. The objects that meet these criteria are then divided into four groups: those that are observed in J, F, and N; those that are observed in J and F only; those that are observed in N and F only; and those that are observed only in F. The instrumental J, F, and N magnitudes are then calibrated to Gunn-Thuann gri (see "Calibration").

The plate is then divided into 16 blocks, to facilitate flat-fielding. Both (g-r) and (r-i) core magnitude colors are computed for objects observed in all three bands in each 16th of the plate. Sixteen color-color plots ((r-i) vs. (g-r)) are then produced. The resultant stellar loci are aligned to a standard location determined by the stellar locus of one of the central sixteenths. This serves to flat-field the plate. The flat-fielded core magnitudes are then divided into half magnitude bins, and color-color diagrams are again made. The stellar locus for each half-magnitude bin is aligned to a standard location for total magnitude colors, determined by four well-calibrated fields. Quasars with redshifts between 4.0 and 4.8 have a larger (g-r) color than stars, meaning that these quasars lie outside of the stellar locus on color-color diagrams. Objects whose large (g-r) colors pull them sufficiently far from the stellar locus are added to the candidate list. The cut-off colors have been determined empirically for each half-magnitude bin.

For objects detected only in the J and F bands, color magnitude diagrams are used to filter out objects with a (g-r) color less than a limit determined by the magnitude of the object. A magnitude greater than 18^m is required for consideration for quasar candidacy. Final image examination is carried out before candidate confirmation.

For objects detected only in the F and N bands, image examination is carried out. The images are examined to verify that there was no detection in J. Generally, image examination will reveal that most objects are visible in J, and these objects are determined to have been mismatched. These objects are not considered as quasar candidates. Those objects that truly have no J detection are added to the candidate list.

Finally, objects detected only in the F band are considered. Image examination in all three bands reveals the majority of these objects as dust particles or a plate defect. Objects that have been mismatched and display N detection but no J detection are added to the candidate list.

Once a list of possible quasar candidates has been made, finding charts are made for each object on the list. These charts serve as a map for taking spectra of the objects. Spectra are taken at the Palomar 200 inch telescope using the Double Spectrograph. Exposure times for each candidate vary between 300 seconds to 600 seconds, depending on the magnitude of the object. Redshifts are computed from the wavelengths at which known Lyman alpha lines are detected.

Calibration

Galaxy count calibration was used for calibrating the instrumental colors to the standard Gunn-Thuan gri colors when the more proper CCD calibration was unavailable. While quasars have been found using this calibration, its validity and therefore the completeness of the survey for the fields for which this method was used is doubtful. Galaxy counts cannot be accurately applied to star counts for calibration. CCD calibration is necessary. Also, the method by which core magnitudes have been shifted to the standard location of total magnitudes is less accurate than it could be ideally. A possible alternative method involves the fitting of the plot of total magnitude versus core magnitude, and applying the appropriate transformation between them. Initial results using this new method have matched extremely well with CCD data. In addition, we are considering the improvement of vignetting over manual flat-fielding, as discussed above. It is possible that, in order to ensure completeness in this survey, past fields will have to be re-processed in this new manner.

Results

Candidate selection was carried out for thirteen new fields. Seven new quasars were discovered, all with redshift greater than 4.

QSO	z	r	RA	Dec
PSS 0003+2730	4.26	19.0	00 03 23.1	+27 30 22
PSS 0106+2601	4.32	19.4	01 06 00.8	+26 01 02
PSS 0134+3307	4.52	18.8	01 34 21.6	+33 07 56
PSS 0137+2837	4.30	19.0	01 37 12.3	+28 37 34
PSS 0747+4434	4.42	18.0	07 47 49.0	+44 34 16
PSS 1721+3256	4.03	19.2	17 21 06.8	+32 56 35
PSS 2122-0014	4.18	19.1	21 22 07.5	-00 14 45

Follow-up observation at Keck has revealed a 25^m companion galaxy to PSS 1721+3256. This galaxy shows no sign of having an Active Galactic Nucleus, but rather seems to be powered by star formation. It lies at approximately 13 arcseconds from the quasar, corresponding to a distance of about 85 kpc. This is the fourth galaxy found by astronomers to have redshift greater than 4. Two of these are powerful radio galaxies, and the third is also a quasar companion. It therefore seems likely that follow-up observations of objects near high redshift quasars could yield discoveries important to the study of the formation of early galaxies.

References

- Boyle, B.J. and Shanks, T. and Peterson, B.A., "The Evolution of Optically Selected QSOs," *MNRAS*, Vol. 235, 935-948, 1988
- Kennefick, et al., "A Multicolor CCD Survey for Faint Z-Greater-than-4 Quasars," *Astronomical Journal*, Vol. 111, 1816-1829, 1996
- Kennefick, et al., "The Luminosity Function of Z-Greater-than Quasars From the 2nd Palomar Sky Survey," *Astronomical Journal*, Vol. 110, 2553-2565, 1995.
- Kennefick, et al., "The Discovery of 5 Quasars at Z-Greater-than-4 Using the 2nd Palomar Sky Survey," *Astronomical Journal*, Vol.110, 78-86, 1995.
- Smith, J.D. and Thompson, D. and Djorgovski, S., "Multicolor Detection of High-Redshift Quasars .1. 2 Objects at Z-Greater-than-4," *Astronomical Journal*, Vol. 107, 24-27, 1994. Pasachoff, 6. Spinrad, Osmer, and Cheng, *The Farthest Things in the Universe*, Cambridge University Press, 1994, Cambridge.

3D Painting

Louis K. Thomas and Peter Schröder

Texture maps are very useful in 3D modeling because they allow the artist to add fine detail without the expense of added geometry. Painting a texture map with a 2D paint program can be difficult because of the distortions that occur when wrapping the texture around the 3D object. 3D paint programs allow the artist to paint directly on the object while the program manages the distortions transparently. Most 3D painting algorithms currently in use only sample the geometry of the object at a single point under the artist's brush. In this paper, we present a 3D paint program that uses a new algorithm that examines the geometry of the object being painted more thoroughly. Unlike point sampling algorithms, this algorithm behaves correctly on silhouette edges and is much less affected by distortions in the texture map. The program behaves more realistically than currently available 3D paint programs, and is suitable for use in immersive 3D environments.

Introduction

In 3D graphics, an easy way to add detail to a shape is to give it a texture-map. A texture map is an image that is used to modulate the surface color of a 3D object in order to add detail that would otherwise require exorbitant amounts of geometry. Applying a texture map is just like putting up wallpaper to make the walls of a room more interesting. Texture images are almost always two dimensional and stored as planes, since this corresponds to the flat drawing surfaces everyone is used to, like the page of a book or an artist's canvas.

A problem arises when the object to be textured is not perfectly flat. A flat image cannot be directly applied to a curved surface. The flat image must be distorted to fit it onto the surface. Mapping the image to the surface is generally not a problem. The difficulty lies in drawing a distorted picture on the flat image that produces the desired result when the image is mapped onto the shape.

The straightforward solution to the distortion problem is to show the 3D surface and allow the artist to paint directly on it. The creation of the distorted image should be handled automatically by the computer. This way, the artist will see and modify the image as it will actually appear.

The next problem that must be tackled is establishing how the artist interacts with the 3D surface. There are established tools and methods for painting objects in real life. How can these be simulated within a computer generated environment? Most artists are limited to the traditional computer interface consisting of a flat screen and a mouse. However, new hardware is being developed that will allow for more realistic 3D interfaces.

There are several commercial 3D paint programs currently available ("MeshPaint 3D" from Positron, "4D Paint" from 4DVISION, "Detailer" from MetaCreations, "Amazon 3D Paint" from Interactive Effects) that all use the same interface. The object is rendered to the screen as a still, 2D image. The artist uses a mouse to pick points where paint is to be applied. The point on the screen is translated into a point on the object, which is then translated into a point on the texture. Using this point, a standard 2D painting operation is performed, for example setting all the pixels within a small radius of the point to a new color. While this point-sampling method has some advantages, it has many disadvantages. The methods used to accelerate this algorithm do not work in a 3D environment. The algorithm assumes that the mapping from the texture plane to the object's surface is linear in the region where modifications are made. If this assumption does not hold true, for example if the artist tries to paint in a region of great distortion or tries to paint a large area, the results are non-intuitive and awkward. For example, painting a stripe along a conical object produces a line which is wide near the base of the cone and narrow near the tip although the artist never changes the size of the brush (see fig. 1). This algorithm does not perform correctly on silhouette edges either. For example, if an artist were painting along the rim of a dinner plate, she would find that a paint dot applied too near the edge on the front surface would wrap around the edge of the plate and color the back surface as well.

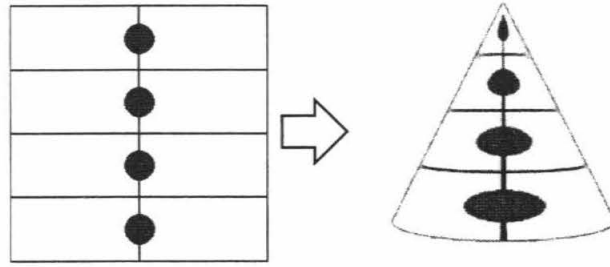


Figure 1. Distortions caused by a cylindrical mapping. When a texture containing dots of equal size is wrapped around a cone, the dots now seem to be of different sizes.

Other 3D paint methods have been developed as well. One commercial application (“StudioPaint 3D” from Alias|Wavefront) creates a 2D projection of the 3D object on the screen on which the user then paints. When the user is finished painting, the 2D view is projected back onto the 3D object, and suitably warped clippings of the painted 2D view are pasted onto the textures. This solves the problems of the point sampling algorithm, but is not suitable for a true 3D interface.

Pederson [3] has developed algorithms that allow for textures to be cut-and-pasted on smooth surfaces. This has many nice characteristics, but is not suitable for free-form painting. Chow [5] has developed an interesting algorithm using voxels containing color information instead of texture maps to paint complex models. The voxel algorithm allows for interesting effects that are defined over 3-space, such as cellular textures and Perlin noise functions [11]. However unlike texture mapped models, the shape of a voxel-painted model cannot be modified after it has been painted.

The algorithm we have developed is not affected by distortions in the texture mapping and properly handles silhouette edges, unlike the point sampling algorithm. It has similarities with the 2D projection algorithm, but is well suited for a truly 3D interface. Since our algorithm uses texture maps, models may be modified after they have been painted.

Method

In 2D paint programs, a dab of paint is placed on the image by picking a point on the image and then setting the pixels within a certain radius to the current color. This can also be done as a composition operation. The brush could be considered a small image that has a solid dot of color in the center and is transparent around the edges. This brush image is laid over the original image and the new image is the composition of the two (see fig. 2).

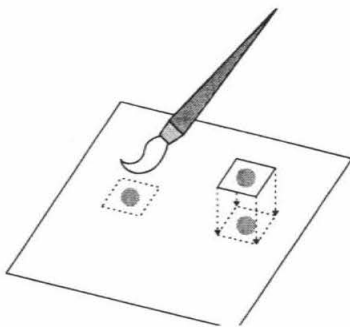


Figure 2. Projecting a small image straight down and compositing is equivalent to standard painting.

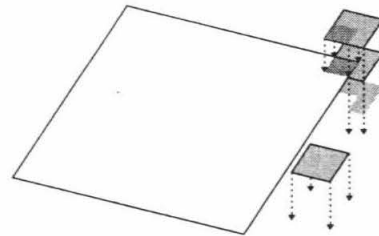


Figure 3. When the brush image is below the image to be painted, nothing happens. When the brush only partly covers the target image, the brush must be clipped.

This operation is easily done with current graphics hardware. We place the original image in the frame buffer. When we draw a textured square into the screen buffer, if the texture has an alpha channel (transparency information), we get exactly the blending operation described above. All we need are the coordinates of the corners of the brush square relative to the underlying image.

We can make this model three dimensional by assuming the image lies in the X-Y plane. The axis pointing away from the front of the image is the Z axis. We can now raise the brush image up off the original image. One can visualize this as holding a postage stamp over a regular piece of paper. Looking straight down and ignoring perspective, the result is the same. As long as we only translate (but do not

rotate) the brush, we just need to project the brush straight down and perform a composition to paint the image. Whether we move the brush with respect to the image or the image with respect to the brush, it makes no difference. If we move the paint brush underneath the image, we can no longer project the brush down onto the image. We consider the paint brush to be missing the image and composing the brush with the image produces no effect. If we slide the brush sideways so that it is partly on and partly off the original image, we need to clip the brush image so that we only tell the hardware to draw on the original image (see fig. 3).

If we raise the brush above the image and tilt the brush to the side, the projection of the brush onto the original image becomes distorted. The circular paint dot on the brush image becomes an ellipse on the original image. Since we are ignoring perspective, this is the same as if we were to project the corners of the brush onto the image and then stretch the square brush image so that it fit the rectangular footprint. The circle becomes an ellipse. (see fig. 4)

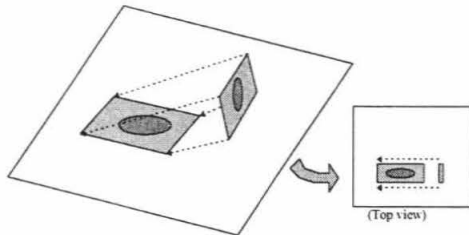


Figure 4. When the brush is tilted on its side, its projection on the target image becomes rectangular, and the circle on the brush becomes an ellipse on the target image.

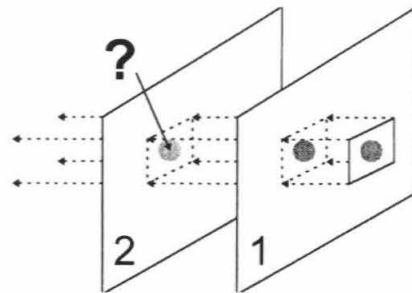


Figure 5. One would expect the first target image to occlude the second target image so that only the first image would be painted. The algorithm does not take occlusion into account, so a maximum depth is given to the brush instead.

If we tilt the brush and then place it half way through the image, what should happen? We say that only the part of the brush image above the surface of the original image will actually paint the original image. We need to clip the brush image so that only part of it above the original image is drawn.

Painting on a 3D model is now straightforward. After positioning the brush image over the model, we consider each textured surface separately. We project the brush onto it and clip the brush image to the edges of the textured surface. Then we draw a brush-textured polygon over the original surface texture and save the result. There is only one problem that we have not addressed. What happens when one surface is underneath another? Intuitively, we expect the bottom surface to be occluded. However, since our algorithm looks at each surface individually, it cannot make any decisions about occlusion. As a reasonable alternative, we say that the brush will not paint any surface further away than a certain distance. This doesn't actually solve the occlusion problem, but it does stop the 3D paint brush from painting distant surfaces that the artist was not expecting to be painted (see fig. 5).

The 3D paint brush now looks like a cube. Any surface that is facing "upwards" and placed within the brush-cube will be painted. The brush is totally independent from the viewer, which makes it suitable for immersive 3D interfaces. The brush can be moved and rotated in all directions. The brush can also be scaled along any of its axes. All these separate transforms can be conveniently summed up into a single affine transform. This "brush transform" is the transform that takes the cube $(0,0,0)-(1,1,1)$ into world space, translating, scaling, and rotating it appropriately so that it becomes the brush that the artist sees. When the artist moves the brush, she is actually modifying the brush transform.

Here we present the algorithm for painting as pseudo-code. Since the region on a surface that will be painted is the intersection between the brush-cube and the surface, it does not matter whether we clip the surface to the brush or the brush to the surface. In world-space, both the brush and the surface can have any orientation and scale, which makes clipping difficult. However, in brush-space, the brush is always the same size and is conveniently aligned with the axes. For this reason, we transform the surface to brush-space and clip the surface against the brush. Furthermore, since the brush-space and the brush-texture-space have the same scale and origin, we can use brush-space polygon vertices as texture coordinates.

```

for (each polygon) {

    use the inverse brush transform to transform the polygon vertices from world space to
brush space
    if (the polygon normal faces -Z-ward) {
        skip to next polygon
    }
    clip the polygon to the cube (0,0,0)-(1,1,-1), giving new polygon vertices
    appropriate texture coordinates based on the original texture coordinates
    if (no part of the polygon falls within the cube) {
        skip to next polygon
    }
    load texture into frame buffer
    draw a polygon into the frame buffer textured with the brush image, using the texture
coordinates of the clipped polygon as the vertices and the vertices of the clipped
polygon (projected onto the X-Y plane) as the texture coordinates.
    read new texture from frame buffer
}

```

Results

Figure 8 is an example of the detail that can be added with the 3D paint program. 26 256x256 pixel 24bit-color textures are used to cover this armadillo model, although only a few have been painted for this close-up image of the armadillo's head. The mannequin model shown in the next two images contains 1,355 top level faces and a total of 36,065 triangles. 167 64x64 pixel 24bit-color texture images are being used to cover the surface, with eight faces per texture. Each number on the mannequin's head is one face. All the timing measurements are done on an SGI Indigo² R10000@175MHz with High Impact graphics using debug-build code.



Figure 8. Face shot of Armadillo Man

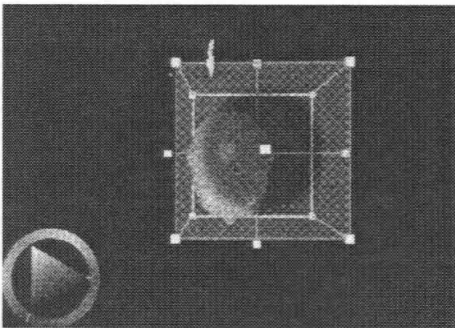


Figure 9. Painting the entire mannequin head

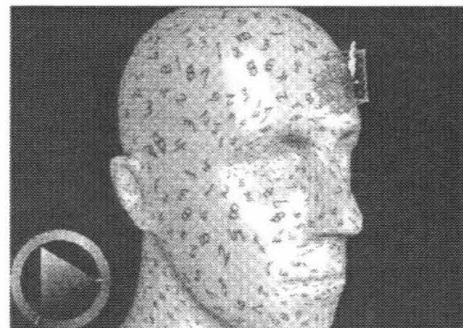


Figure 10. Painting a small dot on the forehead of the mannequin.

Painting the entire model at once (Fig. 9) takes on average, 1.41 seconds. 164 textures are modified, all of the faces and thus all of the triangles are processed, and 14,556 triangles are actually painted. Painting a blue spot onto the mannequin's forehead (Fig. 10) takes on average 0.05 seconds. 11 textures are modified and 16 faces are processed. Of the 201 triangles that are processed, 63 are actually painted.

Discussion

The times listed above show that this algorithm runs at interactive rates even for relatively large models. We have found that screen-redraw times are often more of a problem than painting times.

The user interface that was used for the test paint program is intractable and not suitable for any large painting project. This is not unreasonable for test code, however. The interface was useful for testing how the brush responded to the many degrees of freedom available, and was essentially a poor intermediate between a good 2D and a good 3D interface. There are many straightforward modifications that could be done to make the 2D interface much more usable, such as providing multiple views and smoother mouse control. The ability to make the brush stick to the surface as it was dragged would be of immense help. Similar adjustments would need to be made for a 3D interface.

Conclusions

The painting algorithm presented here is suitable for any polygonal model. Since any smooth surface can be represented as the limit of a series of approximating polygons, the algorithm will work for any surface. Currently, most graphics accelerators only render polygons, so this is not a serious limitation. The algorithm only works when the texture mapping for each polygon is a projective mapping. Other mappings, such as spherical or cylindrical mappings, can be closely approximated using many small polygons each with a projective mapping. Again, this is the way current texture mapping hardware works, so it is not a serious limitation either. Because the brush is projected onto each polygon individually, silhouette edges are handled correctly. A polygon that is facing away from the brush will not be painted, so the brush will never paint around edges. It is superior in these ways to point-sampling painting algorithms.

This algorithm is also well suited for use with fully 3D computer interfaces. It has no dependence on the location of the viewer like the projection algorithm has. The brush has great freedom of movement, unlike the cut-and-paste algorithm. The brush would be an appropriate widget to have at the tip of a 6-degree-of-freedom stylus. In fact, we hope to demonstrate the advantages of this algorithm by developing a program so that an artist may use Caltech's Responsive Workbench to paint models using a truly 3D interface.

One important avenue for further research is to determine how to efficiently generate and use occlusion information during the painting process. Setting the depth limit of the brush is non-intuitive for first-time users. Occlusion effects are important for realistic painting.

Acknowledgments

We wish to thank Jim Barry and Cici Koenig for their advice and patience in testing the paint program.

Bibliography

1. Pat Hanrahan and Paul E. Haeberli. Direct WYSIWYG Painting and Texturing on 3D Shapes. In Forest Baskett, editor, *Computer Graphics (SIGGRAPH '90 Proceedings)*, volume 24, pages 215-223, August 1990.
2. Hans K. Pederson. Decorating Implicit Surfaces. In Robert Cook, editor, *Proceedings of SIGGRAPH '95 (Los Angeles, California, August 6-11, 1995)*, Computer Graphics Proceedings, Annual Conference Series, pages 291-300. ACM SIGGRAPH, ACM Press, August 1995.
3. Hans K. Pederson. A Framework for Interactive Texturing on Curved Surfaces. In *Proceedings of SIGGRAPH 1996*, pages 295-301.
4. Denis Zorin, Peter Schröder, and Wim Sweldens. Interactive Multiresolution Mesh Editing. In *Proceedings of SIGGRAPH '97*, pages 259-268.
5. Mike M. Chow. A Scaleable System for Interactive Painting of Complex Surfaces. <http://graphics.lcs.mit.edu/~mchow/paintings/mp-intro.html>. In preparation, July 1997.
6. Richard Szeliski and Heung-Yeung Shum. Creating Full View Panoramic Image Mosaics and Environment Maps. In *Proceedings of SIGGRAPH '97*, pages 251-258.
7. Alan Watt. *3D Computer Graphics*. Addison-Wesley, 1993.
8. Paul Haeberli. The SGI Image File Format. <http://reality.sgi.com/grafica/sgiimage.html>.
9. OpenGL Architecture Review Board. *OpenGL Reference Manual*. Addison-Wesley, 1992.
10. OpenGL Architecture Review Board; Jackie Neider, Tom Davis, Mason Woo. *OpenGL Programming Guide*. Addison-Wesley, 1993.
11. Perlin, K. An Image Synthesizer. In *Proceedings of SIGGRAPH 1985*, pages 287-296.

Research on Short Frame Turbo Code

Alwin Y. Chi and Robert J. McEliece

Turbo-codes, first introduced by C. Berrou, A. Glavieux and P. Thitimajshima in 1993 [1], achieve significantly better performance than most conventional coding methods. However, as this topic is rather new, many aspects of turbo-codes are still unexplored. In this research, the performance of short-frame turbo-codes in a wireless environment is investigated. The wireless channel is modeled as an Additive White Gaussian Noise (AWGN) channel. Different interleaver structures for short block length are tested and rated based on the weight distribution of the code and Bit Error Rate (BER) at different bit energy to spectral noise density ratio (E_b/N_0).

Among the decoding algorithms for turbo-codes, Soft Output Viterbi Algorithm (SOVA) is one of the most popular since it has good performance and is easy to implement. However, its performance at short block length drops considerably. With a view to improve the decoding performance under such conditions, simple modifications to the SOVA decoder are also attempted in this project.

Introduction

In digital communications, we seek to transmit binary data over a channel at high bit rate. Due to noise interference, the received signals would not be an exact replica of the transmitted signals, resulting in errors. To enable more accurate transmission of data, the information bits are usually encoded before being sent over channel, and depending on the encoding method, channel type and decoding algorithm, the Bit Error Rate (BER) can be lowered.

In 1993, a new class of error correcting codes known as *turbo-codes* is first introduced in [1] with 'near Shannon limit error correction performance' on Gaussian channels. The structure of a turbo encoder is given in Fig. 1. The turbo encoder consists of two identical parallel concatenated Recursive Systematic Convolutional (RSC) encoders, with constraint length $K = 5$, generator polynomial (37,21) and rate 1/3. The code rate can be adjusted by puncturing the outputs. Both encoders use the same bit stream U but with a different ordering created by an interleaver. The interleaver scrambles low-weight input bit streams to generate high-weight codewords, and is vital for the performance of turbo-codes. However, the exact effect of different interleaver structures is not known. In order to understand more about their effects, several interleaver structures are studied in this research.

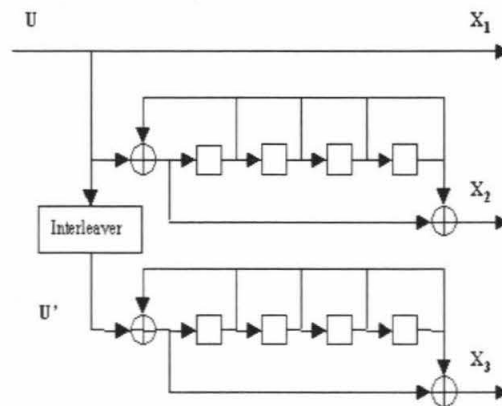


Figure 1. Turbo Encoder, constraint length = 5

Due to the code structure, it is unfeasible to implement the optimal decoding algorithm for turbo-codes, and its performance is strongly dependent on the sub-optimal decoding algorithm used. The standard turbo code decoder structure is given at Fig. 2. It is made up of two decoders which provide soft decision information, usually the bit-wise log-likelihood ratio.

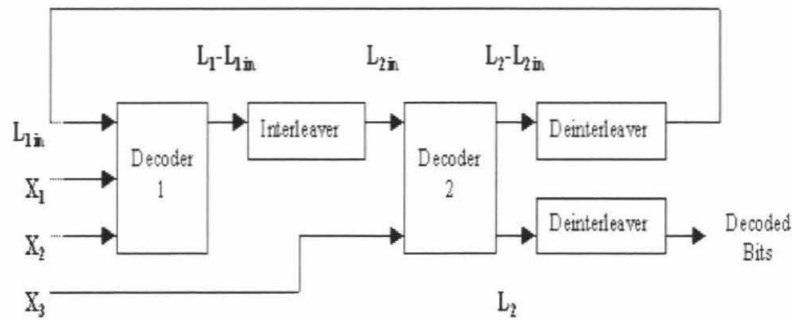


Figure 2. Iterative Turbo Code Decoder

This information would then be supplied to the other decoder as “extrinsic information” to improve the decoder performance through iterations. Among the various soft-decoding algorithms, Soft-Output Viterbi Algorithm (SOVA) suggested in [2] can give reasonably good performance with comparatively easy hardware implementation, making it a promising candidate for practical research. To improve this decoding scheme without greatly increasing decoder complexity, some modifications to the SOVA decoder are also suggested in this research.

Materials and Methods

To investigate the performance of Turbo Code, the system model (as shown in Fig. 3) is broken down into three parts: encoder, channel and decoder. These components were simulated using Matlab to find out the BER of a particular system under consideration at different E_b/N_0 .

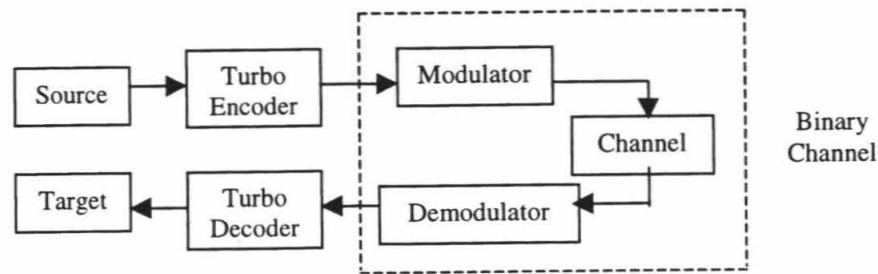


Figure 3. Turbo Code system model

1. The encoder is treated to be outputting at Binary Phase-Shift Keying (BPSK), outputting $+A$ and $-A$ for bit value of 1 and 0 respectively, where A is the amplitude of the signal.
2. The binary channel is modeled as an Additive White Gaussian Noise (AWGN) channel. It adds a zero-mean normal random variable to the signal input from the encoder. The variance of this noise is dictated by the E_b/N_0 ratio.
3. The decoder is constructed using SOVA decoder components.

The simulation is carried out using pseudo-random 32-bit streams as input sequence at the encoder, and is continued for a sufficient number of trials until at least 100 errors are made by the decoder, so as to ensure the BER calculated from the data is over 95% confident.

Simulation Results and Discussion

Since bit reliability values are updated as the SOVA decoder traces through the trellis, the number of updates essentially depends on the position of the bit in a frame. In general, reliability of bits at the beginning of a frame tends to be updated more often, and reliability values of bits towards the end of a frame are not adequately updated. As the updating process always lessens the reliability values, we would expect these insufficiently updated reliability values to be higher than they should. This over-optimistic estimation of bit reliability can adversely affect code performance. Following this analysis, we would expect better code performance if we limit the bit reliability values under a certain threshold in the early iterations, where most improvement is coming from.

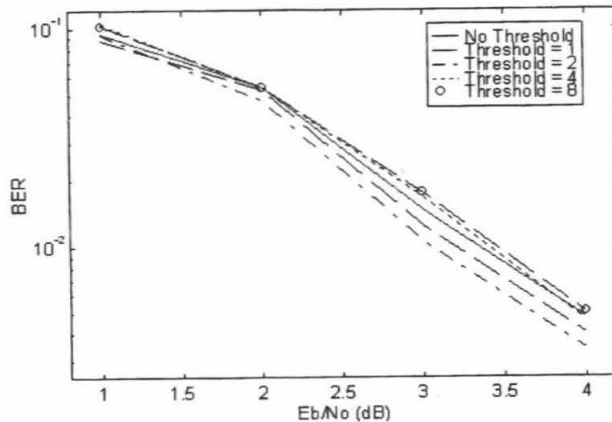


Figure 4. BER vs. E_b/N_0 after 4 iterations with different threshold reliability
16-state code, 32-bit frame, traditional block interleaver

From our simulation results, a threshold reliability of 2 gives the optimal results when E_b/N_0 is between 2.0 and 4.0 dB. This improvement is particularly obvious at high E_b/N_0 , when the original curve without threshold starts to flatten out. At this region setting the threshold to 2 can achieve a gain of 0.5 dB. However, when the threshold is set at 4 and 8, the BER curve overlaps the one without threshold.

Selecting an appropriate threshold is not easy; if the threshold chosen is too small, the decoder cannot distinguish the relative reliability of different bits, and this would reduce the improvement attained from imposing the threshold, or possibly worsen the code performance. On the other hand, if the threshold chosen is too large, most of the reliability values would not reach the threshold and it would have little impact on the code performance.

In a Traditional Block Interleaver (TBI), data is formatted into a m -by- n block array, written in row-wise and read out column-wise. An example write-in and read-out pattern for a 4 by 2 TBI is given in Fig. 5.



Figure 5. Write-in (left) and read-out (right) pattern for 4 x 2 traditional block interleaver

The major defect of TBI is that the last bit of the input stream remains at the end of the output frame. As bits towards the end of a frame tend to give higher reliability values due to insufficient update, their reliability would be over-estimated, no matter before or after interleaving. Consequently, iterative SOVA-based decoding cannot reduce the error probability of those bits near the end of a frame, worsening the overall code performance.

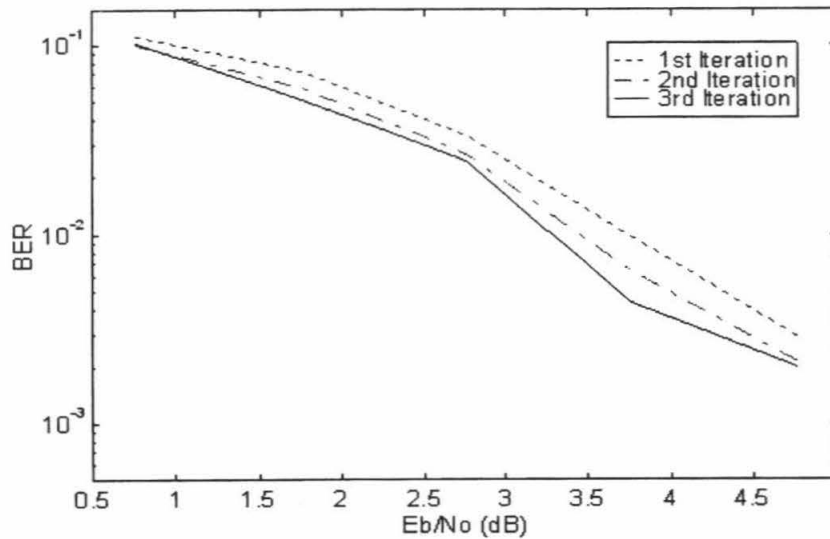


Figure 6. BER vs. E_b/N_0 from iteration 1 to 3 16-state code, 32-bit frame, traditional block interleaver

In Fig. 6 we noticed that although bit error rate drops with increasing E_b/N_0 , the improvement decreases as E_b/N_0 increases beyond 3.5dB, as shown by the flattening curve towards higher E_b/N_0 . This occurrence is very similar to the flattening observed in [3]. This is in line with our analysis; at higher E_b/N_0 , the high error probability of the last bit poses a limit on the code performance. Increasing the number of iterations has a limited effect on reducing this error, as shown by the apparent convergence of the two curves for 2 and 3 iterations at high E_b/N_0 . Since this flattening on the performance curve is caused by the lack of update on reliability values of the bits at the end of a data frame, we call this phenomenon 'tail effect'.

From our analysis on TBI, we would expect an improvement in code performance if we design an interleaver that maps the bits at the end of a frame to the beginning. To verify this hypothesis, we propose a new interleaver which simply inverts the bit order as shown in Fig. 8. As this interleaver inverts the bit ordering, we shall name it Inversion Interleaver (II). This interleaver should remove the tail effect present when TBI is used.

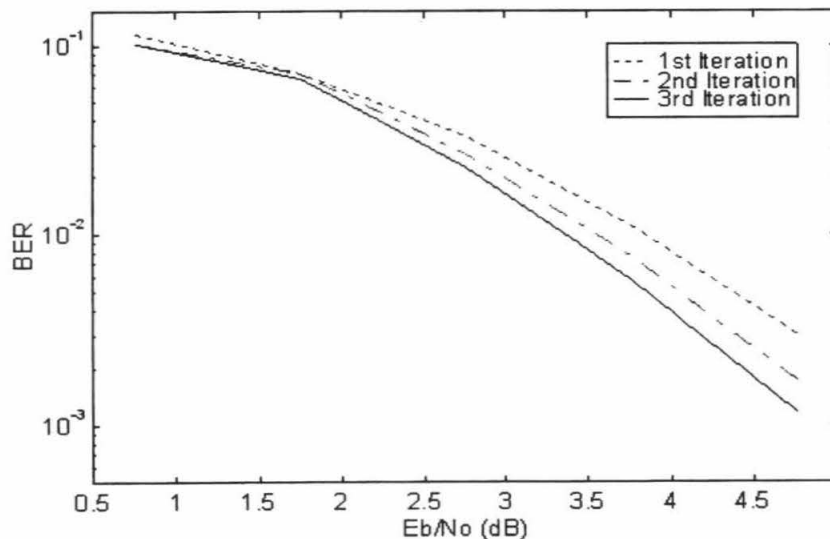


Figure 7. BER vs. E_b/N_0 from iteration 1 to 3 16-state code, 32-bit frame, inversion

1	2	3	4
5	6	7	8

8	7	6	5
4	3	2	1

Figure 8. Write-in (left) and read-out (right) pattern of inversion interleaver

From the BER graph of II and TBI we can see that there is almost no difference in code performance at the first iteration. And in fact, for E_b/N_0 less than 2.5dB, II is slightly inferior to TBI after 2 and 3 iterations. However, when E_b/N_0 increases beyond 4.0dB, the improvement of II becomes apparent. At this region the TBI curves begin to flatten out, while the II curves continue to drop with little flattening.

Inverting the input stream removes the ‘tail effect’ affecting the performance of TBI, however, it fails to reduce the correlation between neighboring bits. When an error is made in judging the value of a certain bit, this error would in turn affect the judgement of its neighbors when the soft reliability values are passed on in further decoding. Therefore a bit contaminated by a noise of loud amplitude would subsequently bias the judgement of the bits before and after it, and iterative decoding cannot correct these ‘bursts’ of error. This analysis is supported by the simulation results: at low E_b/N_0 (noisier channel) the performance of II is not as good as that of TBI, but at high E_b/N_0 (less noise contamination) this effect is not as dominant and II performs better than TBI without the tail effect. As this effect is caused by the correlation between the bits, we shall name it ‘correlation effect’.

From the analysis, we would predict that a good interleaver should achieve two goals: it must avoid the ‘tail effect’ in TBI and reduce the ‘correlation effect’ in II. To satisfy both conditions we propose a new block interleaver. The write-in and read-out pattern of this new block interleaver is given in Fig. 9.

1	2	5	6
3	4	7	8

7	5	3	1
8	6	4	2

Figure 9. Write-in (left) and read-out (right) pattern of new block interleaver

Here, we organize the input pattern into two square blocks, swap the squares and rotate them clockwise by 90° to obtain the read-out pattern. After this operation all the bits originally at the end of a data frame are moved to the front, and their ordering are adequately shuffled by the sub-block rotation. Due to this interleaver structure, we shall call this interleaver Swap-Rotated Block Interleaver (SRBI).

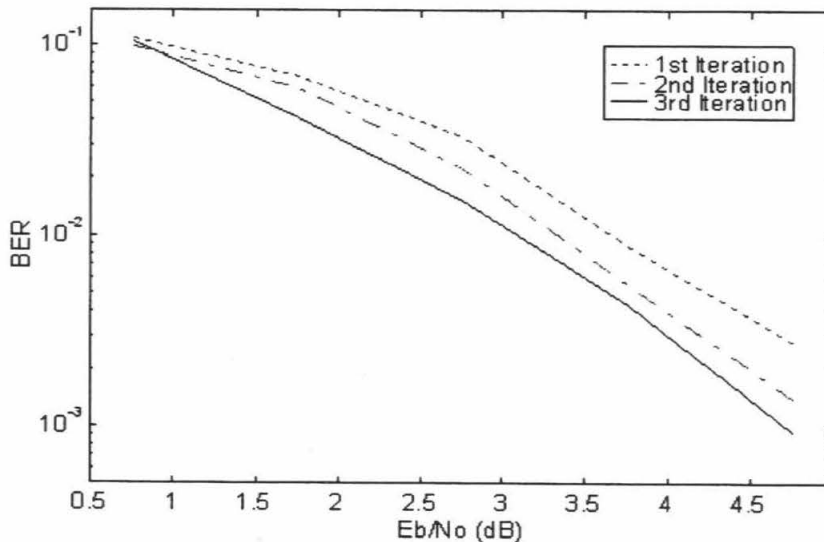


Figure 10. BER vs. E_b/N_0 from iteration 1 to 3
16-state code, 32-bit frame,
swap-rotated block interleaver

In Fig. 10, the simulation results using a TBI and SRBI are given. After the first iteration the results using different interleaver are approximately the same, but on further iterations the difference becomes obvious. After three iterations turbo-code using SRBI performs significantly better than TBI, achieving a gain of 0.5dB compared to TBI at a BER of 10^{-2} . When E/N reaches 4.0dB, the TBI curve start to flatten out and hit the error floor due to the tail effect, but the SRBI curve continues to drop without significant flattening.

Comparing the performance using three different interleavers, we find that SRBI achieve the best performance, over the range of E/N simulated. This confirms our analysis on designing an efficient interleaver: it must minimize the tail effect and correlation effect.

Conclusion

We simulated the turbo code transmission using the standard turbo code encoder and SOVA decoding algorithm. Analyzing the updating rule of SOVA decoder we predict that bits at the end of a data frame may not be updated sufficiently and hence can have over-optimistic reliability values. In order to improve decoding performance without greatly increasing the hardware requirement, we propose to set a limit on the reliability value by a threshold value to cope with the overestimated reliability. From simulation, this method can effectively reduce the BER when rate 1/3 turbo code with constraint length 5 and 32-bit frame is used with traditional block interleaver.

Noting the flattening performance curve using a traditional block interleaver at high E/N , we suggested the tail effect as a critical limitation to the code performance. With a view to eliminate the tail effect, we propose the inversion interleaver and swap-rotated block interleaver as substitutes. From the simulation results it is found that the latter is superior to both the inversion interleaver and the traditional block interleaver. We therefore concluded two criterions in interleaver design: to minimize tail effect and correlation effect.

Acknowledgments

I would like to express my heartfelt gratitude to my faculty mentor, Professor Robert J. McEliece and my co-mentor at Hong Kong University of Science and Technology, Professor Tzs-Mei Ko, for their encouragement, advice and support. Without their assistance this research would not have been possible.

Special thanks to the Summer Undergraduate Research Fellowship (SURF) of California Institute of Technology for the financial support for this research.

Reference

1. C. Berrou, A. Glavieux and P. Thitimajshima, "Near Shannon Limit Error-Correcting Coding and Decoding: Turbo-Codes(1)", Proc. of ICC'93, pp. 1064-1070, 1993
2. J. Hagenauer and P. Hoehner, "A Viterbi Algorithm with Soft-Decision Outputs and its Applications", Proc. Of IEEE'89, pp. 1680-1686, 1989
3. J. Hagenauer and P. Robertson, "Iterative ("Turbo") Decoding of Systematic Convolutional Codes with the MAP and SOVA Algorithms", ITG-Fachberichte, v. 130, pp.21-29, 1995

High Efficiency Class-E Power Amplifiers

Teo Der-Stepanians and David B. Rutledge

Existing, conventional high-frequency (HF) power amplifiers often rely on either vacuum tubes or large power transistors to amplify signals. As a result, they are themselves very large and expensive. A new HF, high-efficiency, class-E, radio power amplifier has recently been developed at Caltech that overcomes both of these limitations.

This amplifier operates on the 30-meter (10 MHz) band, and is designed with an output power of 200 watts. It is based around the International Rectifier IRFP440 MOSFET, which is a device commonly used in switching power supplies and costs under \$10. We were able to use such a relatively inexpensive, low-power device because of the high efficiency characteristic of the class-E amplifier, typically around 90%. The high efficiency makes the power dissipated in the switching device small enough to allow operation even without a cooling fan. The 30-meter amplifier requires only 3 to 8 watts of drive power for reliable, efficient operation. We used a modified NorCal-40A low-power radio transceiver to supply this drive.

This new amplifier is a continuation of work done at Caltech by undergraduate and graduate students over the past three years. Last year, a pair of amplifiers was developed specifically for hams operating on the 40-meter band. These amplifiers had output powers of 300 watts and 500 watts. A paper about these amplifiers was published in QST Magazine [1]. Collections of parts were assembled and sold to people who wanted to try building the amplifiers. It was found that there was much interest in amplifiers for other bands. This led to the work done this summer and the development of the new 30-meter, 200W amplifier. Like its predecessors, this new amplifier is easy to build, costs about the same, and has most of the same characteristics and limitations.

Background

It is often necessary to amplify weak signals to make them more useful, and there are different methods for carrying out this amplification. Most conventional amplifiers fall into one of the three classes A, B, or C. Each class of amplifier has advantages and disadvantages which make it more suitable in certain situations. The following is a short description of each of these classes:

Class-A: These amplifiers use a single transistor which is always active. An active transistor has considerable amounts of voltage across and current through it. The product of the voltage across the transistor and current through it translates into heat dissipated in the transistor. For this reason, the efficiency of class-A amplifiers is limited to about 30%. However, class-A amplifiers introduce very little distortion in the amplification process. The output of a class-A amplifier looks almost exactly like its input, only larger in amplitude.

Class-B: Class-B builds on Class-A by having two transistors, which take turns amplifying the input signal. One transistor usually handles the positive half of the output, and the other the negative. This way, only one transistor is active at any given time, while the other is off. This doubles the efficiency to around 60%, at the cost of small amounts of distortion at the signal crossover, where one transistor turns off and the other takes over the amplification.

Class-C: The class-C amplifier is known as a switching amplifier. In traditional class-C amplifiers, the switching device is active less than half of the time, making it even more efficient. In modern, transistor-based class-C amplifiers, the transistor often acts like a switch, either completely on or completely off. When on, a large current flows through the transistor, but the voltage across it is small. When off, voltage builds across the transistor, but the current through it falls nearly to zero. This way, there is very little overlap between voltage and current in the transistor, which translates into much less power being wasted in the device, and a higher efficiency. Class-C amplifiers normally have efficiencies reaching 75%-80%. Most of the loss in a class-C amplifier occurs during the actual switching. The transistor does not switch from on to off (or vice versa) instantaneously. As the transistor switches, it goes through an active region, where it has both a current through it and voltage across it. This translates into power wasted as heat in the transistor every time it is switched, and this wasted power increases as the frequency of operation is increased. A disadvantage of the class-C amplifier is that because of its switching mechanism for amplifying signals, it is not linear at all. The output may look nothing like the input. It will be at the same frequency, though with a great deal of harmonic distortion.

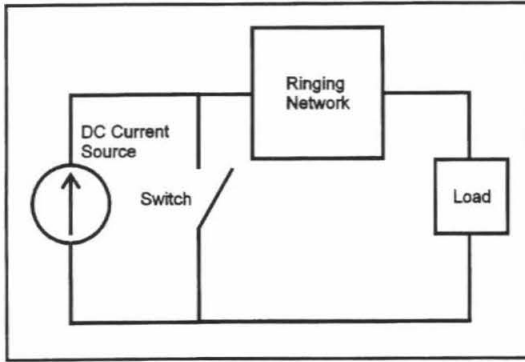


Figure 1. Block diagram of class-E amplifier

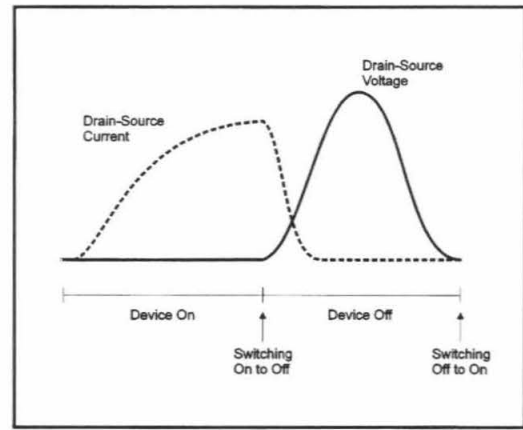


Figure 2. Ideal class-E waveforms

Class-E

The Caltech power amplifiers rely on a less well known class of operation, class-E. The class-E amplifier design was first explored in 1964 by Gerald Ewing [2] and later by Nathan and Alan Sokal in 1975 [3], who patented it. The use of class-E amplifiers in high-frequency amateur radio transmitters prior to the Caltech designs is unreported. An idealized diagram of a class-E amplifier is shown in Figure 1. It consists simply of a DC current source feeding a switch (transistor), followed by a ringing network and the load. A class-E amplifier is very similar to the class-C amplifiers. However, a class-E amplifier achieves even higher efficiency (typically around 90%) by minimizing the current-voltage overlap which occurs during switching in a class-C amplifier. This is done by the addition of the ringing network following the switching device. With the ringing network in place, the voltage across the transistor rises smoothly from 0 to a maximum, and falls smoothly back to zero just before the transistor switches on again. A complete cycle of the class-E switching amplifier can be broken down into the following four phases (see Figure 2):

Transistor On (switch closed): Transistor conducts current through itself to the ground. The voltage across the transistor is very small, keeping power dissipation in the device low.

Transistor Switching On to Off (switch opening): Voltage across transistor rises smoothly as current is redirected from the device into the resonant load network. While the switching is occurring, power dissipation is kept low because the voltage across the device rises slowly and remains small during the short switching period.

Transistor Off (switch open): Voltage rises smoothly to a maximum, then falls smoothly back to zero.

Transistor Switching Off to On (switch closing): Since there's near-zero voltage across the transistor, little power is wasted as current is again directed into the device instead of the load network.

In this way, the class-E amplifier achieves efficiencies of around 90%, which allows us to operate with a relatively small, inexpensive transistor. Power dissipated in the transistor is small enough that heat can be removed with a simple heat-sink. No fan is required for low duty cycle use. Because of the relationship between efficiency, dissipated power, and output power, an amplifier running at 90% efficiency can output 21 times more power (at a given dissipation level) than a 30% efficient amplifier [4]. However, there are some disadvantages to the class-E design. The amplifier must be driven with enough power to reliably switch the transistor on and off. The gates of the MOSFET's are capacitive and present a low impedance at high frequencies. The drive must be powerful enough to switch the transistor on and off quickly and completely. If the transistor is not switched on and off reliably, or if it is switched too slowly, inefficient operation results which can cause a buildup of heat in the transistor, leading to its failure. The class-E amplifier is completely non-linear, and its operation is limited to a single band by the ringing circuit on its output. The power output of the amplifier (assuming it is driven properly) depends almost exclusively on the DC supply voltage. This makes it unsuitable for use

in AM or SSB transmitters. However, it works very well in CW, FM, and FSK applications, where information is transmitted either by turning a carrier on and off completely (CW) or by changing the frequency, not amplitude, of the carrier by small amounts (FM, FSK).

The 30-Meter Amplifier

The newly developed 30-meter, 200W amplifier is very similar in design to the existing 40-meter amplifiers. For the most part, only the component values were changed to operate at the higher frequency. See Figure 3 for a circuit diagram of the amplifier, and Appendix 1 for a more detailed description of the components used. Components L1 and T1 match the input of the transistor to the output of the driving transceiver. The impedance of the gate of the MOSFET is low and mostly capacitive (though there is a small parasitic resistive component, as well). The transformer matches this low impedance to the nominal 50Ω impedance of the driver. The variable inductor L1 is tuned to cancel the capacitance of the gate at the operating frequency. The input SWR is typically below 1.4. Capacitor C1 is a high frequency bypass of L1 to reduce VHF ringing.

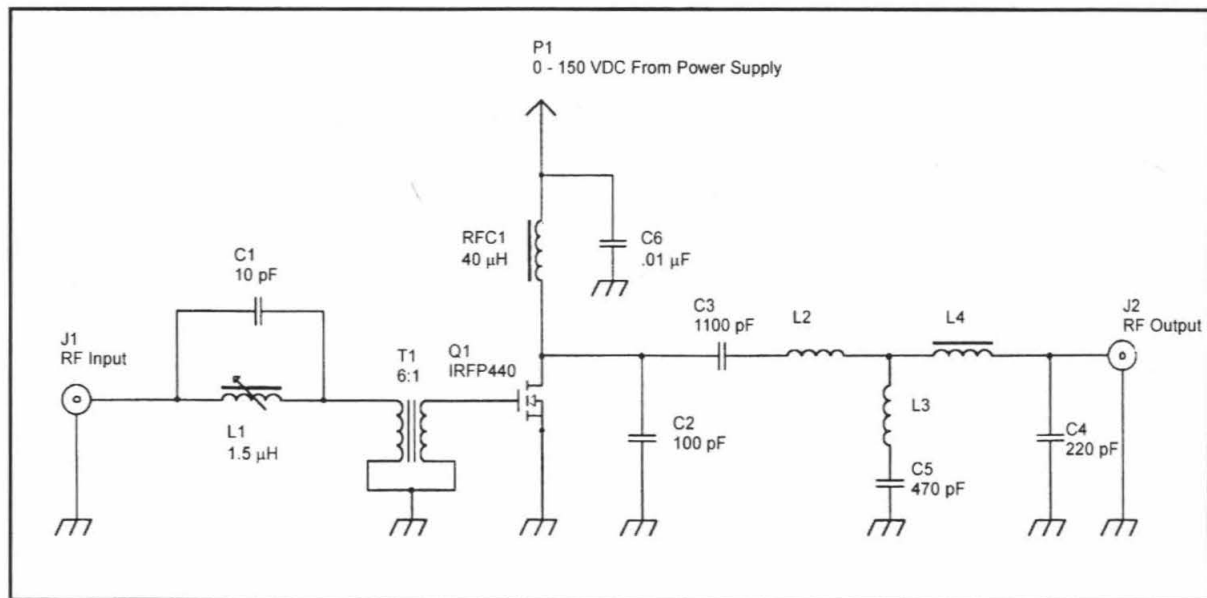


Figure 3. Circuit diagram of 30-meter, 200W amplifier

The function of RFC1 is to convert the 0-150 VDC from the power supply into a current source. RFC1 also helps, in conjunction with C6, to keep RF voltages away from the power supply. C3 and L2 form the main resonant circuit. They cause the voltage at the drain to rise smoothly to a maximum and return to zero before the transistor turns on again. C5 and L3 serve two purposes. The first is to form a notch filter for the second harmonic. Together, C5 and L3 resonate at twice the operating frequency (around 20 MHz) and therefore provide a direct path to ground for the second harmonic. Their second function is to transform the 50Ω impedance of the antenna down to around 10Ω, a better match for the transistor in this type of circuit.

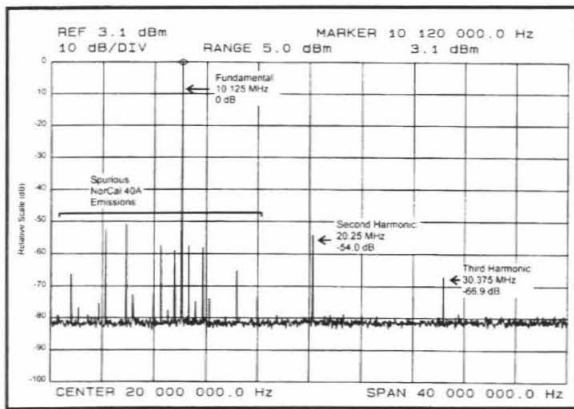


Figure 4. HF spectrum of 30-meter amplifier driven with modified NorCal 40A transceiver

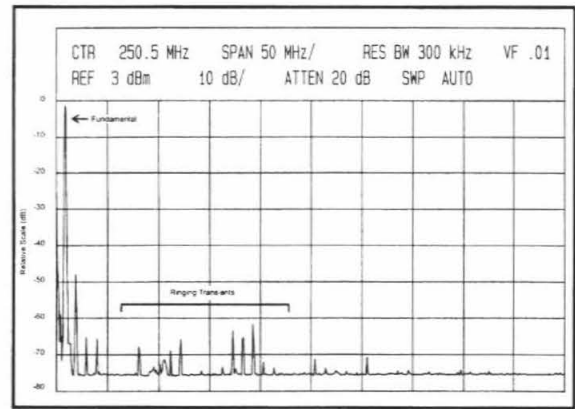


Figure 5. VHF spectrum of 30-meter amplifier driven with modified NorCal 40A transceiver

C4 and L4 form a low-pass filter. They ensure that all of the harmonics fall well below -40dB of the carrier, the limit set by the FCC. Figures 4 and 5 are the HF and VHF spectra of the amplifier's output, respectively. These spectra were taken with the amplifier output set to 204W. The driver was a modified NorCal 40A transceiver, which will be discussed in the next section. The drive level was 4.78W. Figure 6 shows a picture of the MOSFET gate and drain waveforms.

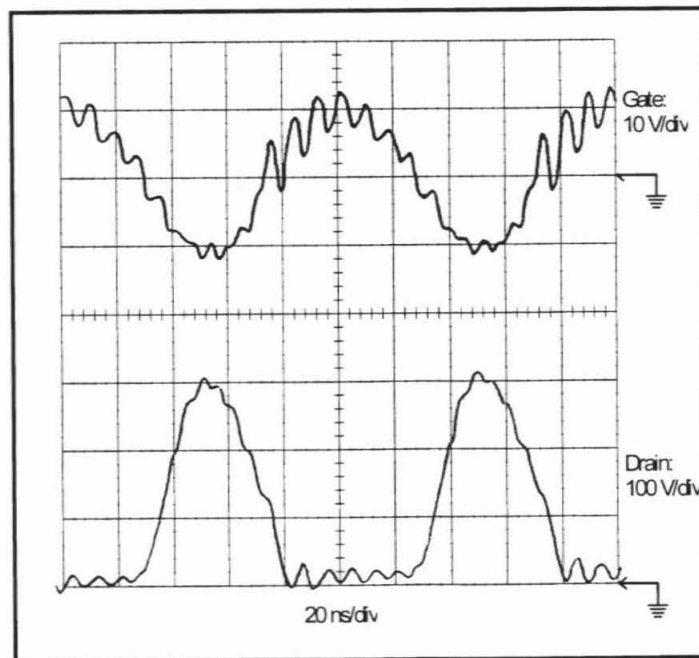


Figure 6. Gate (top) and drain (bottom) waveforms of 30-meter amplifier, being driven at 4.78W with a modified NorCal 40A transceiver. The output power is 204W. The gate is at 10 V/div, and the drain at 100 V/div. The time scale is 20 ns/div. Note the ringing on both waveforms.

The 30-meter amplifier requires from 3 to 8 watts of drive power for optimal operation. See Figure 7 for a plot of efficiency vs. drive power. We have noticed problems with keying the amplifier at levels below approximately 4 watts, so drive powers exceeding this amount are recommended. The drain efficiency is found by dividing the output RF power by the input DC power. A better indicator of how much power is being dissipated in the transistor, however, is the total efficiency. The total efficiency is defined as the RF output power divided by the sum of the input DC power and RF drive power. As can be seen from Figure 7, though the drain efficiency continues to increase, the total efficiency drops for

drive powers above approximately 8 watts. This happens because the drive power does not couple to the output, but is dissipated in the transistor as heat. Therefore, once the drive power is high enough that the transistor is switching optimally, further increasing the drive power only increases the amount of power dissipated in the transistor, and does not benefit the total efficiency of the amplifier.

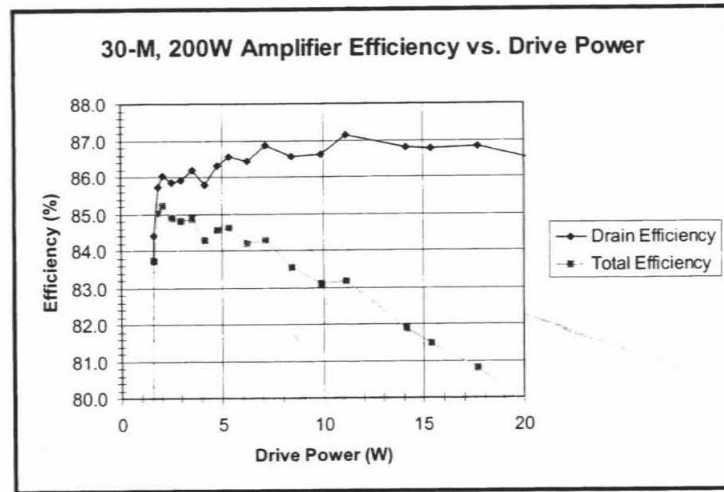


Figure 7. Efficiency vs. drive power for 30-meter amplifier

An interesting feature of this amplifier, which it shares with the existing 40-meter amplifiers, is the way in which signals couple backwards from the output to the input. When the supply voltage is at 0 volts (this occurs during reception), there is a large capacitance between the gate and drain of the transistor. Therefore, in-band signals couple backwards through the amplifier, including the transistor, with a measured loss of only 8.5dB. Because of the high sensitivity of the modified NorCal 40A driver (we measured its MDS to be -133dBm), even with this 8.5dB of attenuation placed before the antenna, the transceiver is still limited by atmospheric noise. This way, no additional transmit/receive switch circuitry is required for the amplifier. The amplifier operates nearly transparently with the driving transceiver.

The Norcal 40A Modifications

Because the 30-meter amplifier was aimed at an audience of amateur radio operators, one of our goals was to find a suitable transceiver for driving the amplifier that would be commonly available to hams. We tried using a modified NorCal 40A (NC40A) as the driver. The NC40A is a 40-meter (7 MHz) transceiver. However, Ed Burke outlines a way of modifying the NC40A to change its operating frequency from 7 MHz to 10 MHz [5]. At the heart of this modification is the changing of the IF from 5 MHz to 8 MHz. Both the original and modified NC40A's have a local oscillator at 2 MHz. In the original, 2 MHz is mixed with 5 MHz to give the operating frequency of 7 MHz. In the modified NC40A, 2 MHz is mixed with 8 MHz, and the resulting radio works at 10 MHz.

The modified NC40A, though functional on the 30-meter band, suffered some losses in performance. The level of the minimum discernible signal (MDS) went from -132dBm to -126dBm and the gain from 104dB to 96dB. To solve these problems, certain component values were changed, bringing the gain and sensitivity of the modified NC40A back close to their original values. In our NC40A's, the sensitivity after the modifications was -133dBm, and the gain was 102dB. To increase the output power of the NC40A (which was measured to be 1.4W after the modifications - down from 2.5W before), we lower the impedance of the low-pass filter, increasing the current drawn and therefore the power from the power amplifier. The values for these components were determined through computer simulations of the low-pass filter using PUFF [6]. The output powers of the two NC40A's that we modified were increased to 5.5W and 6.5W, making the modified NC40A perfect for driving the amplifier.

Diplexers

To keep spurious emissions from the NorCal 40A driver and the 30-meter amplifier low, two diplexers were built. A diplexer is a band-pass filter which has an impedance of 50W at all frequencies,

terminating out-of-band spurious emissions in a 50W dummy load [7]. The smaller of our two diplexers, designed to handle low powers, is placed between the NorCal 40A driver and the power amplifier. This diplexer ensures that the power amplifier is driven with a clean signal at the correct frequency. It attenuates the spurious emissions from the driver which would otherwise be amplified by the power amplifier. The larger, high power diplexer is placed after the output of the power amplifier, and helps in attenuating spurious emissions generated by the power amplifier. Figure 8 shows a block diagram of the complete 30-meter CW radio station.

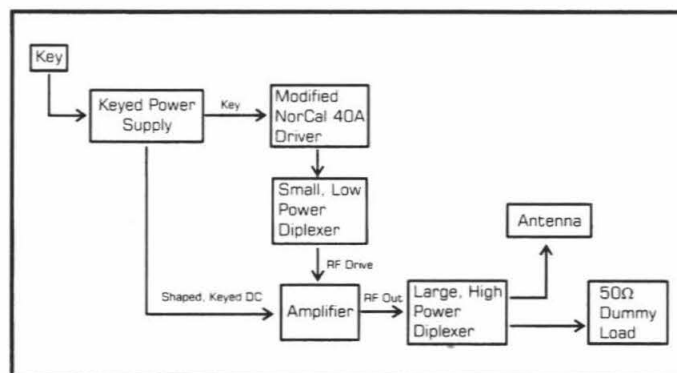


Figure 8. Block diagram showing complete 30-meter CW radio station

Future Work

There is still much room for improvement on these class-E power amplifiers. One possibility is a built in pre-amp, which would allow the amplifiers to be driven with smaller amounts of power, allowing their use with low power (QRP) transceivers without modification. Another useful addition would be a transmit/receive (TR) switch of some sort, which would allow for better reception by allowing incoming signals to bypass the amplifier. A small, switching power supply could be developed to replace the current one, which is very large and expensive. It may even be possible to use the RF drive, perhaps divided in frequency, as an oscillator for such a power supply. Finally, it would be interesting to develop class-E amplifiers for other bands and higher powers. Work is already underway for developing a 15-meter class-E amplifier.

Acknowledgements

This summer's work was done under a Caltech Summer Undergraduate Research Fellowship, funded partially by Allied Signal Corporation. The author appreciates the help, guidance, and technical assistance of Dr. David Rutledge, John Davis, and Kent Potter, without whom this work would not have been possible.

References

1. E. Lau, K.-W. Chiu, J. Qin, J.F. Davis, K. Potter, D.B. Rutledge, "High-Efficiency, Class-E Power Amplifiers," Part 1, QST, pp. 39-42, May 1997; Part 2, QST, pp. 39-42, June 1997.
2. G.D. Ewing, "High-Efficiency Radio-Frequency Power Amplifiers," Ph.D. Dissertation. Oregon State University, Corvallis, Oregon, 1964.
3. N.O. Sokal and A.D. Sokal, "Class E - A new class of high-efficiency tuned single-ended switching power amplifiers," IEEE Journal of Solid-State Circuits, Vol. SC-10, pp. 168-176, June 1975.
4. E. Lau, K.-W. Chiu, J. Qin, J.F. Davis, K. Potter, D.B. Rutledge, "High-Efficiency, Class-E Power Amplifiers," Part 1, QST, pp. 39-42, May 1997; Part 2, QST, pp. 39-42, June 1997.
5. E. Burke, "NC40 to N30 Conversion," QRPP, Vol. III, Number 4, p. 63, December 1995.
6. PUFF is a program developed at Caltech for design and simulation of microwave integrated circuits, but is very useful for RF circuits, as well. It is available from Puff Distribution, Department of Electrical Engineering, MS 136-93, Caltech, Pasadena, CA 91125. The cost is \$10. See <http://www.systems.caltech.edu/EE/Faculty/rutledge/puff.html> for more information.
7. D. Newkirk and R. Kariquist, "Mixers, Modulators, and Demodulators," The 1996 ARRL Handbook, Chapter 15, p. 15.22

Methanol Fuel Cell System Design

John F. Christensen and S. R. Narayanan

A steady-state model for the individual methanol fuel cell has been constructed, with the potential for being integrated into an overall system model. Both experimental results and theoretical considerations have been incorporated into the model. Correlations for the flux of methanol across the cell membrane (methanol cross-over) and cell voltage as functions of current density, stack temperature, and air flow rate have been derived, based upon parametric studies of a five cell stack. Calculations of pressure drop in various flow field and manifold configurations provide an estimate of the power requirements for the air compressor, while water removal calculations indicate that a water recovery subsystem may be needed to maintain water balance. Finally, the thermal energy balance determines the liquid flow rate necessary for adequate cooling.

Introduction

Fossil fuels are limited, unrenewable energy sources that may not be around in the decades to come. With their impending depletion, many researchers are looking to alternative methods of energy production to power the planet in the very near future. Batteries are a reasonably environmentally agreeable solution to the energy crisis, but even rechargeable batteries have finite lifetimes and must eventually be discarded. At present, no battery is capable of powering an automobile for a long period of time without recharging.

Fuel cells operate in a similar manner to batteries, but lack the intrinsic flaws of both batteries and fossil fuels. The fuel used in these devices can be stored in a tank and refilled as desired, just as gasoline is used in automobiles today. Thus, the fuel cell has a theoretically unlimited lifetime (neglecting cell degradation, which is slow under the operating conditions discussed here), and can power a machine for as long as is allowed by the size of the tank.

The fuel cells that are being designed and tested at JPL (Figure 1) use methanol mixed with water at the anode and oxygen or air at the cathode, and rely upon proton migration through a semi-permeable membrane (Nafion in this instance) to drive the current. Products are carbon dioxide and water, the latter of which is recycled and used to keep the methanol solution at the desired molarity. Only one carbon dioxide molecule is produced per molecule of methanol, so the process is somewhat cleaner than fossil fuel combustion. Methanol is a relatively cheap, easily transported liquid fuel, and exists in great abundance.

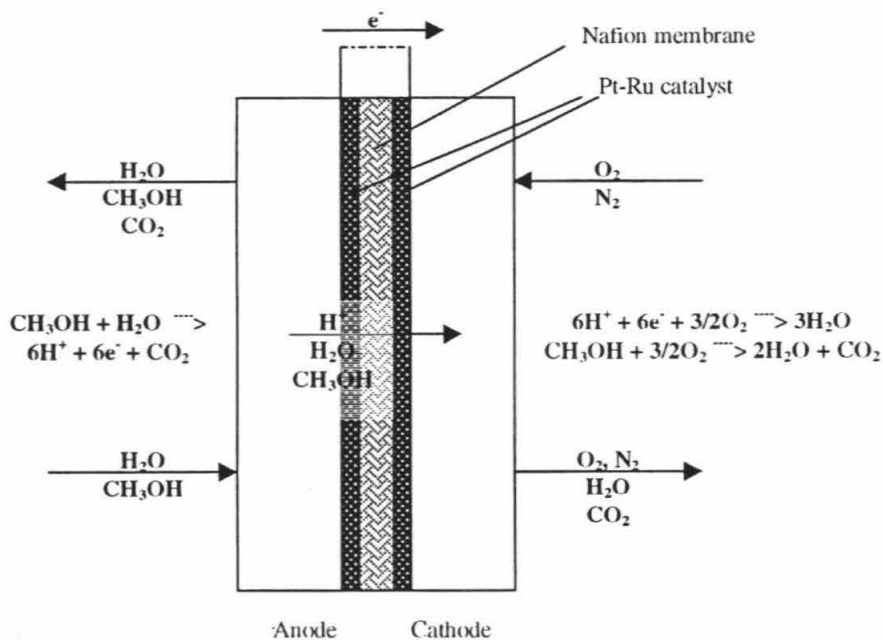


Figure 1. Schematic of the direct liquid feed methanol fuel cell. Methanol and water are supplied to the anode, where they react on a Pt-Ru catalyst layer to form protons, electrons, and carbon dioxide. The protons migrate through the Nafion membrane (along with water and some methanol) and are oxidized at the cathode to form water. Any methanol that permeates through the membrane is assumed to combust completely to form water and carbon dioxide. Electrons are conducted through the catalyst layers and can supply power to an external load. Oxygen or air is supplied to the cathode.

Though the concept of using direct methanol fuel cells as a power source is appealing in its simplicity and theoretical efficiency, tapping the energy contained in methanol and air becomes quite complicated on a systems level. It is desirable to maximize the power delivered by a fuel cell stack (anywhere from 5 to 50 cells linked in series) while maintaining stability and minimizing the size and cost of ancillary components (compressor, pump, condenser, radiators, etc.). Thermal stability is of prime concern among several design issues, since the cell voltage (and thus the power density) is a strong function of temperature. If the temperature of the stack were to fluctuate too greatly, the cells would cease to provide adequate power to run the ancillaries, and the system would fail.

Another major issue in the system's design is water management, as water is necessary for the half-reaction on the anode side, as well as a product on the cathode side. Thus, water must be separated from the cathode waste stream and recycled to the methanol mixing tank. There are several mechanisms for water transport across the membrane during cell operation, including water permeation; electro-osmotic drag, or the migration of water molecules which hydrate the protons crossing the membrane; methanol crossover and combustion, the Nafion membrane being permeable to methanol as well as water; and the Pt-Ru catalyzed reaction of protons with oxygen at the cathode [1]. The overall number of moles of water transported via these mechanisms is determined experimentally so that the amount of water to be recycled can be calculated. Figure 2 illustrates the water transport mechanisms.

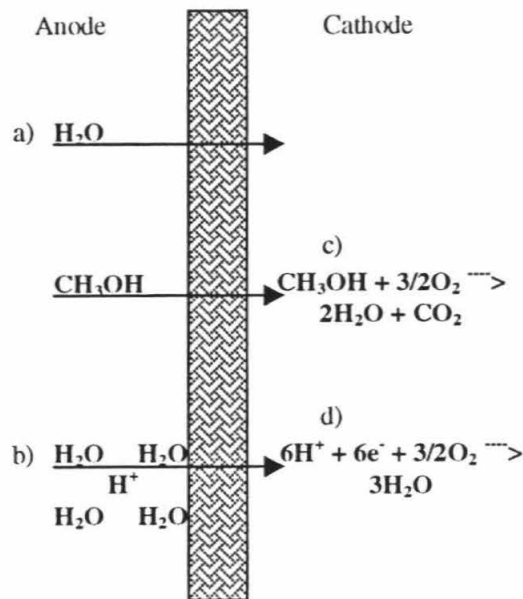


Figure 2. Mechanisms for the transport of water to the cathode. a) Water permeation through the membrane: Nafion is highly permeable to liquid water, which is fed with methanol to the anode. b) Electro-osmotic drag: Proton transfer through the membrane is facilitated by water transport. c) Methanol crossover: Some methanol permeates the membrane and is oxidized to form water at the cathode. d) Proton oxidation: Water is also formed as the product of the cathode half-cell reaction.

A third important problem in system design deals with the design of the cell itself. Each cell is composed of a Nafion membrane, bordered on each side by a layer of catalyst, which in turn is adjacent to a graphite bipolar plate. Each plate is machined with a series of grooves on each side, one being the air flow field for a given cell and the other being the methanol flow field for the adjacent cell. The stack is simply an alternating series of bipolar plates and membranes. There are two major designs for the flow fields used in the fuel cell, one being a cross-hatch of channels and grooves resembling the inside of a waffle iron, and the other containing several parallel serpentine paths which wind back and forth along the length of the plate (Figure 3). The flow field design is most crucial in the calculation of pressure drops on the cathode side of the cell, as these gradients tend to be higher for air than for the methanol-water mixture, and the power requirements for pressurizing the air are therefore greater. The "waffle" design requires a much lower pressure drop than the "serpentine" design, though the latter has certain advantages when water clogging is considered. If there are fewer passages for the transport of air, as in the serpentine design, then it is more likely that plugs of water will be pushed out, permitting utilization of all the available catalyst area.

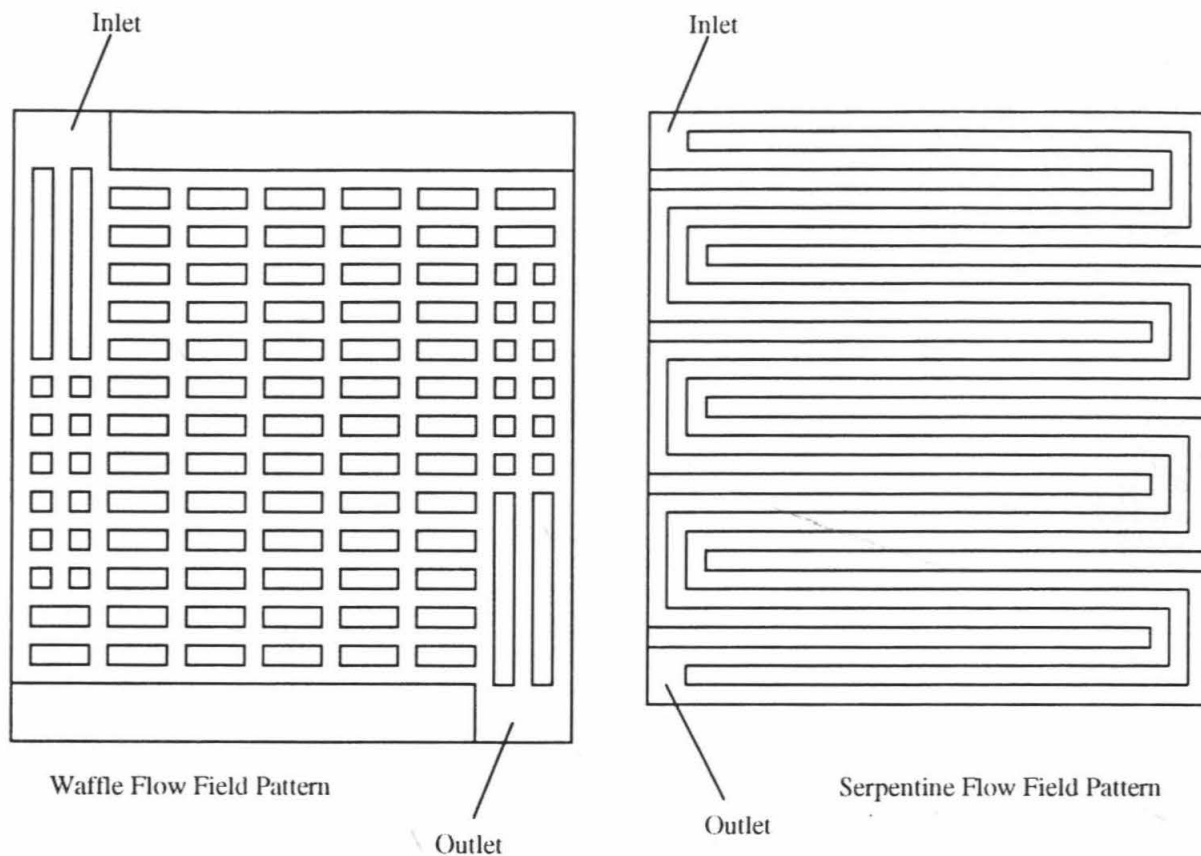


Figure 3. The two flow field designs used in the methanol fuel cells. The “waffle” design has a lower pressure drop between the inlet and outlet, but is more susceptible to water clogging on the cathode side than the serpentine pattern.

Methods

In order to determine the cooling rate required to maintain the stack at a specified temperature, the major heat sources were identified, and the magnitude of their contributions estimated. The two primary heat generation terms in the fuel cell are the power loss due to non-idealities in the cell and combustion of methanol which has passed through the Nafion membrane to the cathode of the cell. Both of these are essentially experimentally determined values, as the operating voltage and extent of methanol crossover have been measured at various stack temperatures, air flow rates, and current densities (an independent variable which can be controlled by the load placed on the stack). Multi-variable polynomial regressions were carried out on the data collected in parametric studies on both the voltage and crossover current (the current related to methanol crossover by Faraday’s law). These experimental fits, though they match the data quite well (within an average of three percent), are valid only in the range of parameters over which data was collected. Therefore, the domain of input available for heat generation calculations is limited by that of the parametric studies.

Mechanisms for heat removal were also evaluated in order to establish the range of parameters necessary for a thermal energy balance in the stack. Under normal operating conditions, the liquid and air streams enter the stack at the ambient temperature and exit at approximately the temperature of the stack. Since the stack temperature is higher than that of its surroundings, both streams will remove heat from the stack. By varying the inlet temperatures of the two streams, one may control the fraction of heat that is rejected. Since the reactant air is typically dry, while the exhaust gases are saturated with water collected at the cathode, energy can also be removed from the system via evaporation and removal of water by the air stream. Thus, varying the relative humidity of the inlet air is another method for maintaining the thermal energy balance. Finally, the rate of heat removal must be directly

proportional to the flow rate of the air and liquid streams, provided equilibrium is established rapidly enough inside the stack.

Water removal itself is another crucial element in system design, and once again it depends upon the flow rate and inlet conditions of the air stream. The amount of water generated through combustion of the crossover methanol and the electrochemical reaction at the cathode was calculated, as was the amount of water carried away by an air stream of a given flow rate and at a specific inlet temperature and relative humidity. Rather than use air flow rate as an independent variable, it is often more convenient and illuminating to base calculations upon the number of stoichs of air that must be passed through the system; that is, the ratio of moles of air pumped into the stack to the stoichiometric number of moles necessary to react completely with the methanol that is utilized. If the air flow rate is defined in terms of stoichs, the ratio of water removed to water generated is independent of the amount of methanol consumed in the cell, and depends only upon inlet relative humidity, the number of stoichs, and the inlet and stack temperatures.

Yet another design issue associated with the air flow through the stack is the dependence of pressure drop upon flow rate. Simplified versions of the waffle design and several serpentine patterns have been modeled and analyzed, following the method employed by Thirumalai and White in their analysis of waffle-pattern flow fields for hydrogen-oxygen fuel cells [2]. The pressure drop-flow rate relationship for rectangular ducts contained in their paper was verified and employed in the set of models. A system of equations, one for each node in the flow field, was represented in matrix form, and the pressure at each node was calculated. Aside from wall friction losses, only the ninety degree turning losses in the serpentine arrangement were considered, incorporated into the system of equations as fluid flow sources and sinks. Bloomfield, et al point out that turning losses have higher drag coefficients than any other possible source of form drag, including expansions, restrictions, inlets, and outlets [3]. Since there are so many turns in the serpentine design compared to other sources of drag, it appears reasonable to ignore other losses.

Results and Discussion

The thermal energy balance calculations illustrate the strong dependence heat and power generation have upon variables such as the stack temperature, current density, and air flow rate through each cell. The cell voltage varies significantly as these parameters are altered, thus imposing a wide range of values upon the total cell area necessary to deliver the desired stack wattage. For a 180 watt stack, with cell areas of 100 cm^2 , the number of cells in the stack must be anywhere from 15 at operating conditions of 290 mA/cm^2 , 363 K , and two liters/min of air, to 177 at 25 mA/cm^2 , 293 K , and 0.4 liter/min . Since the number and area of cells in the stack are fixed once the system is built, the sizing must be matched to the envelope of possible operating conditions.

Other variables such as the inlet temperature and relative humidity of the air stream influence the heat removal capabilities of the system. Cool dry air will remove more heat through evaporation than will warm humid air, and in certain regimes, the air can actually cool the stack, as shown in Figure 4. Cooling occurs when the heat removal rate required of the liquid stream falls below zero watts. In these instances, a recuperator on the cathode side may provide a solution to the cooling problem. Other than the air flow rate, all of the variables associated with the inlet air are dictated by the ambient conditions. A recuperator, which transports water from the cathode exhaust to the inlet air and acts as a heat exchanger, would be a means of altering the inlet temperature and water content to control heat loss through the air stream.

Heat to be removed by liquid stream

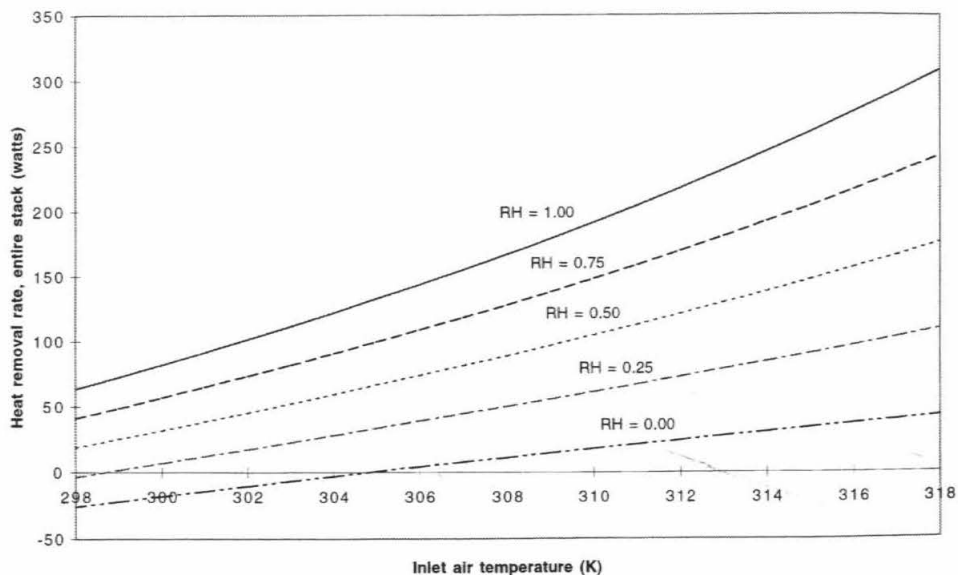


Figure 4. Required heat removal rate as a function of cathode inlet temperature and relative humidity. The stack temperature is 333 K, the current density is 100 mA/cm², and the air flow rate is 2 liter/min per cell.

As the fuel cell stack will be insulated from its surroundings, the liquid stream is responsible for removing the balance of heat generated in the stack. Since water and methanol have such high heat capacities compared to that of air, the temperature of the liquid stream will not increase significantly from entrance to exit. Figure 5 shows the effect of flow rate (per cell) and inlet temperature upon the exit temperature of the liquid stream at a current density of 100 mA/cm², air flow rate of 2 L/min, stack temperature of 333 K, and ambient conditions of 50% relative humidity and 318 K.

Though much of this model focuses upon heat sources and sinks, the balance of water in the system is also critical in maintaining steady state operation. Water is produced via reduction of oxygen and crossover combustion at the cathode and is removed primarily by the air stream as it becomes saturated with water vapor. Figure 6 shows that the fraction of water removed can exceed one even at relatively low flow rates when the inlet air is cool and dry, another indication that a recuperator should be used on the cathode side. An alternative to the recuperator is an air-cooled condenser linked in series with a gas-liquid separator, which would remove water as liquid from the exhaust air (to be vented), and return any necessary make-up water to the methanol mixing tank.

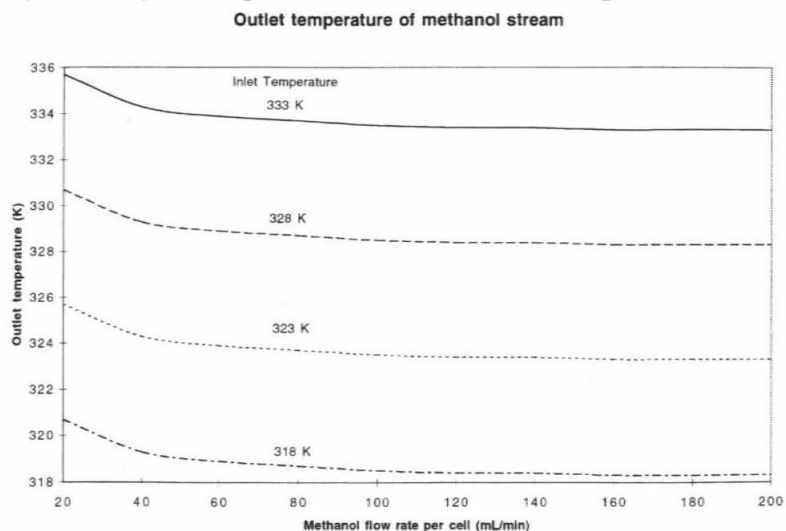


Figure 5. Outlet temperature of methanol stream as a function of methanol flow rate and anode inlet temperature. The stack temperature is 333 K, the operating current density is 100 mA/cm², the air flow rate is 2 liter/min per cell, the ambient temperature is 318 K, and the relative humidity is 0.5.

The data generated from this and other thermal energy models are helpful in sizing ancillaries such as the condenser or recuperator on the cathode side and radiators on the liquid side. The power generated by the stack minus the power required for cooling and pumping the fluids is the quantity to be maximized in the overall system design. As far as pumping goes, the air stream will require much more power than the liquid stream, due to the properties of both fluids and the fact that much more air than liquid is pumped into the stack. Therefore, the pressure drop on the cathode side of the cell has been studied in greater detail.

The pressure drop analysis of both the waffle and serpentine flow field designs yielded a direct proportionality between flow rate and pressure drop. As expected, the pressure drop for the waffle pattern was significantly lower than that of the serpentine paths. Pressure drop depended on several geometric factors, including the length, width, and depth of channels, as well as upon the number of channels in each cell. For a 2-serpentine path flow field of length and width 2.680 inches, with a channel width and depth of 47 and 36 mils respectively, the total pressure drop associated with a flow rate of 1 liter per minute was 0.842 psi. The number of turns for each serpentine was 16. On the contrary, the pressure drop for an 8 by 13 grid of channels in a flow field of the same dimensions and under the same flow conditions was only 0.0216 psi. The pressure drop declined as the number of channels in the flow field grid was increased. Similarly, the pressure drop in the serpentine flow field decreased as more serpentine paths were added. These are obvious results of the fact that for a constant overall flow rate, the flow rate per path diminishes with an increasing number of paths. Thus, the pressure drop across each path is lower, as is the overall pressure drop. It also makes intuitive sense that the pressure drop should be lower for the waffle design than for a serpentine design, as the latter contains fewer paths of greater length, with turning losses to boot. In the limits of n serpentine paths with no turns, and a waffle pattern with n channels in one direction only, the two designs are equivalent.

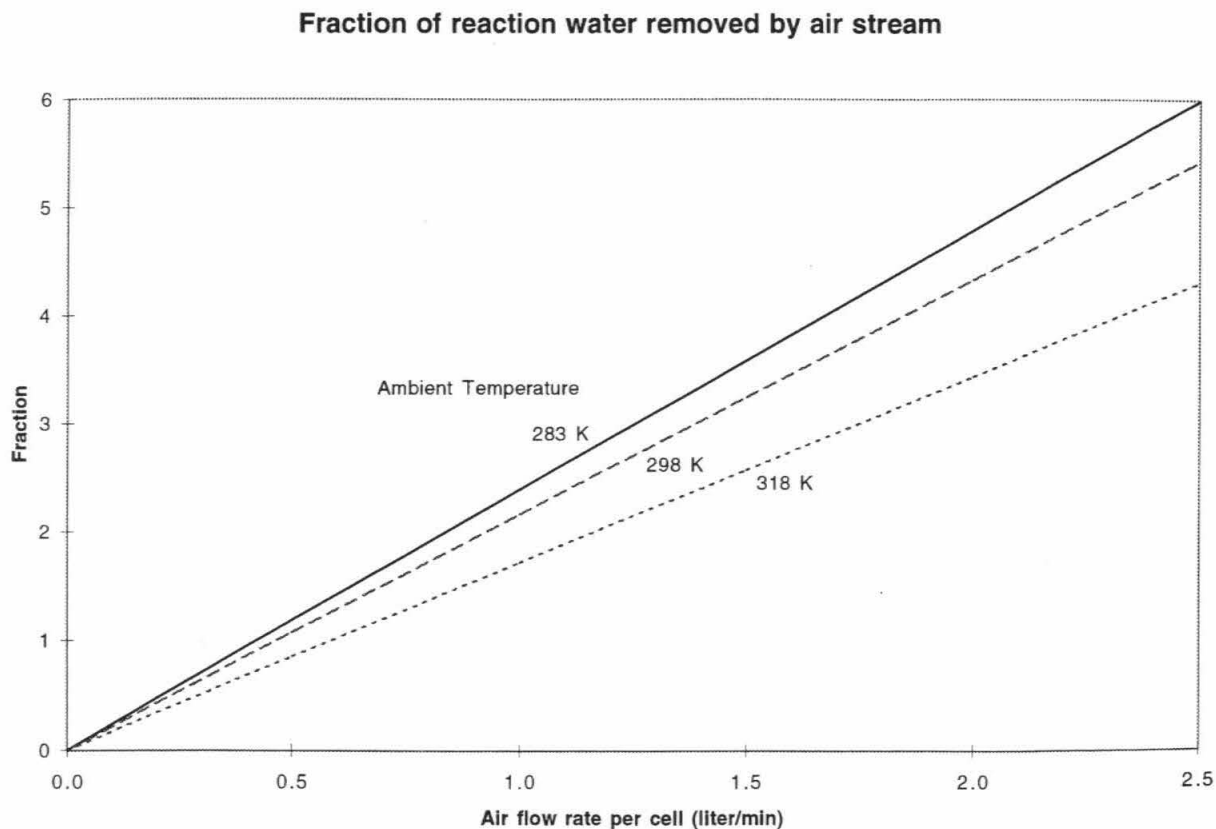


Figure 6. Ratio of water removed by the air stream to water produced via crossover combustion and electrochemical reaction, as a function of air flow rate and ambient temperature. The stack temperature is 333 K, the current density is 100 mA/cm², and the relative humidity is 0.5.

One element that was not accounted for in this flow field model was the effect water accumulation has upon pressure drop. Such accumulation would lead to a higher pressure drop via one or more mechanisms. If water plugs form, completely blocking the channel, a higher pressure will be necessary to push them through the flow field, as the viscosity of water is greater than that of air. If instead the water forms as a film on the walls of the channel, surface tension will make water removal more difficult, and the channel will be constricted. Since pressure drop is inversely proportional to the fourth power of the hydraulic radius, any constriction will raise the pressure drop significantly.

Conclusion

As indicated by the results of heat and water removal calculations for the cathode side of the fuel cell system, the inlet temperature and water content of the air stream will have to be controlled if the system is to be operated over a wide range of ambient and stack conditions. Further calculations and refinement of the current model are necessary in order to determine which conditions will necessitate the use of a recuperator or some other mechanism to humidify the air stream. Various models of the direct methanol liquid feed fuel cell may be designed and manufactured according to the specific application, and a recuperator or other type of humidifier will most likely not be required in all cases. The number of cells and cell area will also depend upon the application, as there is a trade-off between minimizing stack weight and size and maximizing the net power deliverable at a given current density, temperature, and reactant flow rates.

The model used for pressure drop calculations does not yield highly accurate quantitative results, but it does serve as a valid qualitative tool for comparing one flow field design to another. Refining the model to account for water blockage will require further experimental work upon two phase flow in channels and serpentine. If studies that relate the pressure drop to the quantity of water produced at the cathode are carried out, much of the model will become obsolete, as a correlation would replace several of the equations derived from theoretical considerations.

Other limitations in the fuel cell model include the narrow range of temperatures, current densities, and air flow rates over which the voltage and crossover correlations yield reasonable predictions. Furthermore, these values depend upon other parameters as well, such as methanol concentration and flow rate, but have not been evaluated experimentally as the parameters are varied. Fortunately, any further experimental work will lead to improved correlations which can be easily inserted into the present model.

The next step in the modeling process will be to size system components such that steady state can be achieved under the most severe operating conditions. A series of calculations will be made over the range of all relevant parameters in order to optimize system size, efficiency, and net output. Sensitivity analyses will aid in determining which parameters most seriously impact system performance, and thus require the highest degree of control. Once the properties of all ancillaries and control mechanisms are fixed, the model will undergo a final revision with this set of properties as a static basis for further calculations.

Acknowledgments

I would like express my gratitude to the members of the direct methanol fuel cell team at the Jet Propulsion Laboratory for all of their assistance with this project, especially my mentor Dr. Narayanan who has provided invaluable guidance and support. I would also like to thank JPL and the Caltech SURF program for funding the research.

References

1. Valdez, T. I., S. R. Narayanan, H. Frank, and W. Chun. Direct Methanol Fuel Cell for Portable Applications. The Twelfth Annual Battery Conference on Applications and Advances, Long Beach, CA, Jan 14-17 (1997) p. 239.
2. Thirumalai, D. and R. E. White. Mathematical Modeling of Proton-Exchange-Membrane Fuel-Cell Stacks. *J. Electrochem. Soc.*, 144, 1717 (1997).
3. Bloomfield, D. P., V. J. Bloomfield, P. D. Grosjean, and J. W. Kelland. Mobile Electric Power: Final Report, Feb (1995) p. 17.

Analysis of Jovian 5- μ M Hot Spot Reflectivities Using Hubble Space Telescope Data

Andreas C. Tziolas, University of Leicester, and Glenn S. Orton

Hubble Space Telescope (HST) data has been widely used in supporting the Galileo mission and has played a key role in characterising the Probe Entry Site hot spot. HST images, as all others, need to be rigorously calibrated before they are used to drive and support the science returned from Galileo. This process includes bias subtraction, dark reduction, flat-fielding, cosmic ray compensation, geometry correction and finally "absolute" photometric analysis. The data returned by the Galileo probe, are now being challenged with data from many sources, the best resolved of which are HST data.

Photometric analysis of the Probe Entry Site (PES) has not been performed before and there is interest in the results of such a study. Local reflectivities for the PES and a neighbouring hot spot have been examined for dates spanning from April 1995, through to October 1996. Multiple wavelengths were examined making good use of the Wide Field and Planetary Camera mark II (WF/PC2) data available and producing reflectivity spectra for each epoch that are consistent with ground base observations, such as those from NASA's Infra Red Telescope Facility (IRTF).

All verify the unpredictable nature of the events that sustain hot spot regions. Thus, the reflectivity variations have been recorded for each wavelength throughout the time period examined. A neighbouring hot spot that interacts with the PES hot spot has also been monitored in the same respects, in an attempt to lay down a pattern of behaviour for the always restless Jovian hot spots and atmosphere.

History of Observations

The highest resolution data from Jupiter available, since the observations performed by Voyager, involve sets both preceding and following the epoch of the probe entry, come from the WF/PC2. With the Planetary Camera and its 0.0455 arcsec/pixel resolution, the 5- μ m hot spot was investigated using filters relevant to wavelengths spanning from the far ultra violet to the near infra red, as listed in Table 1.

Coincident observations of the PES in visible wavelengths with the HST were inhibited by Jupiter's near solar conjunction, that brought the planet a mere 9° from the Sun. However, supporting the time of the Galileo probe entry are data sets from the 4th and 5th of October 1995. Cycle 5 data from the 5th of March 1995, the 14th of May and the 27th of June 1996, complement the data used in this characterisation. Other sets either portray a rather diverse image the 5- μ m hot spot, from the one known from the 7th of December, or do not include it at all and were not included in this investigation.

Scaling to Reflectivity Units

To scale each pixels intensity (DN) to local reflectivities, the data were calibrated using Photocalibration factors provided by Karkoschka *et al* (1994) and completed with assistance from Kathy Rages *et al* (1995). The albedo values were found by multiplying the filter and instrument transmission curve with the solar spectrum and then convolving this with Jupiter's albedo spectrum. The following simple equation was used to derive the reflectivities from the images:

$$I / F = \frac{DN * factor}{t_{exposure} * 10,000}$$

Where, $t_{exposure}$ is the exposure time in seconds and 10,000 is a normalising factor. There were factors missing however, most importantly for the Red, 673nm filter. In this study, the 673nm data play an important role as visual and infrared data are compared. Hence, a multiplicative factor was calculated that converts pixel brightness (DN) to local reflectivity units (I/F). This factor obeys the relation:

$$factor = \frac{DB_{Karkoschka}}{DB_{Image}}$$

Here, $DB_{Karkoschka}$ is the average disk brightness, found by convolving Karkoschka's full disc albedo spectrum with the corresponding filter response profile and DB_{Image} is the disk brightness calculated for each image. The filter function of the F673N filter, is a narrow band filter that includes emission lines from SII (671.6 and 673.1nm) and was designed to have a dimensionless bandpass profile. Thus it is sharp enough to omit convolving the albedo average with the filter function, without inducing unprecedented errors.

It is often the case with PC images, to have an entire side of the planet cut from the image, due to the huge resolution of the camera. When averaging the disk brightness, one does not include one of the dark limbs of the planet with the result of getting an inaccurate average from the rest of the disk. This introduces an ~5% error that covers the inherent error when doing Photocalibration with factors, a conclusion also supported by Chanover *et al* (1996). There are ways of compensating for this problem and this involves studying the HST's and Jupiter's orbits and finding images that include the limb missing. Attention must be paid to match the incidence μ and reflectance angles μ_0 of radiation from the Sun.

Table 1 includes the Photocalibration factors used to reduce the images. The multiplicative factors used for the F673N filter were 4.402×10^{-4} for the May 1996, PC data and 1.128×10^{-3} for the June 1996 WF data. Note they are dependant on the camera and gain used to take the image.

Limb Darkening Effects

The data was accumulated from a range of dates, making them difficult to compare. Limb darkening, which occurs only in the Sun and Jupiter, due to its size, is a condition in which the brightness of the object decreases as the limb of the planet is approached. In the data sets examined, the 5- μ m hot spot was often close to the limb of the planet, making it susceptible to limb-darkening effects that distort the true reflectivity of the features under examination.

When correcting for limb darkening in the Sun, it is often the procedure to determine the radial average reflectivity, that is along each radius and then divide all the data by this value, effectively normalising to that value. Another way to compensate for limb darkening involves taking the 2-D Fourier transform of all data and removing the low order terms. When the image is reconstructed from the high frequency components, the image is free of the lower-intensities that caused the limb darkening. No model is assumed in this treatment and is a good way of making the image equally bright. However, a more mathematically orientated approach was used, as the effects of the Fourier transform method on the data was unknown. This involves modelling the actual reflectivity variations with the following, the Minneart function:

$$I / F = \frac{I / F_{Measured}}{\mu^k * \mu_0^{2k-1}}$$

Where the measured local reflectivity is normalised via dividing by expressions of the emission and incident sunlight cosine angles μ and μ_0 , respectively.

We can see that the larger the coefficient, the less dependent the limb darkening is and the more it resembles sunlight reflected off an isotropically scattering globe. For short-wave filters where Rayleigh scattering is important this does not hold and k is around 7 (Beebe *et al*). For longer wavelengths where a larger component of the radiation is reflected light from a rough clouded structure, where the scale of the structure is small relative to our resolution element, the Lambert case, $k=1$, is more appropriate at "Red" wavelengths without molecular scattering. At 893nm, where CH_4 absorption is very strong, little reflected light is returning and again k approaches 1, because the light is reflected off of the high clouds and is more dependent on solar illumination than anything else.

Table 1. Karkoschka Photocalibration Factors

Filter	WF Gain	PC Gain
F218W	810.00 H	0.00 X
F255W	144.50 H	677.00 H
F336W	5.20 L	25.30 L
F410M	4.70 L	23.00 L
F547W	0.33 L	0.00 X
F555W	0.00 X	0.72 L
F953N	24.00 L	57.30 H
FQCH	13.00 L	61.40 L
FQCH ₄	13.00 L	31.40 H

Only wavelengths that were to be compared to the NSFCAM data were corrected for limb darkening. In an attempt to customise the Minneart equation to our reflectivity model and our observations, the dependence of μ_0 was assumed independent of k , giving the model more flexibility. Hence, the new form:

$$I / F = \frac{I / F_{Measured}}{\mu^k * \mu_0^1}$$

By fitting this equation to the data, the k, l values that correspond to each wavelength of observation were determined. Specifically, the values that resulted in an intensity flattened image were averaged for each wavelength and comprise Table 2. As μ, μ_0 approach 1, it was proven difficult to discriminate between their individual contributions to the limb darkening affect and thus their average sum value was used, along with the standard deviation of the k, l values about their mean, as shown in Table 2.

Table 2. Minneart Limb Darkening Correction Factors

λ nm	k	l	$k+l$	σ
410	0.59	0.34	0.93	0.10
555	0.44	0.60	1.04	0.06
673	0.34	0.69	1.03	0.06
893	1.06	0.20	1.03	0.06
953	0.58	0.70	1.28	0.18

Correlation of Visual - Infra Red Data

The HST datasets taken with the WF/PC2, were coupled with data from the Near Infrared Camera/Spectrometer (NSFCAM), an facility instrument of NASA's Infrared Telescope Facility (IRTF). The closest incident data and their observation time intervals are described in Table 3. The time difference and separation of features are crucial in this treatment. Time is in Universal Time (UT).

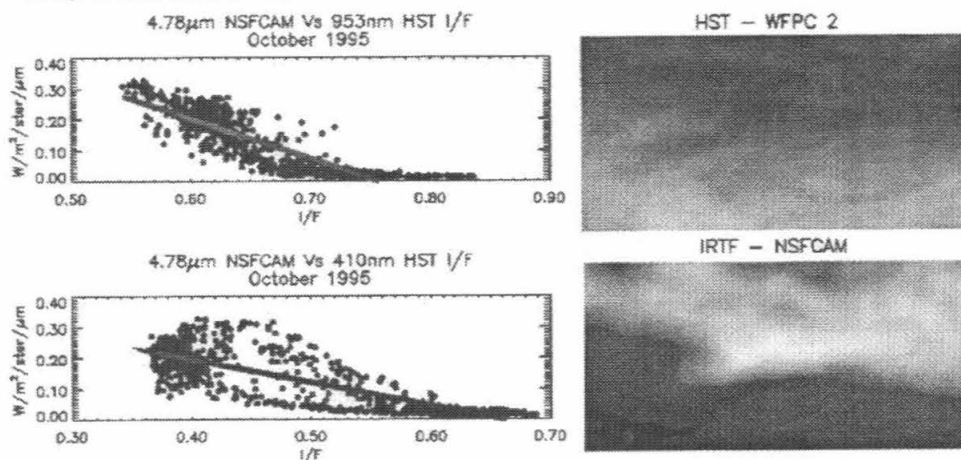
Table 3. HST - IRTF Coincident Observations

HST Date	Time	IRTF Date	Time	$\Delta(\text{time})$	PES $\Delta(\text{degs})$	LCMIII
04/03/95	18:24:16	08/03/95	20:23:13	-97:58:57	-20.17	207°
04/10/95	20:39:16	04/10/95	05:06:30	+15:32:46	+3.19	102°
27/06/97	03:07:16	26/06/96	07:18:18	-19:48:58	-4.07	12°

As an additional step to the calibration, the consideration that there may have been shifts in the global reflectivity of Jupiter in the 7 to 8 month interval between HST observations though, something that would add to the lack of homogeneity in these observations. The disc average reflectivity between observations, with comparable time lapses, were investigated by Chanover *et al.* Limb-to-terminator scans showed reflectivity variations of ~6% and phase angle differences of the planet, between the two dates, affected the I/F by ~4%. Corrections were not made on the data, but this was taken into consideration as an added error.

Figure 1 shows a comparison of the 4.78 μm thermal radiance measured by the NSFCAM at the IRTF with the 953nm and 410nm reflectivity measured by the HST Planetary Camera for the October 1995 epoch. The 10° latitude by 20° longitude region centered on the feature at 6.5° N planetocentric latitude are shown in the adjacent panels. The upper panel is an enhanced colour composite taken from cylindrical projections of HST PC images. The lower panel is the same region taken from an NSFCAM IRTF 4.78 μm image. The HST image has been shifted in longitude to match the motion of the hot spot during the short time separation between the two observations, as summarised in Table 3. The linear regression fit to the data excluded points with thermal radiance less than 0.06 W/m²/ster/ μm . The correlation coefficient for the 953nm vs. 4.78 μm radiance is 0.66 and for the 410nm vs. 4.78 μm radiance is 0.41, in a negative sense. The data from June 1996 were also correlated and correlated to 0.91 and 0.52, respectively.

Figure 1. Visual/IR Correlation Plot



The predominant “Blue” colour the hot spots display in the visual raised many questions, which were partially resolved by the correlations described above. A class of cold points at $4.78\mu\text{m}$, spotted by Orton *et al* (1997) with radiance less than $0.07 \text{ W/m}^2/\text{ster}/\mu\text{m}$, particularly prominent in the 1995 data, represents a wide range of high reflectivity values at both 953nm and 410nm. These points correspond to regions in the lower half of the images, which belong to the Equatorial Region. Regions with higher $4.78\mu\text{m}$ radiances are clearly correlated with lower 953nm reflectivity, i.e $I/F < 0.60$. For a given radiance, the spread of I/F values at 953nm is 0.05 or less for October 1995 and ~ 0.08 for June 1996, when ground based observations were poorer.

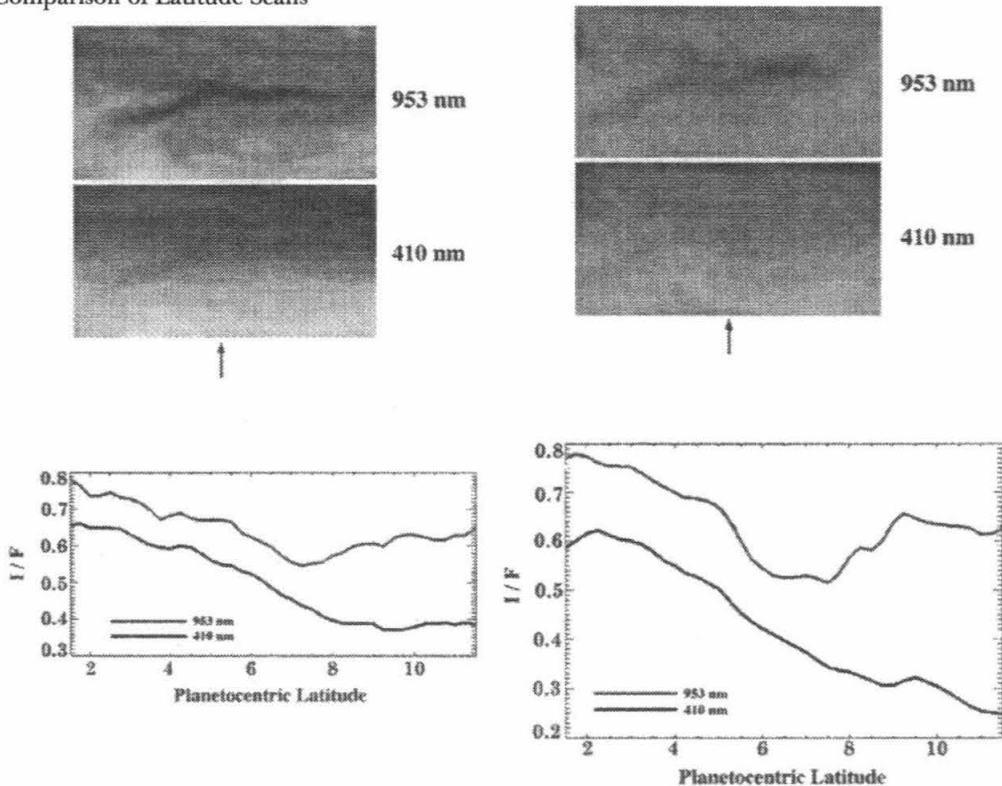
All hot spots seem to be better defined in the “Red” than in the “Blue”, as the absolute correlation coefficients are 0.5 or less and the spread of I/F values are ~ 0.20 at best. In Figure 3 the latitudinal variations of the hot spots at 953nm and 410nm are plotted, possibly revealing the source of this discrepancy. For both epochs of observations, the PES is a distinct feature at 953nm. This is not absolutely true as the feature’s contrast is much lower at 410nm, where the northern boundary extends towards the North Equatorial Belt and becomes indistinguishable.

To solve the mystery of the blue colour $5\text{-}\mu\text{m}$ hot spots assume in the visual, a hypothesis was suggested by West *et al* (1986), who suggested that only differences in large particle populations are of effect, although they could be considered negligible at such short wavelengths, according to Irwin *et al* (1997). A solution has been offered by Orton *et al* (1997), that suggests a combination of the above two opinions, as a mixture of particles of various sizes, all with different single scattering albedos in the visible, can emerge as a chromophore component of the atmosphere, hence providing a justification of the predominant blue colour, the hot spots assume in the visible.

Latitudinal Reflectivity Variations

The Galileo probe entered the southern end of the $5\text{-}\mu\text{m}$ hot spot. The range of WF/PC2 filters used in the coincident observations described in Table 3, allowed the hot spot to be compared at several wavelengths. This approach hints towards the chemical composition of the hot spot. Most interesting was the comparison of the “Blue” and NIR wavelengths, 410 and 953nm. At 410 nm the hot spot is less defined and becomes barely visible, towards the North. In the NIR regime though, the hot spot displays much more structure and is well defined. Figure 2 displays a comparison of their reflectivity variations with latitude, centered at 6.45° North, in Local Central Meridian System III (LCMIII) co-ordinates, which assume a solid spinning nucleus for Jupiter, coherent with the planets magnetic field. The false color images represent what the hot spots look like in the wavelengths compared, where the regions compared are pointed out by the arrow.

Figure 2. Comparison of Latitude Scans

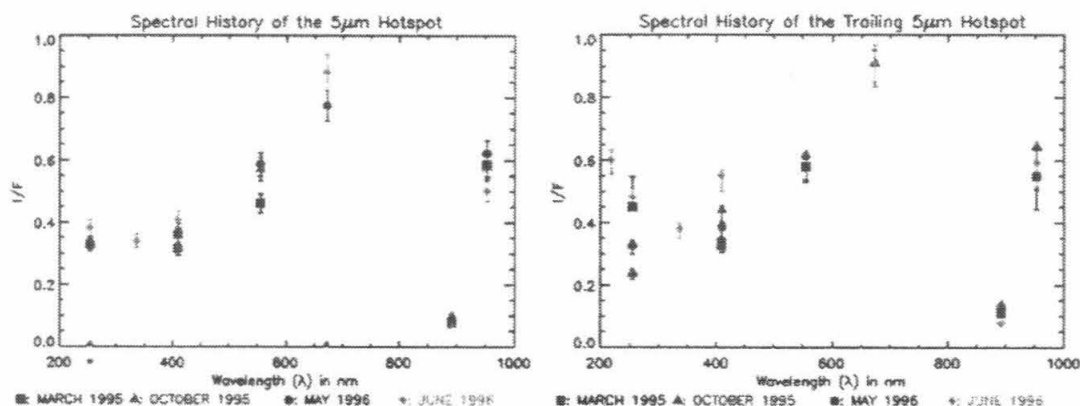


In the October 1995 data, the reflectivity variations in the “Blue” change smoothly with the “Red”. The June 1996 data is considerably more structured, especially in the “Red”, but the variations still follow the same gradients. The relative images of the hot spots at those wavelengths, portray what the plots are describing. Hot spots are significantly more defined in NIR wavelengths. In the 9 months between these observations the PES hot spot’s characteristics started or, should we say, continued to fluctuate, as is the case with hot spots in general. These fluctuations began dispersing the hot spot’s limbs, causing the fluctuations seen in the figure.

Spectral Variations of the PES and 5- μm Hot Spot

In an attempt to characterise the PES and compare it to the morphology of the specific and other 5- μm hot spots, the reflectivity history of the spot in interest was determined for the various epochs of HST observations. As it was determined, the probe entered the southern part of the hot spot, at a latitude of 6.45° N LCMIII. For comparison, a neighbouring 5 μm hot spot that trailed the PES by 40°-45° was selected to be investigated, because the two shared the same latitude, form and brightness temperature. The observed reflectivity has been adjusted to emission and incidence angles of 45° each. The reflectivities are taken from a 1° span of longitude centered on the PES and error bars represent a combination of the variance of the measured I/F values and the propagation of uncertainties of the Minneart coefficients used to adjust to a common geometry. Not shown is a ~5% uncertainty in the absolute calibration affecting all the data.

Figure 3. PES, Trailing and 5 μm Hotspot Spectra



The high reflectance at 555nm (Green), 673nm (Red) and 953nm (NIR), along with the strong absorbance at 892nm, where gaseous CH₄ absorption occurs, is expected of this plot and serves as a cross check to the validity of the data.

The PES reflectivity spectrum and that of the centre of the 5 μm hot spot, defined by the latitude at which the “Red” reflectivity was a minimum, as seen in figure 2, are very similar, as expected, with the maximum I/F deviation reaching 0.1. The spectrum from the companion hot spot, also has negligible variations from the other two. Although the morphology and 5 μm radiance varied over the October 1995 - June 1996 period, the visible spectrum did not. At the time of the probe entry, it is safe to conclude that the hot spot’s condition was nominal and hence the data collected by the probe are representative of the Jovian atmosphere. All evidence is pointing towards the conclusion that hot spot reflectivities do not vary drastically in this frequency range.

Overall, the three spectra have well correlated points and display a certain overall consistency. At short-wave frequencies there is an increased distribution of reflectivities in the trailing hot spot, within reasonable error. The spectral characteristics of these two hot spots are consistent and this result can be extended to the bulk of hot spots that fit the thermally elevated regimes in this belt, further known as 5 μm hot spots.

Conclusions

By observing 5- μm hot spots in the IR and visual we see that "Red" radiance is dominant. The "Blue" wavelengths seem to emphasise high cloud tops which camouflage and help blend the area with the Northern Equatorial Belt, which is characterised by high ammonia clouds. Their peculiar blue colour in the visual is most likely caused by the interaction of various molecules with different sizes and origins. Two cloud layers, an upper tropospheric cloud based between 350 and 460mbar, and a lower tropospheric cloud between 1.5 and 3.0mbar, identified by Stewart *et al* (1997) could be the origins of these two types of molecules, that otherwise reside in their individual pressure heights. The assumption is made that they are independently non-chromoactive, but their combination provides sufficient scattering characteristics as to reflect this predominant blue, that is now well coupled with 5 μm hot spots.

The spectra produced, enabled the comparison of the hot spot PES, minimum and other hot spots, revealing the astonishing coherence of characteristics, even though during the epoch of observations the PES hot spot grew through its "life cycle", from emergence to dissipation. Strong evidence of an permanent underlying mechanism that systematically produces hot spots with specific characteristics is now found. This points towards a large scale phenomenon focused at the equatorial region and spanning $\pm 10^\circ$ North and South, that results in vertical cloud motions and the rise of material from the depths of the atmosphere, the mysterious force driving the emergence and demise of 5 μm hot spots.

References

- Chanover *et al*, 'Absolute reflectivity spectra for Jupiter: 0.25-3.5 μm ', *Icarus* 121, 351-360, 1996.
- Irwin *et al*, 'Cloud structure and atmospheric composition of Jupiter retrieved from Galileo NIMS real-time spectra', *J. Geophys. Res.*, 1997.
- Orton *et al*, 'Preliminary results of Earth based observations of the Galileo probe entry site', *Science* 272, 839-840, 1996. -*Special Thanks*
- Stewart *et al*, 'The cloud structure of the north equatorial zone: Context of the Galileo probe entry latitude', submitted to *J. Geophys. Res.- Planets*, 1997.
- West *et al*, 'Impact debris particles in Jupiter's atmosphere', *Science* 267, 1296-1301, 1995.
- Rages, personal communications.
- Karkoshka *et al*, (1994)
- WF/PC2 manual, Version 4.0, June 1996.
- Galileo Homepage, <http://www.jpl.nasa.gov/galileo/>.
- STScI Homepage, <http://www.stsci.edu/>.

Analysis of Two Aspects of the Ethylene Signal Transduction Pathway in *Arabidopsis thaliana*

Alfred Wang, Jian Hua, and Elliot M. Meyerowitz

Studies of the signal transduction pathway of ethylene in the model plant *Arabidopsis thaliana* has led to the discovery of several ethylene receptor genes, *ETR1*, *ERS*, *ETR2*, *EIN4*, and *ERS2*. During studies on the ethylene receptor gene *ETR2*, a weak extragenic suppressor of the *etr2-1* mutation was isolated and named *solh* (suppressor of long hypocotyl). The *solh* mutant displayed a phenotype in between that of wild type plants and ethylene resistant plants, having shortened hypocotyls, slight apical hooks, and long roots. Genomic mapping of the gene using Simple Sequence Length Polymorphisms (SSLPs) and Cleaved Amplified Polymorphic Sequences (CAPS) has localized the gene on chromosome five of *Arabidopsis*. Mutant analysis suggests that the *SOLH* gene is responsible for hypocotyl elongation in etiolated seedlings. In addition to *SOLH* gene, tests were performed on the interactions of *CTR1*, a negative regulator of the ethylene response, with the ethylene receptors *ETR2*, *EIN4*, and *ERS2*. Previous studies have shown that the receptors *ETR1* and *ERS* directly interact with *CTR1* in several *in vitro* assays. No such interactions were observed in the two-hybrid assay between *CTR1* and the other ethylene receptors *ETR2*, *EIN4*, and *ERS2*. This result suggest the possibility of the existence of functional differences among these receptors.

Introduction

Ethylene, the widely known fruit ripener, regulates several processes in plant development including leaf senescence, flower abscission, and seed germination (1). It has also been implicated in the responses of plants to certain environmental stresses, such as wounds and bacterial infection. The role of this colorless gas in these important aspects of plant growth have made it an attractive target in plant research. A complete understanding of the ethylene signal transduction pathway could have significant applications in the agricultural and farming industries, resulting in the production of healthier and longer lived crops, as well as fruits and vegetables with a prolonged shelf-life. Significant progress has been made in recent years in understanding the molecular pathways involved in ethylene perception. More than a dozen players have been identified in the signal transduction pathway. The small genome and short generation time of the mustard weed, *Arabidopsis thaliana*, make it an ideal model for studying the ethylene signal transduction pathway in plants.

The approach taken to elucidate the molecular mechanisms of ethylene signal transduction has been to isolate mutants defective in ethylene perception, and to identify and study the genes responsible for the defects. In plants, ethylene confers a characteristic 'triple response' in etiolated seedlings which is useful in screening for ethylene response mutants. The triple response consists of a shortening and radial swelling of the hypocotyl, severely stunted root growth, and a severe apical hook. Defects in the ethylene receptors confer a lack of this phenotype, causing the seedlings to lack an apical hook, and to have long, slender hypocotyls and long roots. Several of these ethylene insensitive mutants have been isolated and characterized, and the genes responsible for the defects have been cloned. Among them is the *etr2-1* mutant, which has an ethylene resistant phenotype due to a dominant missense mutation in the *ETR2* ethylene receptor gene (10). In order to better understand the nature of the *ETR2* ethylene receptor, suppressor screens were performed on *etr2-1* mutants that reverted back to the wild type ethylene response phenotype, which would imply a redundant role for *ETR2* in ethylene perception. A mutant with these characteristics was isolated and named as *solh* (suppressor of long hypocotyl). The *solh* mutant expressed an incomplete suppression of the ethylene resistant phenotype, resulting in seedlings with short and radially swelled hypocotyls, slight apical hooks, but long roots characteristic of ethylene resistant plants. Here, we describe the phenotype of this suppressor and the *solh* mutant by itself. The location of the mutation in the *Arabidopsis* genome was also determined using simple sequence length polymorphisms (SSLPs) and cleaved amplified polymorphic sequences (CAPS).

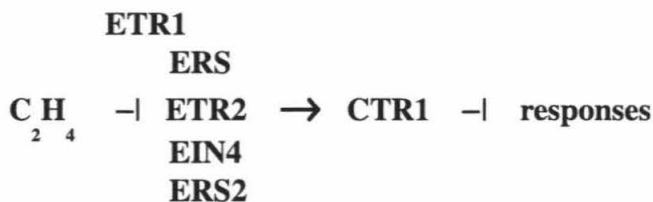


Figure 1. The proposed ethylene signal transduction pathway in *Arabidopsis*.

CTR1, a negative regulator of the ethylene response, lies downstream of the family of ethylene receptors (Fig. 1). It has recently been shown that the ethylene receptors ETR1 and ERS interact directly with CTR1 in the two-hybrid assay and coimmunoassay, suggesting that there are direct physical interactions between these receptors and CTR1 (2). It was then questioned whether the homologous ethylene receptors ETR2, EIN4, and ERS2 could also interact directly with CTR1. This physical interaction was tested with the LexA version of the yeast two-hybrid assay.

Materials and Methods

Plant Growth and Crosses

Seeds resulting from plant crosses were grown on MS (Murashige-Skoog) 1% agar plates. These plates were then wrapped in aluminum foil to prevent light exposure, and cold treated at 4°C for three days to enhance and obtain synchronous germination, and then exposed to four hours of light before being re-wrapped in foil and placed in the ethylene chamber. The plates were exposed to 10 ppm of ethylene for three days at which time they were ready to be scored for their phenotype.

Plant Genotyping

Plants were genotyped using the Polymerase Chain Reaction (PCR) and synthesized oligonucleotide primers designed to only amplify specific alleles. Plant tissues for PCR were prepped using a boiling preparation consisting of boiling a leaf piece for 45 seconds in 40 µl of 0.25 M NaOH, and then another 2 minute boiling after the addition of 40 µl of HCl and 20 µl of 0.5 M Tris 8.0. PCR products were run on 2-4% agarose gels, depending on the size of the PCR product/s.

Mapping of SOLH

Genomic DNA was extracted from the leaves of plants according to Konieczny *et al.* (5). This concentrated DNA was eluted in 50 µl of water, and stored at -20°C. Polymorphisms between ecotypes were then detected using either SSLP primers or CAPS primers and PCR using 1 µl of the DNA sample, 2 µl of deoxyribonucleotides, 2 µl of 10x Mg PCR buffer, 0.5 µl of forward and reverse primer, and 0.3 µl of Taq Polymerase, in 14 µl of H₂O. Cycling temperatures were 94°C for 15 s, 55°C for 15 s, and 72°C for 30 s, for 40 cycles. When possible, hot start PCR was utilized to prevent non-specific amplification. This was done by making a bottom cocktail consisting of the primers, deoxyribonucleotides, and DNA and a top solution consisting of Taq Polymerase and the Mg buffer, which was added after the solution had reached 94°C (denaturing stage). All 20 µl of the PCR product were run on 4% agarose gels along with 3 µl of loading dye. Usage of CAPS primers required an additional restriction digest of the PCR product to detect polymorphisms. Typically, 5 µl of PCR product was used in a 20 µl overnight digest.

Plasmid Construction

PCR was used to amplify the histidine kinase and receiver domains of ETR2, EIN4, and the histidine kinase domain of ERS2 using specific primers with a BamHI linker (GGATTC) to facilitate subsequent restriction digest analyses. The PCR consisted of 0.6 µl of cDNA, 4 µl of 10x PCR Buffer with Mg, 0.6 µl of Pfu Polymerase, 2 µl of forward and reverse primers, and 27 µl of sterile H₂O. The PCR products were then ligated to a Zero Blunt Vector (Invitrogen) using 1 µl of T4 DNA Ligase, 1 µl of 10x Ligation Buffer, 2 µl of the vector, and 4 µl of the PCR product, in 2 µl of H₂O. The ligations were incubated at 16°C for three hours, and then transformed into competent *E. coli* cells. The cells were then plated on LB Kan (Kanamycin) agar plates to select for transformants, by incubating overnight at 37°C. Plasmid minipreps (QIAGEN) were used to extract the plasmid DNA from the transformants. BamHI restriction digests were used to cut the insert from the vector and run on a 1% agarose gel. The insert was then cut out from the gel and purified (Bio-Rad Prep-A-Gene). Simultaneously, the vector containing the DNA Binding Domain (pLexA-NLS) was also linearized with Bam HI and dephosphorylated with shrimp alkaline phosphatase, and gel purified (Bio-Rad). A final ligation consisting of 1.5 ml of the purified insert, 1.5 ml of the vector, 0.5 ml of 10x ligation buffer, 0.5 ml of T4 DNA Ligase, in 1 ml of H₂O, fused the histidine kinase and receiver domains of the ethylene receptors with the dephosphorylated vector containing the LexA DNA Binding Domain (pLexA-NLS). Orientation of the inserts was checked using restriction digests (EcoRI for ETR2 and EIN4, PstI for ERS2). Clones with the correct insert orientation were then sequenced to check for errors.

Two Hybrid Assay

Cotransformation of the plasmids into competent yeast cells was performed according to the Clontech MATCHMAKER lithium acetate protocol. Transformed yeast cells were plated on -His/-Leu/-Trp and -Leu/-Trp SD agar plates and incubated at 30°C. Surviving transformants were then restreaked

onto a new -His/-Leu/-Trp SD plate and allowed to grow for 2 to 3 days. β -galactosidase filter assays were performed on these transformants. A fresh nitrocellulose filter was first submerged in a solution consisting of 16.1 g/l of Na HPO \cdot H O, 5.5 g/l of NaH PO \cdot H O, 0.75 g/l KCl, 0.246 g/l MgSO \cdot 7H O, 2.7 ml/l of β -mercaptoethanol,² and 16.7 ml/l of 20 mg/ml X-Gal in a 100 mm petri dish. 1.8 ml of this solution was used for each 100 mm filter. Another fresh filter was placed over the surface of the SD plate containing the transformants. This filter was then lifted from the plate and placed in a pool of liquid nitrogen for several seconds until the filter was frozen, colony side up. The filter was then allowed to thaw to room temperature. This freeze/thaw process was performed three times. The filter with the colonies was then placed colony side up on the X-Gal saturated filter. These were then incubated at 30°C and checked periodically for the appearance of blue colonies.

Results

I. Characterization and Mapping of SOLH

The *solh* mutation was isolated from the *etr2-1* mutation which confers ethylene resistance. Wild type seedlings grown in ethylene usually have very short and fat hypocotyls, very short and hairy roots, and an exaggerated apical hook. Ethylene resistant mutants, such as *etr2-1*, usually have long hypocotyls and roots, and lack an apical hook. The *solh* mutation is recessive, and appears to partially suppress the *etr2-1* mutation. *solh;etr2-1* double mutants grown in ethylene have short and thickened hypocotyls, slight apical hooks, and long roots. A similar phenotype is seen in *solh;etr2-1* double mutants grown in the absence of ethylene.

Mapping of the *SOLH* gene involved crossing the *solh* mutant in a Columbia (Col) ecotype to a wild-type Landsberg (Ler) ecotype plant. F₂ plants segregated three phenotypes; wild-type (ethylene sensitive), ethylene resistant, and *solh*. F₂ plants were screened in ethylene to select for plants with the *solh* phenotype (short hypocotyl with long root). Genomic DNA was extracted from these plants, which was then used for mapping. Mapping of the *SOLH* gene was performed using a series of SSLPs and CAPS on the mapping population. A total of 38 plants were used. The following SSSLP or CAPS markers were used to map the gene (CAPS are italicized):

Chromosome I: nga248, nga111

Chromosome II: nga168, *GPAL*, *m429*

Chromosome III: nga6

Chromosome IV: nga8

Chromosome V: nga225, nga249, ca72, nga106, nga139, nga76, *DFR*, *LFY3*, *ASA1*

Loose linkage was first observed from the CAPS marker *DFR*, located on chromosome five. A series of SSSLP and CAPS markers was used until the *SOLH* gene was mapped onto chromosome five, approximately 3 centimorgans north of the nga106 SSSLP marker (between nga 106 and nga249). When the nga106 SSSLP was used, only two recombinants were detected in the population of 38 plants.

II. Two-Hybrid Assay to Test the Interactions between *CTR1* and the ethylene receptors *ETR2*, *EIN4*, and *ERS2*

The direct interaction between *CTR1* and the ethylene receptors was tested using the LexA version of the yeast two hybrid assay (3). The two hybrid assay is used to detect the direct physical interaction between two target proteins *in vivo* by utilizing the gene regulatory properties of the LexA operators. The LexA operators consists of two physically distinct components, the activation domain and the DNA-binding domain. Transcription of a gene under the control of this operator system can only occur when the activation domain is in direct physical contact with the DNA-binding domain. This transcriptional regulatory system can be used to determine if two proteins of interest have direct physical interactions. By creating a fusion protein composed of one target protein and the LexA DNA-binding domain, and another fusion construct consisting of another target protein and the LexA activation domain, interaction between the two target proteins can be detected by monitoring the expression of a reporter gene regulated by the LexA operators. If interactions between the two proteins exist, their physical contact will allow the LexA activation domain to contact the LexA DNA-binding domain, initiating transcription of the reporter genes. If no interactions occur between the target proteins, the LexA activation domain is prevented from interacting with the DNA-binding domain, resulting in no expression of the downstream reporter genes (Fig. 2). If interactions do exist between the two target proteins, the strength of their interaction can also be determined by measuring the expression levels of these reporter genes.

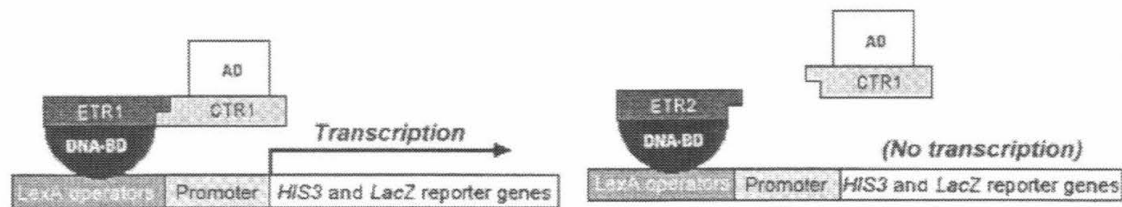


Figure 2. Concept of the LexA Two-Hybrid Assay. In the case on the left, CTR1 and ETR1 have physical interactions, activating the transcription of the *HIS3* and *LacZ* reporter genes. On the right, CTR1 and ETR2 have no interactions, resulting in no transcription or expression of the two reporter genes. DNA-BD represents the DNA-binding domain and AD represents the activation domain.

Our assay relied on the cotransformation of two protein fusions consisting of one of the ethylene receptors fused to the LexA DNA Binding Domain and the CTR1 protein fused to the LexA Activation Domain into a yeast reporter strain (L40). Protein interaction was detected by the expression of two reporter genes: *HIS3*, which confers viability on media lacking of histidine, and *lacZ*, which produces β -galactosidase that reacts with 5-bromo-4-chloro-3-indoyl- β -D-galactopyranoside (X-Gal) to produce a blue color. The intensity of the protein-protein interaction could easily be detected using a β -galactosidase assay to monitor the expression of the *lacZ* reporter gene. The yeast two hybrid assay required the cloning of fusion proteins consisting of the LexA DNA Binding Domain and the histidine kinase and receiver (ETR2 and EIN4 only) domains of the ethylene receptors ETR2, EIN4, and ERS2. These domains were amplified by PCR and then inserted into the pLexA-NLS vector which contains the LexA DNA Binding Domain. A total of three fusions were cloned : ETR2 HKR (Histidine Kinase + Receiver domains) / pLex, EIN4 HKR / pLex, ERS2 HK (Histidine Kinase domain only) / pLex (Fig. 3).

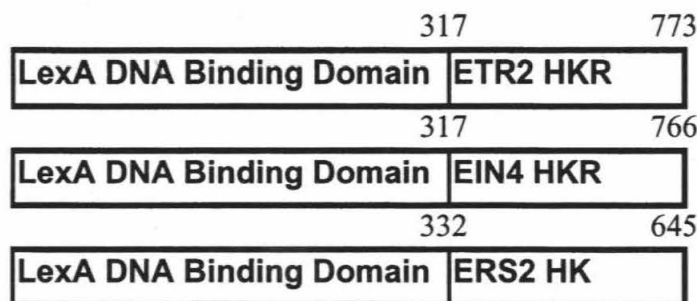


Figure 3. Diagram of the LexA DNA Binding Domain/ETR2 ; EIN4 ; ERS2 histidine kinase + receiver domain fusions. ERS2 lacks a receiver domain, resulting in a shorter fusion product. The numbers denote the starting and ending amino acids.

Through the yeast two hybrid assay, the ethylene receptors ETR2, EIN4, and ERS2 were shown not to directly interact with CTR1. When these fusion proteins were cotransformed into competent yeast along with the CTR1/AD fusion, surviving colonies were present on -Leu/-Trp SD plates, indicating successful cotransformation of the two fusions. But none survived on the -His/-Leu/-Trp SD plates, indicating the lack of interaction between CTR1 and these ethylene receptors. On the other hand, surviving colonies were present on -His/-Leu/-Trp SD plates with yeast cotransformed with ETR1/DNA-BD and CTR1/AD (Table 1).

	Number of yeast colonies on different minimal media				Interaction?
	PGAD (AD)		CTR1 / AD		
	Trp- Leu-	Trp- Leu- His-	Trp- Leu-	Trp- Leu- His-	
pLex (DB)	100	0	0	0	-
ETR1 / DB	5	0	30	15	+
ETR2 / DB	200	0	30	0	-
EIN4 / DB	30	0	40	0	-
ERS2 / DB	100	0	40	0	-

Table 1. Approximate number of surviving colonies from various yeast cotransformations.

β -Galactosidase Filter Assays were performed on the cotransformants to further confirm the results. ETR1/DB ; CTR1/AD cotransformants turned blue after addition of X-Gal in approximately 10 minutes at room temperature. The other cotransformants, including ETR1/DB; PGAD, ETR2/DB; CTR1/AD, EIN4/DB; CTR1/AD, ERS2/DB; CTR1/AD, did not produce a blue color even after 24 hours of exposure to X-Gal and incubation at 30° C. This confirmed the result that the ethylene receptors ETR2, EIN4, and ERS2 do not interact with CTR1. In addition, Western Blotting of the DNA-binding domain fusions with antibodies against the LexA DNA-binding domain were used to confirm the expression of the protein fusions in the cotransformed yeast (9).

Discussion

The *solh ; etr2-1* mutant has an intermediate ethylene triple response phenotype, having the usual short hypocotyl and apical hook, but long roots, which are not characteristic of ethylene sensitive seedlings. The mutant has the same phenotype when grown in both air and ethylene, partially suppressing the *etr2-1* phenotype. Mapping of *SOLH* onto chromosome five has shown no correlation in genomic location to the other members of the ethylene pathway. The location of the *SOLH* gene in the *Arabidopsis* genome suggests it is an unidentified new gene. Since the *solh* mutation has a visible phenotype when seedlings are grown in both air and ethylene, *SOLH* is responsible for hypocotyl elongation in etiolated seedlings. The *SOLH* gene may act to regulate the ethylene response in the hypocotyl. Dosage studies may prove to be useful in elucidating its role. Further double mutant analyses with other ethylene mutants and detailed physiological analysis can lead to a better understanding of its function.

The results from the yeast two hybrid assay strongly suggest that no direct interactions exist between CTR1 and the upstream ethylene receptors ETR2, EIN4, and ERS2. Recent studies done on these receptors suggest they lie parallel to one another in the ethylene signal transduction pathway (8). Since ETR1 and ERS has been shown to directly interact with CTR1 (2), it was suspected that the homologous ethylene receptors ETR2, EIN4, and ERS2 might interact in a similar manner. The lack of interaction between these receptors and CTR1 can be justified by several hypotheses. A possible explanation is that the ethylene receptors ETR1 and ERS, though homologous to the three other receptors, belong to a separate subfamily than the other three, having several critical differences in their amino acid sequences (7). This could result in a significantly lower interaction strength between CTR1 and the three receptors, one that can not be detected by this assay. Another similar hypothesis is that these three receptors function as a multi-subunit complex with some members directly interacting with CTR1. The final possibility is that no interactions actually occur between CTR1 and the ethylene receptors ETR2, EIN4, ERS2. It is possible that important functional differences are present between these two subfamilies, resulting in the interaction of only one subfamily (ETR1 and ERS) with CTR1.

Acknowledgments

I thank Dr. Caren Chang for providing the strains for the two hybrid assay. I also thank Dr. Elliot Meyerowitz for his continuing support, Jian Hua for her patient guidance and mentoring, and Jim Wong for critical comments on the manuscript. This research was funded by the Summer Undergraduate Research Fellowship of the California Institute of Technology and the Howard Hughes Medical Institute.

Bibliography

1. Abeles, F.B., Morgan, P.W., Saltveit, M.E., Jr. (1992) *Ethylene in Plant Biology* (Academic, New York), 2nd Ed.
2. Clark, K.L., Wang, X., Chang, C. (1997) Association of *Arabidopsis* RAF-like CTR1 with ethylene receptors ETR1 and ERS, *in print*.
3. Fields, S., Song, O. (1989) *Nature* **340**, 245
4. Bell, C.J., Ecker, J.R. (1994) Assignment of 30 Microsatellite Loci to the Linkage Map of *Arabidopsis*, *Genomics* **19**, 137-144
5. Konieczny, A., Ausubel, F.M. (1993) A procedure for mapping *Arabidopsis* mutations using co-dominant ecotype specific PCR-based markers, *The Plant Journal* **4**(2), 403-410
6. Chen, D.-C., Yang, B.-C., Kuo, T.-T. (1992), *Current Genetics* **21**, 83
7. Hua, J., Sakai, H., Meyerowitz, E.M. (1997) *Biology and Biotechnology of the Plant Hormone Ethylene*, 71-76
8. Hua, Jian. unpublished data.
9. Kumar, Prakash. unpublished data.
10. Sakai, H., Hua, J., Chen, Q.C., Chang, C., Medrano, L., Bleecker, A.B., Meyerowitz, E.M. ETR2 is an ETR1-like gene involved in ethylene signaling in *Arabidopsis*, *Proc. Nat'l Acad. Sci.* **95**, 5812-5817

California Institute of Technology
Student-Faculty Programs Office
Mail Code 139-74
Pasadena, California 91125

626/395-2885

Fax 626/449-9649

E-Mail sfp@cco.caltech.edu

